# Multimodal characterization of atherosclerotic cardiovascular disease with label-free non-linear optical imaging techniques

by

Leila Büttner Mostaço-Guidolin

A Thesis submitted to the Faculty of Graduate Studies of

The University of Manitoba

in partial fulfilment of the requirements of the degree of

DOCTOR OF PHILOSOPHY

Department of Biomedical Engineering
University of Manitoba

Copyright © 2015 by L.B. Mostaço-Guidolin

*"Continuous effort — not strength or intelligence — is the key to unlocking our potential."*

(L.Cardes)

To the memory of my father, Fernando. To my mother Eliane, my brother Guilherme and to partner to life, Luiz.

# Abstract

Application of the nonlinear optical microscopy (**NLOM**) for investigation of biological samples has, to date, primarily focused the qualitative analysis of images. The general consensus is that nonlinear optical (**NLO**) techniques provide enough biochemical information when compared to, for example, visible light microscopy. Herein, is presented a detailed study where a set of tools for quantitative extraction of information from **NLO** images were developed and tested for the analysis of complex tissue assemblies. Two-photon excited autofluorescence (**TPEF**), second-harmonic generation (**SHG**), and coherent anti-Stokes Raman scattering (**CARS**) were used for the characterization of atherosclerotic plaques.

Our **NLO**-based image analysis of animal arteries affected by atherosclerotic plaque accumulation revealed that images of the healthy regions of the artery can be readily distinguished by marked differences in morphology, due to a fluorescent signal generated from the presence of generally intact elastic layer. Regions affected by lesions were dominated by lipid-rich cells and collagen fibers; the elastic layer was disrupted and the presence of fluorescent particles were also detected. Next, the potential of using information extracted from **NLO** images led us to the development of a new optical index for plaque burden (**OIPB**). Through the **OIPB**, it was possible to investigate and to classify the plaque severity regarding the already established and currently used definition during clinical analyses.

Extrapolating to and anticipating future applications, several methods for extracting specific information from images acquired by each **NLOM** modality were developed and tested. Texture analysis, particle-specific features, fractal analysis and directionality of components within the images were successfully adapted and tailored to better extract relevant information from the **NLO** images. Even though the methods presented in this thesis were mostly tested in images from arterial plaques, there is strong evidence that all tools presented here are capable of tracking changes that occur in many medical conditions and applications.

# Acknowledgments

There are many people who made my time as a graduate student an unique time of my life. I would like to thank some of them here.

First, I must thank my family as without whose support I would never be able to get where I am. In special, I am thankful to my mother Eliane, who is an incredible warrior, always being there ready to help us no matter what, no matter when. 'Obrigada, Manhêêê!'. To my great love, Luiz, incredible person that completes me and inspires me, and whose company paramount in every achievement.

I would like also thank my younger-not-so-little brother Guilherme, for being there, keeping company to mom when I decided flying North. To my special 'Dinda' Mariangela and 'Dindo' Luiz Carlos who are always cheering me on, no matter what is my "new adventure". Grandpa Erich and Grandma Lélia, I am sure you would also be enjoying this moment. Many thanks also to my "expanded" family: Dirce, Pedro, Branca, Giulia, Giovanna and Marcos.

Each of the following individuals has provided me with support, advice, and encouragement throughout the process of developing this thesis. It is with sincere gratitude and appreciation that I thank you all for everything you have done to assist me in one of the most ambitious endeavor of my life so far.

I would like to begin by expressing my thanks to my supervisors, Dr. Arkady Major and Dr. Alex C.-T.Ko, for their continued support, friendship, guidance and encouragement throughout these years of my thesis research.

I also wish to thank Dr. Michael G. Sowa for his invaluable assistance during this journey, which started when he accepted me as a visiting student back when I was still finishing my masters. Thank you to all guidance you have provided me during these years.

I wish to thank my colleagues and friends at the National Research Council of Canada, especially those members of the Spectroscopy group, for their friendship and scientific discussions. Of these, I especially recognize Elicia Kohlemberg and Mark Hewko for their

assitance with all biological samples used in this study. Hours in the histology lab and spreadsheets with rabbit's IDs became much simpler to deal with your help. I also thank Michael S.D. Smith and Bernie Schattka for their assistance, helping me to solve all those *"unexpected hardware-software-issues"*, so common in any experimental research. Many thanks to you all!

I also thank the faculty, students and staff of the Department of Electrical and Computer Engineering, University of Manitoba for their support. I would like to specially thank Amy Dario, for being always there so helpful and so competent when I most needed.

I thank the members of my Ph.D. committee for their encouragement and advice.

Lastly, but not least, I express my sincere thanks to my friends for their support and encouragement over the years. Special thanks goes to Dr. Sandra Kirby, who kindly agreed to help me with all the final revisions.Very special thanks to Dr. Anthony (Tony!) Shaw for his steadfast support over these years.

I thank those individuals who have helped me to keep the balance, while pursing big dreams. Friends who are physically distant but were always there for me (by email, messages, skype calls...). Friends who are close by, chasing good chicken wings deals for Wednesday-nights gatherings. Friends who kept me company while skiing, and training, and training, training. Thank you for helping me to keep motivated, when the body is screaming for some rest. You know who you are. Thank you!

*This thesis is specially dedicated to the memory of my beloved father, Fernando Mostaço. It is your shining example that I try to emulate in all that I do. I miss him every day, and I wish he could have seen to where the* **Mostaço-Methodology"** *has lead me to so far. Thank you for everything.*

*Leila B. Mostaço-Guidolin*

"The only thing that stands between you and your dream is the will to try and the belief that it is actually possible." – Joel Brown

# Contents

# List of Tables

# List of Figures

# List of Copyrighted Material for which permission was obtained

Figure 3.5 - . Reproduced with permission and restrictions from IOP Publishing Ltd. P.31

Chapter 4, 5, 7, and 8 of this thesis are based on the following papers, which I am author and co-author (copyright permission was obtained to include these articles):

- Mostaço-Guidolin LB, Sowa MG, Kohlenberg EK, Smith M, Hewko M, Major A, Ko ACT: **Quantitative nonlinear optical assessment of atherosclerosis progression in rabbits**. *Analytical Chemistry* 2014
- Ko AC, Ridsdale A, Pegoraro AF, Smith MS, Mostaço-Guidolin LB, Hewko MD, Kohlenberg EM, Schattka BJ, Shiomi M, Stolow A, et al.: **Label-free imaging of arterial tissues using photonic crystal fiber (PCF) based nonlinear optical microscopic system**. In *SPIE BiOS: Biomedical Optics*, International Society for Optics and Photonics 2009:718204–718204
- Mostaço-Guidolin LB, Sowa MG, Ridsdale A, Pegoraro AF, Smith MS, Hewko MD, Kohlenberg EK, Schattka B, Shiomi M, Stolow A, et al.: **Differentiating atherosclerotic plaque burden in arterial tissues using femtosecond CARS-based multimodal nonlinear optical imaging**. *Biomedical optics express* 2010, **1**:59–73
- Ko AC, Mostaço-Guidolin LB, Ridsdale A, Pegoraro AF, Smith MS, Slepkov A, Hewko MD, Kohlenberg EK, Schattka B, Stolow A, et al.: **Using multimodal femtosecond CARS imaging to determine plaque burden in luminal atherosclerosis**. In *SPIE BiOS*, International Society for Optics and Photonics 2011:790318–790318
- Ko ACT, Ridsdale A, Mostaço-Guidolin LB, Major A, Stolow A, Sowa MG: **Nonlinear optical microscopy in decoding arterial diseases**. *Biophysical Reviews* 2012, **4**(4):323–334
- Mostaço-Guidolin LB, Ko ACT, Wang F, Xiang B, Hewko M, Tian G, Major

A, Shiomi M, Sowa MG: **Collagen morphology and texture analysis: from statistics to classification**. *Scientific reports* 2013, **3**

- Mostaço-Guidolin LB, Ko ACT, Wang F, Tian H, Hewko M, Shiomi M, Major A, Sowa MG: **Evaluating collagen morphology and pathological lipid deposition using multiphoton image statistics**. In *SPIE BiOS*, International Society for Optics and Photonics 2014:89482A–89482A

Appendix B - Sato Y, Nakajima S, Shiraga N, Atsumi H, Yoshida S, Koller T, Gerig G, Kikinis R: **Three-dimensional multi-scale line filter for segmentation and visualization of curvilinear structures in medical images**. *Medical image analysis* 1998, **2**(2):143–168. Parts reproduced with permission from Elvier. P.136-140

# Chapter 1

# Introduction

The challenge of developing new tools for research and clinical applications in biology and medicine is always generating interest among scientists all around the world. Multidisciplinary research combining optical physics, engineering and medicine enables researchers to use light-matter interactions to explore biological structures and to relate their observations to various physiological functions. With the help of recent advances in optical technologies and their translation into clinical devices, our understanding of biology and medicine has also advanced.

Over the last 15 years, nonlinear optical microscopy (**NLOM**) has emerged as a powerful research tool [27–30]. Based on the physics of nonlinear light-matter interactions, and using these interactions as contrast mechanisms for cellular and tissue imaging investigations, **NLOM** has acquired a reputation of an excellent optical tool for answering multiple biological questions [30–33].

Traditional microscopy techniques, such as confocal microscopy, fluorescence microscopy [34], generate image contrast from light-matter interactions in which the elementary process of absorption involves a single photon, and are dependent linearly on the intensity of the incident light. Nonlinear techniques are fundamentally different in that they use "higher-order" light-matter interactions, involving the absorption or scattering of multiple photons for contrast generation. The nonlinear nature of these interactions leads to new findings and possibilities.

There are two main advantages of using nonlinear optical microscopy. First, **NLOM** can generate images with sub-micron lateral and axial resolution. Such intrinsic confocality makes it possible to generate 3D (three-dimensional) data set. Secondly, many of the nonlinear optical processes rely on endogenous intracellular and extracellular contrasts without labeling. Therefore, these **NLOM** techniques are capable of providing detailed structural images with chemical information from intact unstained samples. Also, the better collection efficiency of **NLOM** compared to traditional techniques, makes it a more suitable tool to characterize highly scattering biological tissue. These images can then be used for correlation with the bio-morphological composition of the samples under investigation entirely based on intrinsic optical selectivity inherent to each of the nonlinear technique.

This thesis is focused on one (among possible others) particular biomedical application of nonlinear optical microscopy. This work tests potential of using nonlinear optical techniques for medical diagnosis tool and to help better understand the biology behind cardiovascular diseases, and atherosclerosis in particular.

Several groups have been studying arterial diseases [1,35–39] using **NLOM**, and have presented interesting results. For example, Lilledahl *et al.* [40] had studied collagen fibrils accumulation in the fibrous cap of atherosclerotic plaque, through two-photon emission fluorescence (**TPEF**) and second-harmonic generation (**SHG**) images. Megens *et al.* [41] applied **TPEF** microscopy to image arteries labeled with specific, fluorescent markers for collagen, inflammatory cells, cell nuclei, and lipids to gain insight into the distribution of collagen and its association with inflammatory cells during plaque formation. Doras *et al.* [42] have performed nonlinear optical image reconstructions, as well as polarization state analysis inside an artery wall affected by atherosclerosis, to investigate the changes in collagen structure. However, until the beginning of this work, none of these studies had tried to develop reliable methodologies to quantify the obtained information, by performing systematic and objective analysis. Thus, it was difficult to evaluate the actual potential of **NLOM** as a diagnostic tool.

To extend **NLOM** beyond a qualitative tool for visualization, we have pioneered a

thorough study of quantitative **NLOM** imaging to investigate biochemical changes which occur in samples taken from a rabbit model for atherosclerosis. One of the main outcomes of this study is a thorough characterization of how atherosclerosis is progressing by closely following relevant biochemical changes in accumulated plaques. This characterization was based on testing, application and validation of a novel *in-house* developed index for quantification of plaque burden [18].

Several other methodologies for image analysis were also performed. For example, texture analysis was applied to analyze and to quantify biochemical compounds accumulated in the plaque [16]. This imaging analysis was implemented to extract structural and biochemical information from images acquired by each nonlinear optical (**NLO**) technique (i.e. **TPEF**, **SHG**, and **CARS**). Complementary results from other established techniques and experiments (e.g. histology and immunohistochemistry), were also presented to validate our hypothesis.

In addition to developing a method specifically relevant for atherosclerosis, this work has also culminated in the development of a unique package for nonlinear optical image analysis. Developed methods and tests specific tailored for each nonlinear technique were tied together and represent a step forward in the characterization of biological components, such as collagen, lipid-rich structures and elastic fibers using quantitative **NLOM** imaging. The methods presented in this thesis can be broadly used in many other applications where objective analysis is needed.

## 1.1 Motivation

There is a need for new tools to better investigate the underlying mechanisms of atherosclerosis and to characterize the various stages of plaque burden progression. Nonlinear optical microscopy, a primarily label-free method, is a useful tool for studying key facets of atherosclerosis. Its label-free characteristic, combined with high sensitivity and specificity for major extracellular molecules, makes it an attractive alternative to conventional histology or fluorescence microscopy in studying arterial structures and vessel

wall composition. The optical sectioning capability of **NLO** methods also provides a means of imaging bulk tissue in 3D.

Three **NLO** methods are employed in this study. Two-photon excited autofluorescence (**TPEF**) has the capability to specifically image extracellular elastin fibers, while second-harmonic generation (**SHG**) can probe type-1 collagen fibrils efficiently. Coherent anti-Stokes Raman scattering (**CARS**), when tuned to image the C-H stretching vibrations, can quickly visualize lipid-rich structures, intracellular and extracellular lipid droplets in unstained intact tissue.

It is well known that both elastin and collagen are the major structural proteins implicated in the remodelling of the arterial wall during plaque development, while lipid accumulation is a hallmark feature of atherosclerosis [43, 44]. Therefore, **NLO** methods are particularly suited to understanding the role and interplay between these key extracellular molecules involved in plaque development. Several studies have demonstrated the use of the **NLOM** to image arterial tissue [1, 35–39]. However, none of these studies have provided quantitative descriptors of the images and related these metrics to the development of atherosclerosis or vascular wall anatomy and pathology.

In the first part of this thesis, the utility of using nonlinear optical images to study structural and biochemical changes that occur in several stages of vascular atherosclerosis were explored. A new quantitative metric (the Optical Index for Plaque Burden - **OIPB**) was developed, tested, and validated to acutely track and classify plaque burden development.

The second part consists of the applications of several methodologies to extract detailed information about each specific component imaged through the **NLOM**. Texture analysis, object identification, particle-specific features are only some examples of possible imaging analyses that were performed. Each image set, acquired by each **NLO** technique, was individually evaluated, aiming to identify specific patterns which can be used to better understand pathological changes during plaque development as well as other diseases.

Additionally, the validation of all results presented in this thesis was carried out

through histological analysis of sections obtained from each analyzed sample. Complementarily, some experiments based on immunohistochemistry (**IHC**) were also performed to provide us with more information in order to understand the observed biological changes.

These experiments, coupled with data analysis based on a solid statistical approach, enabled the development of a valid methodology to extract large amount of information from **NLO** images. It is expected that all our work will contribute not only within the scope of atherosclerosis disease, but also in a more general manner.

## 1.2 Thesis contributions

In this work, **NLOM** was demonstrated as a highly capable technique for imaging of atherosclerotic plaque, at submicron resolution and with highly specific chemical identification. Specifically, the nonlinear processes of **TPEF**, **SHG**, and **CARS** were utilized in a single, multimodal imaging platform to characterize structural and compositional features of the atherosclerotic plaque lesion.

This thesis presents a novel biomedical application of nonlinear optical microscopy, as well as the development of a novel set of tools to interpret the acquired images. In summary, the main contributions achieved during this study were:

- establishment of **NLOM** is a powerful technique that can be used to visualize the extracellular components, such as collagen, elastin, and lipids in atherosclerotic plaques;
- determination of the spatial distribution of these components, and extensive comparison with histopathology, establishing that **NLOM** may be effectively used for optical sectioning to examine bulk tissue without the need for sectioning and staining of the tissue;
- development, testing, and validation of a new quantitative metric (the Optical Index for Plaque Burden - **OIPB**) to accurately track plaque burden development;
- confirmation of critical locations along the aorta for atherosclerotic plaque accu-

mulation, based on results obtained using the **OIPB**;

- classification of plaque levels purely based **NLO** images;
- extraction of textural parameters from **NLO** images provided quantitative descriptors that were linked to specific structural and compositional motifs that characterize different stages of atherosclerotic plaques;
- identification of changes regarding the morphology, orientation, distribution and amount of collagen, elastin and lipid-rich structures were successfully tracked by quantitative methods;

As the main outcome of this study, this research helped to extend **NLOM** beyond its use as a primarily qualitative tool for simple visualization of biological tissue and cells. The work presented here was one of the pioneering in the development of quantitative tools to extract information from **NLO**images.

## 1.3 Thesis outline

This thesis consists of ten chapters. After a brief introduction (Chapter 2), a more general introduction is provided in Chapter 3. The description of the biology behind atherosclerosis is given. Some key points are discussed, including relevant aspects about the biochemical changes observed in vessel wall when plaque formation is initiated. Standards currently used for classification of plaque type and severity, as well as hypothesis about the probable causes of plaque accumulation at preferential vessel sites are also discussed. Finally, the main advantages of specific animal model (**WHHLMI** rabbits) chosen to perform this study is also presented. Also, the theoretical background of nonlinear microscopy techniques used in this study is presented and discussed.

In Chapter 3, technical details related to instrumentation, the microscope and its features are highlighted. A brief discussion about how we can apply **NLOM** to visualize changes that occur in atherosclerotic plaques is given. In Appendix A, tables summarizing possible sources that generate nonlinear contrasts are presented. Finally, this chapter also discusses the experimental procedure adopted in each step of this work, as well as

aspects related to the image analysis and classification.

This thesis is divided into two major parts. The first part focuses on the characterization of atherosclerotic plaque using **NLOM** and its progression. The second part describes the development of quantitative methods to extract information from **NLO** images, creating a set of tools specific to the study of cardiovascular diseases.

In Chapter 4, the development and application of in-house developed Optical Index for Plaque Burden (**OIPB**) is presented. This index was applied to differentiate healthy from abnormal arterial regions along the vessel. **OIPB** was also tested to track disease progression relative to the animal´s age. The study of which locations along the vessel are more prone to plaque development was also performed. Two peer-reviewed journal papers and two conference proceedings were published from these results (Appx. D).

Chapter 5 contains results related to the application of texture analysis for the study of arterial samples. Information regarding how these parameters can track specific features related to the plaque development is presented. One peer-reviewed journal paper and two conference proceedings were generated from these results (Appx. D).

Finally, the last sections of this part presents the results obtained from combining **OIPB** and texture analysis approach. Aiming to improve the scoring and classification of atherosclerotic lesions, according to the American Heart Association (**AHA**) definitions. The results presented in this chapter show the real potential that **NLO** microscopy has for clinical applications.

The second part of this thesis contains more specific methods to analyze and to classify **SHG**, **TPEF**, and **CARS** images. These methods were developed and tested with images acquired for the previous sections of this thesis research, i.e. from arterial samples. Although the results presented are related to cardiovascular diseases, the methods presented in the next three chapters show high potential to be effective in a wide range of applications.

Chapter 7 focuses on the discussion of results obtained by the texture analysis of the **SHG** images to extract complementary information about collagen. In Chapter 8, texture and some particle-specific features were tested in order to classify lipid-rich

structures imaged by **CARS**. Chapter 9 is focused on methods to better characterize the elastic layer of arterial vessels, based on **TPEF** images. Another two peer-reviewed journal papers (referent to each chapter), and two conference proceedings were generated from these results (Appx. D). One additional manuscript is still under preparation. More details can be found in Appendix D. Chapter 10 concluded this work and provided potential future directions.

# Chapter 2

# Background & techniques review

## 2.1 Atherosclerosis and blood vessels

Atherosclerosis involves a set of factors interconnected in a very complex way. To better understand some major aspects of atherosclerosis, a brief explanation of blood vessel structure and its composition is necessary. The arterial wall is basically composed of three layers (or tunica), as shown in Fig. 2.1. The tunica intima or inner layer is relatively thin and mainly consists of a single layer of endothelial cells that lines the vessel lumen.

It is now recognized that the endothelial cells have an important regulatory function for several biological processes [43, 44], rather than being a passive barrier between blood and the tissue. The function of endothelial cells differs considerably throughout the vasculature, not only between different organs but also between large and small blood vessels and between vessels at the arterial and venous side of the circulation [45].

The most abluminal (i.e. outer) part of the tunica intima is the internal elastic lamina (**IEL**) which separates it from the tunica media. The IEL is composed of a layer of elastin. The network-like structure of this layer contributes to cell-cell contact and also allows diffusion of substances [46].

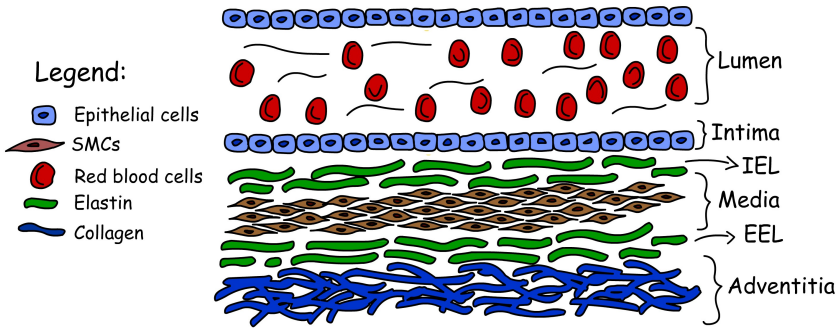


**Figure 2.1:** Schematic representation of a healthy artery. The arteries have three main layers. The tunica intima is a single layer of simple squamous endothelial cells glued by a polysaccharide intercellular matrix, surrounded by a thin layer of sub-endothelial connective tissue interlaced with a number of circularly arranged elastic bands called the internal elastic lamina (**IEL**). The tunica media (the thickest layer) is composed of circularly arranged elastic fiber, connective tissue, and polysaccharide substances; the second and third layer are separated by another thick elastic band called external elastic lamina (**EEL**). The tunica media may (especially in arteries) may be rich in vascular smooth muscle, which controls the caliber of the vessel. Tunica adventitia is entirely composed of collagen and connective tissue. (**SMC**s - smooth muscle cells). Note: The elements of this figure are not to scale. *(© L.Mostaço-Guidolin, 2014)*

The tunica media or medial layer primarily consists of several concentric layers of helically arranged vascular **SMC**. The number of layers depends on size and type of the artery. Vascular **SMC** are separated by fibers of extracellular matrix (**ECM** - collagen, elastin). Interposed between these layers of vascular smooth muscle cells, we have the intermediate elastic lamina (the number of intermediate lamina, again, depends on the size and type of the artery). The main function of the tunica media is to control the vascular tonus. Moreover, the vascular smooth muscle cells are the cellular source of the extracellular matrix [47]. The external elastic lamina (**EEL**), mainly elastin fibers, is the most outer elastic lamina of the tunica media, separating it from the tunica adventitia.

The tunica adventitia is the external layer of the arterial vessel wall and mainly consists of collagen and elastin fibers, which give the vessel structural integrity [47]. In between these fibers, fibroblast-like cells and vasomotor nerves are present. In the tunica adventitia of large arteries, with a vessel wall that is too thick to be solely nourished by diffusion, a network of branched small blood vessels - or *vasa vasorum* - is present, providing metabolites and oxygen to the tunica adventitia and abluminal parts of the tunica media [47]. The vessel walls of various large arteries have a number of structural

features in common, although structural variations between comparable arteries can be considerable. Note that thickness, detailed structure, and function of all tunica types strongly depend on total diameter and type of blood vessel.

### 2.1.1 Atherosclerosis: a general overview

Historically, atherosclerosis was regarded as a disease of vascular lipid accumulation and the endothelial alterations were mainly left out of the picture. The response-to-injury hypothesis, introduced by Virchow in 1856 [48] and later modified by Ross *et al.* [49], postulates that noxious agents, such as shear stress, lipids and oxidation products, damage the endothelium, resulting in increased permeability and enhanced expression of cell adhesion molecules. The ensuing infiltration of inflammatory cells starts a complex process of persistent inflammation and vascular remodeling, which stretches over decades and leads to the development and progression of atheromatous plaques, aneurysms and arterial thrombosis. A sketch showing the progression of atherosclerotic plaques is presented in Fig. 2.2.

Infiltrating leukocytes scavenge lipids and subsequently transform to foam cells, making up the bulk of early lesions [50]. The ensuing inflammation attracts more leukocytes and stimulates vascular smooth muscle cells to proliferate and migrate towards the intima [51]. The latter is the predominant source of extracellular matrix (**ECM**) proteins, such as collagen and elastin, which contributes to progressive plaque growth and arterial remodeling [52, 53]. During lesion progression, the ongoing inflammation and oxygen deprivation in the core of the plaque results in apoptotic and necrotic cell death [54].

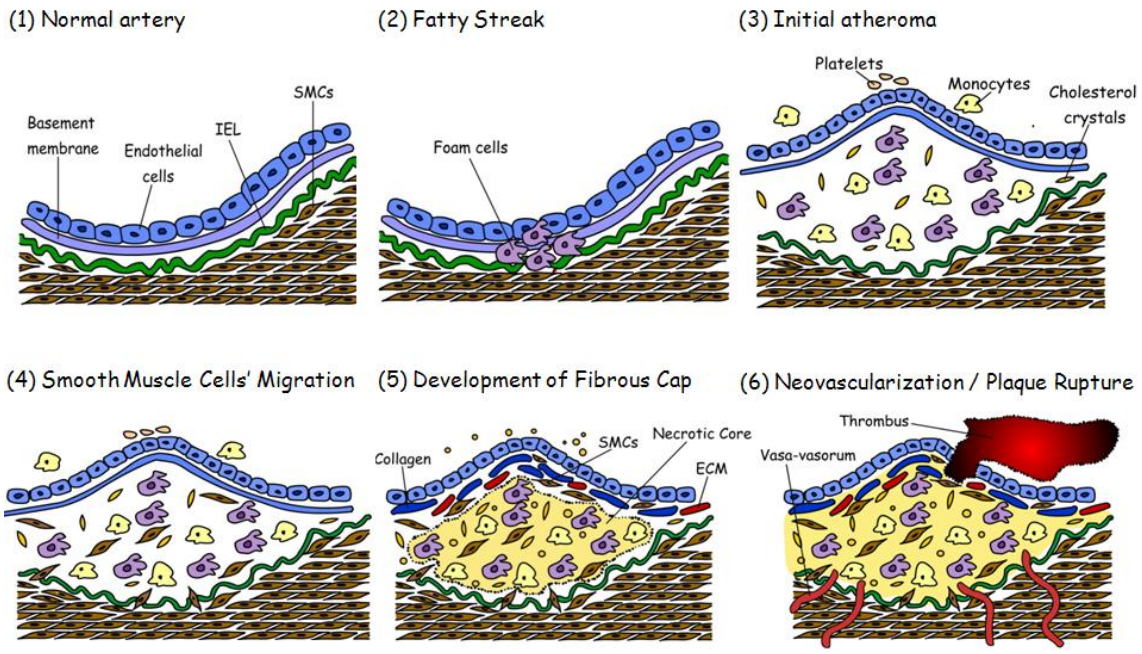


**Figure 2.2:** Progression of atherosclerotic lesions. The normal artery (1) starts to show an accumulation of foam cells, formation of fatty streaks (2); these fatty streaks will lead to an initial atheroma (3). As shown in (4), an atherosclerotic plaque has a core made up of dead foam cells (lipid-engorged macrophages and smooth muscle cells) covered by a fibrous cap (a region of the intimal layer that has thickened as a result of medial smooth muscle cells depositing collagen and elastin fibers); (5) the thickening artery wall of an atherosclerotic plaque gradually encroaches upon the luminal space and can eventually result in a restriction to the blood flow. Unstable plaques, which are susceptible to rupture, are softer and have a thinner fibrous cap. (6) Plaque rupture triggers the formation of a blood clot, which can block the flow of blood through the artery. (© L.Mostaco-Guidolin, 2014)

This lipid-rich necrotic core is separated from the blood by the remaining fibrous cap, rich in **SMC**s and **SMC**-derived collagen [55]. Thrombosis can be triggered by fracture of the fibrous cap, exposing the tissue factor gruel from the core of the lesion, or by endothelial erosion, exposing the sub-endothelial collagen, thereby starting platelet aggregation [56]. The resulting acute ischemia often is the first clinical presentation of atherosclerotic burden and by then atherosclerosis has already progressed to an advanced stage [57].

Although biomedical research considerably increased our knowledge on the pathobiology of atherosclerosis, many facets and causal relations remain unexplained or unexplored. A better understanding of many etiologic factors is important for the development of strategies that could identify atherosclerosis prone individuals and stabilize, or

even regress, existing lesions, therefore preventing or treating atherosclerosis in general and acute ischemic events in particular.

### 2.1.2 Hemodynamic forces as the key behind plaque accumulation

Atherosclerotic lesions show a remarkably consistent pattern distribution throughout the arterial lumen, being mostly confined to branch points of large and middle sized arteries [58]. Typical sites of atherosclerotic burden include the carotid bifurcation, aortic arch, coronary arteries, the aorta near branch points of intercostal, renal and mesenteric arteries, as well as the iliac bifurcation. A simplified scheme, illustrating these main points is presented in Fig. 2.3. These sites correspond to deviant hemodynamic conditions compared to the laminar flow pattern that is found in the greater part of the vasculature [59].

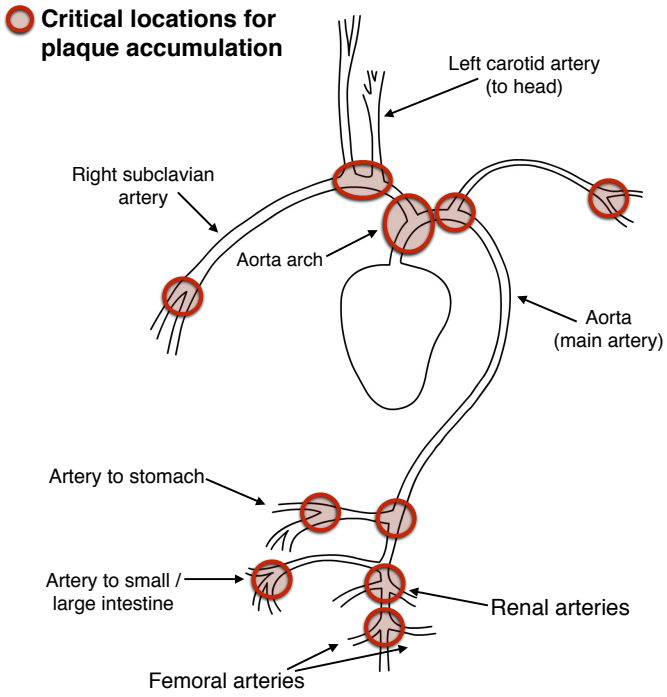


**Figure 2.3:** Scheme illustrating main arteries found in mammalians. Typical sites of plaque accumulation include the (a) carotid bifurcation, (b) aortic arch, the aorta near branch points of (c) intercostal, (d) renal and mesenteric arteries, as well as the iliac and (e) femoral bifurcation. (© L.Mostaco-Guidolin,2014)

The turbulence that occurs at these sites causes low and oscillatory shear forces on

the endothelium. These biomechanical effects change both the geometry of endothelial cells and the gene expression profile [60, 61]. While the high shear stress of laminar flow promotes the expression of atheroprotective genes [62,63], low and oscillatory shear stress induces the expression of various cell adhesion molecules (e.g. **VCAM-1**, **ICAM-1**) [64,65], chemokines (**MCP-1**) [66], cytokines [62], growth factors [67] and enzymes (**NADH** oxidase, **MMP-9**) [68], that are involved in atherosclerotic plaque development and progression. In the second part of this study, experiments involving tracking the accumulation of adhesion molecules on vessel wall were performed, to identify high-risk locations for plaque development.

Another important point that should be highlighted is that in advanced lesions, circumferential stress from high arterial blood pressure not only affects gene expression, but also directly affects the structural integrity of the protective fibrous cap. The fibrous cap of advanced atheromas gradually becomes thinner (and weaker) at the plaque shoulders, and ultimately the fibrous cap ruptures. As a consequence, the thrombotic content of the necrotic core is left uncovered for the blood [69–71]. The latter may result in thrombus formation which can occlude the artery, often causing acute ischemia in downstream organs, which may result in loss of function, and ultimately in death.

### 2.1.3 Animal model - WHHLMI rabbits

In this thesis, myocardial infarction-prone Watanabe heritable hyperlipidemic rabbits, designated as **WHHLMI** rabbits [72, 73], were used as an animal model to mimic spontaneous myocardial infarction in humans. Due to a hereditary defect in **LDL** (low density lipoprotein) processing, **WHHLMI** rabbits develop atherosclerotic plaques without requiring a modified diet. Similar to human Familial Hypercholesterolemia, LDL receptor's function is genetically reduced in **WHHLMI** rabbits and they show hypercholesterolemia [74, 75].

Arterial and cardiac samples from **WHHLMI** rabbits with an age ranging from 0 to 27 month-old were studied. According to several authors [19, 76] aortic atherosclerosis is observed in **WHHLMI** rabbits as early as 2 month-old stage despite feeding them

with normal rabbit chow. At approximately 6 month-old, aortic lesions are expanded to cover about 40% of the aortic surface. Around 10-12 month-old, the lesions cover about 70% of the aortic surface. Above 16 month-old, the aortic lesions cover most of the aorta [19, 76].

Complimentary, coronary atherosclerosis is observed starting from 2 months from they were born. The average coronary narrowing (% of plaque area in the area at the internal elastic lamina) of the circumflex artery reaches about 50% of 6 month, about 70% in 12 month-old, and 80% or higher in 18 month-old and older [77]. In addition, many macrophages and foam cells are observed at the aortic valves.

## 2.2 Nonlinear optical microscopy

During the last several decades, histology has provided detailed insight in various aspects of blood vessel biochemical morphology. However, preparations of histological sections require extensive chemical treatment, pre and post tissue preparation. All of these procedures could result in loss of tissue viability,functionality, and lead to structural alterations.

An imaging technique, which enables simultaneous visualization of both structure and function of the intact and viable diseased vascular wall, is therefore essential. **NLOM** provides a minimally invasive, label free, optical method for fast molecular imaging at sub-cellular resolution with 3D sectioning capability in thick, highly scattering biological tissues [27–30].

In this thesis, three forms of **NLO** microscopic techniques, **TPEF**, **SHG** and **CARS** [30–33] are used to study atherosclerosis progression through tissue imaging. These modalities were chosen due to their respective sensitivity and specificity toward important components of arterial wall and atherosclerotic lesions.

### 2.2.1 TPEF - Two-photon excited autofluorescence

Currently, conventional fluorescence microscopy is the most common optical light microscopy used in biomedical research because of its great specificity, sensitivity, and ease of use. In fact, the comprehensive knowledge of structure and function of the vasculature and vascular diseases such as atherosclerosis is realized in a large part based on studies utilizing conventional fluorescence microscopic techniques.

In conventional fluorescence microscopy, fluorescent molecules (fluorophores) in the sample are excited by absorption of a single photon with a specific wavelength (usually between $350 - 650nm$). Subsequently, the molecules return from the excited state to its ground state by emitting fluorescent light with lower wavelength [1], allowing high contrast imaging of the distribution of fluorophores in the sample with high contrast (Fig. 2.4).

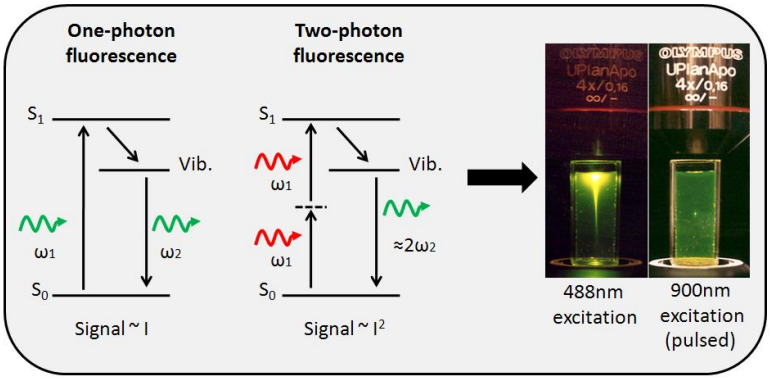


**Figure 2.4:** Schematic energy level diagram illustrating the processes of one and two-photon excitation. Illustration at right: in the two-photon case fluorescence is originated only from molecules excited at the plane of focus, as opposed to the entire focusing cone in the single photon case. *Image adapted from Webb Lab, Cornell University. Adapted by L. Mostaço-Guidolin.*

The process of fluorescence excitation occurs throughout the whole volume that is illuminated by the excitation light. Therefore, out-of-focus fluorescence light also contributes to image formation. It reduces contrast and signal-to-noise ratio, especially in thick and scattering tissues. Furthermore, bleaching of the fluorescent molecules not only occurs in the focal plane, but in the entire illuminated volume.

In combination with the high flux of excitation light that may cause cytotoxic effects, tissue viability is hampered in the large (illuminated) volume of the sample. Finally,

[1] or lower energy; the difference between both wavelengths is called the Stokes shift.

conventional single-photon fluorescence microscopy lacks sufficient penetration depth to obtain high resolution images beyond the tissue surface. This happens due to the high absorption and scattering of the excitation light as well as of the emitted fluorescence in biological tissue. In order to visualize structures in their natural environment, **TPEF** microscopy is a better alternative.

Developed by Webb *et al.* [30], **TPEF** microscopy has become a valuable tool for biomedical studies. **TPEF** microscopy is based on the principle of two-photon **TPEF** excitation, a process which was first described in 1931 by Maria Goppert-Mayer. Simultaneous absorption of two photons (where the total energy is equivalent to that of a single photon at half the wavelength) leads to the electron excitation of fluorescent molecules in the sample. Since the probability of two-photon absorption depends on the square of the intensity of the incident light, excitation occurs only in a very small volume at the focal position of the microscope lens. Therefore, out of focus absorption and excitation, as in normal or confocal fluorescence microscopy, are negligible. As a result, detected photons are primarily originating from the focal position and thus are independent of scattering. Due to this excitation process, **TPEF** microscopy possesses some interesting features: enhanced depth of penetration owing to the use of a near infrared excitation, good optical sectioning, good axial resolution, and reduced photobleaching and phototoxicity [78–81]. Additionally, compared to a confocal microscope, photon detection is much more effective since even scattered photons contribute to the usable signal.

These features make **TPEF** microscopy a better tool than conventional microscopic techniques for imaging structures located deep in (scattering) tissues such as brain [82, 83], kidney [84–87] and microvasculature [88]. Recently, **TPEF** microscopy was also demonstrated as a valuable tool for imaging blood vessels [89].

The two-photon excitation of a fluorophore involves the simultaneous absorption of two photons, generating an electronically excited state, followed by the subsequent spontaneous emission of another photon (generally lower-energy) at the characteristic wavelength of fluorophore emission. This induced fluorescence signal displays a quadratic dependence on the exciting optical power. The basic equation relating the intensity, $I^2(t)$,

of fluorescent signal emitted per molecule and unit time (in the absence of saturation, self-quenching, photobleaching, or stimulated emission) to the experimental parameters for **TPEF** is given by [90],

$$I^2(t) \propto \frac{\phi}{2}\sigma_2\rho^4, \tag{2.1}$$

where $\phi$ is the fluorescence quantum yield of the molecule, $\sigma_2$ is the two-photon absorption cross-section, and $\rho$ is the incident photon flux density. The factor of 2 in the denominator reflects the fact that two photons are required for each absorption event. Since two-photon excitation is an almost instantaneous process, the peak of incident photon flux density of a pulsed laser source, determines the excitation rate.

The requirement for simultaneous absorption of two photons means that **TPEF** cross-sections typically are very small [91]. As the electron is excited to a real excited energy state it can remain in this state for a finite time (typically a few nanoseconds, dependent on the fluorophore) before returning to its original energy state via fluorescence emission [91, 92].

The effective sensitivity of fluorescence microscopy in thick samples is limited by out-of-focus background signal. This introduces a diffuse background fluorescence that does not encode any spatial information, and which therefore acts to reduce the image contrast. In a confocal microscope, a confocal pinhole is used to reject the out-of-focus background and produce an unblurred image which corresponds to a thin ($< 1\mu m$) "optical section". This greatly reduces the limitation of imaging extended samples and enables high-resolution 3D imaging. **TPEF** is an alternative to confocal microscopy that provides clear advantages for three-dimensional imaging. In particular, two-photon excitation microscopy excels at high-resolution imaging in intact thick tissues such as brain slices, embryos, whole organs, and live animals (intra-vital imaging).

For fluorescence microscopy in relatively thick samples, two-photon excitation often provides the most attractive solution, although complementary three-dimensional fluorescence microscopy methods each have particular benefits that can make them better suited for certain experiments.

Confocal microscopy uses a pinhole to reject out-of-focus background fluorescence. Thus, this technique allows optical-sectioning for three-dimensional imaging in thicker samples than conventional wide-field fluorescence microscopy. However, while the excitation light generates fluorescence throughout the specimen, signal is collected only from the focal plane. The absorption of the excitation light will causes photobleaching and photodamage throughout the specimen, which can cause significant problems, especially in live samples.

The penetration depth in confocal microscopy is also limited by sample scattering of both the excitation and emission photons, as well as absorption of excitation energy. Two-photon excitation provides optical sectioning for three-dimensional imaging, but in contrast to confocal microscopy there is no absorption and fluorescence (and thus no photobleaching and phototoxicity) above and below the plane of focus. Consequently, it can be less perturbing to live samples due to the reduced phototoxicity incurred throughout the sample. In addition, the ability to image at depth in the sample is less degraded by sample scattering of excitation, emission photons, and better collection efficiency.

### 2.2.2 SHG - Second-harmonic generation

The second nonlinear optical process discussed in this chapter is the second-harmonic generation (**SHG**). It is a coherent elastic process where two excitation photons are combined in an optically nonlinear medium, to create a **SHG** photon with a wavelength exactly half of the excitation wavelength. This process is summarized in the energy level diagram shown in Fig. 2.5.

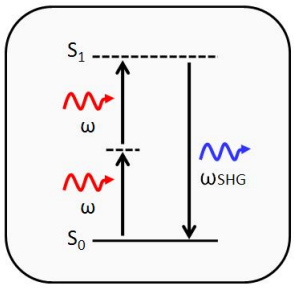


**Figure 2.5:** Second-harmonic generation is a nonlinear optical process, in which two photons interacting within a nonlinear material are effectively "combined" to form a new photon with twice the energy, and therefore twice the frequency, or half the wavelength of the initial photons. *(© L.Mostaco-Guidolin,2014)*

Formally, the equation of the nonlinear polarization is presented in Eq.2.2, showing a polynomial where second-harmonic generation is defined by the second term,

$$\vec{P} = \epsilon_0(\chi^{(1)}.\vec{E} + \chi^{(2)} : \vec{E}\vec{E} + \chi^{(3)}\vdots\vec{E}\vec{E}\vec{E} + \ldots.). \tag{2.2}$$

When the exciting field is a linearly polarized sine wave, we can re-write the Eq. 2.2 as

$$P = \epsilon_0(\chi^{(1)}E_0 \sin\omega t + \chi^{(2)}E_0^2 \sin^2\omega t + \chi^{(3)}E_0^3 \sin^3\omega t + \ldots.), \tag{2.3}$$

where $\chi^{(n)}$ are scalar dielectric susceptibility coefficients. Using trigonometric identities we can simplify Eq. 2.3 to get [93],

$$P = \epsilon_0(\chi^{(1)}E_0 \sin\omega t + \frac{\epsilon_0\chi^{(2)}}{2}E_0^2(1 - \cos 2\omega t) + \frac{\epsilon_0\chi^{(3)}}{4}E_0^3(3\sin\omega t - \sin 3\omega t) + \ldots \tag{2.4}$$

In Eq. 2.4, the $\cos 2\omega t$ term represents the second-harmonic generation and the $\sin 3\omega t$ term represents the third-harmonic generation. The process can also be described quantum mechanically as the combination of two photons with energy $\hbar\omega$ forming a single photon with energy $2\hbar\omega$, where $h$ is the Planck's constant.

There are several factors affecting the magnitude of second-harmonic generation. It depends quadratically on the intensity of the excitation light, and is also affected by the

polarization and wavelength of the excitation light. **SHG** signal can be also dependent on the properties of the material: the nonlinear susceptibility, the phase mismatch between the SHG and the excitation light, and the distribution and orientation of the SHG sources within the focal volume.

An important aspect needs to be pointed out is that **SHG** is polarization sensitive. For many sources of second-harmonic generation, the amount of signal produced is dependent on the polarization state of the incident laser light., relative to the scattering molecular structure.

To illustrate this, we shall focus on the polarization sensitivity of **SHG** from collagen fibrils, as it is the component that will be imaged during the present study. Most studies on the polarization sensitivity of collagen have been carried out on tendon which is composed of highly ordered parallel collagen-type I fibers [94–96]. The intensity of the second-harmonic signal produced from a collagen sample is dependent on the orientation of the polarization state of the laser excitation light with respect to the fiber axis. For a linearly polarized laser beam incident on a collagen fibril, the amount of second-harmonic signal produced for different polarization orientations is summarized in Fig. 2.6.

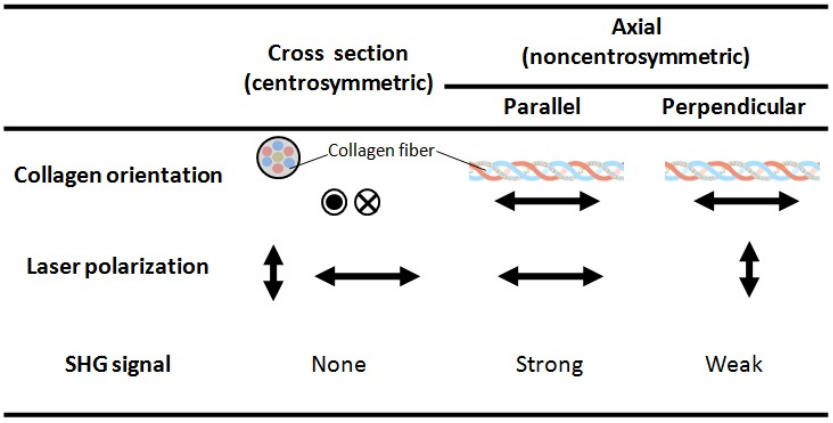


**Figure 2.6:** Summary of the relationship between orientation of collagen fibers and **SHG** signal intensity. The strength of **SHG** signal is dependent on the collagen orientation with respect to the polarization of excitation laser beam.*(© L.Mostaco-Guidolin,2014)*

For fibrils lying in the plane perpendicular to the direction of laser light propagation, the amount of **SHG** produced depends on the angle between the fiber axis and the laser polarization. If the light is polarized along the fiber axis, the maximum **SHG** signal will

be observed. On the other hand, if it is polarized perpendicular to the fiber axis, the weakest **SHG** signal will be observed [97]. This means that the polarization dependence of the **SHG** signal can be measured to study the orientation of the collagen fibrils within tissue [97]. The intensity of the **SHG** signal also depends on the angle between the collagen fiber and the imaging plane. The intensity of the **SHG** is maximum when the collagen fiber is in the imaging plane and very low when the fiber is perpendicular to the imaging plane.

In **SHG** microscopy the focal area in which the **SHG** light is generated has sub-micron dimensions, which is much smaller than the coherence length in collagen. Therefore, the **SHG** signal should not be significantly reduced by destructive interference. **SHG** microscopy has been proved to be an ideal tool to analyze the spatial arrangement of collagen fibers in tissue and quantification. This information can be crucial when dealing with complex medical problems, such as atherosclerotic plaque development.

An interesting point to be noted is that **TPEF** photons can be easily distinguished from **SHG** photons, since **TPEF** is an inelastic process compared to the elastic process of the **SHG**. Therefore, the **TPEF** will always be produced with a longer wavelength than **SHG**, which will always be at a wavelength exactly half that of the laser excitation wavelength. The wavelength of the **TPEF** light is longer than **SHG** because some of the excitation energy is lost during the non-radiative decay.

Unlike **SHG**, **TPEF** is an incoherent process. This means that we do not have to consider the phase mismatch between the **TPEF** and the laser excitation light. **TPEF** is generated out of phase and therefore, no effects of constructive or destructive interference will occur within the focal volume in consideration.

### 2.2.3 CARS - Coherent anti-Stokes Raman scattering

A number of light-scattering phenomena, which can provide structural information are now known and understood. The principal ones and those that are most used are Rayleigh scattering, Raman scattering, hyper-Rayleigh scattering, coherent anti-Stokes Raman scattering, and stimulated Raman scattering.

The third nonlinear optical process used in this study is the coherent Anti-stokes Raman scattering (**CARS**). This is a process in which the contrast mechanism is relying on the molecular vibrations of the sample.

**CARS** enables the extremely weak spontaneous Raman scattering effect to be enhanced by resonance. Raman scattering is an inelastic scattering process involving the vibrational modes of the scattering molecules. Raman spectroscopy has been developed as an analytical technique, allowing different molecules to be identified by their specific vibrational frequencies.

Characteristic peaks occur in the Raman spectra at frequency shifts which correspond to the energy of specific vibrating bonds [32]. There are two types of Raman scattering: Stokes Raman scattering (conventional Raman) and anti-Stokes Raman scattering.

In Stokes Raman scattering part of the energy of the scattered photon is transferred to a vibrating bond of the scattering molecule and the scattered photon consequently has lower energy and therefore leading to longer wavelength.

In anti-Stokes Raman scattering the scattered photon gains energy from a vibrating bond of the scattering molecule under a four-wave mixing condition, consequently leading to shorter wavelength.

The **CARS** signal is generated with a frequency $\omega_{as} = 2\omega_p - \omega_s$, where $\omega_s$ is the Stokes and $\omega_p$ is the pump laser beam. If the frequency difference, $\Omega$, between the frequency of the Stokes beam and the pump beam $(\omega_p - \omega_s)$ corresponds to the frequency of a vibration of a molecular bond within the sample, the **CARS** signal will be strongly enhanced. The energy level diagram for the **CARS** process is shown in Fig. 2.7.

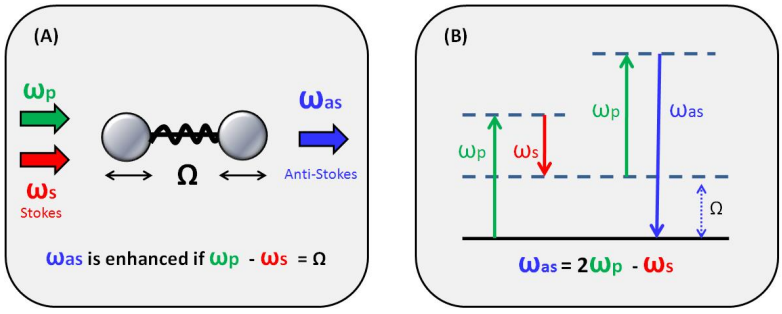


**Figure 2.7:** Energy level diagram for coherent Anti-Stokes Raman scattering. **CARS** is a growing microscopy technique where vibrational energy of molecular bonds is used to visualize the specific molecule in the sample. (© L.Mostaco-Guidolin, 2014)

The major advantage of **CARS** microscopy is that it can be used without staining to image many molecules within the sample which have no intrinsic fluorescence and do not exhibit second-harmonic generation. To produce contrast for a specific molecule, the frequencies of the pump and Stokes photons are tuned so that the difference between them corresponds to a specific vibrational mode which occurs within the molecule (this would be represented by a peak in the spontaneous Raman spectrum). For example, for imaging lipids within a sample, the lasers are tuned so that $(\omega_p - \omega_s)$ corresponds to the vibrational frequency of the CH bonds that exist in large numbers in the hydrocarbon chains of the lipids.

**CARS** is a third order non-linear process and is therefore governed by terms of the third order nonlinear susceptibility tensor $\chi^{(3)}$ . The intensity of the **CARS** signal is quadratically dependent on the intensity of the pump beam, and linearly on the intensity of the Stokes beam,

$$I_{CARS} \propto I_s I_p^2 \left|\chi^{(3)}\right|^2 . \tag{2.5}$$

As the **CARS** intensity is proportional to $\left|\chi^{(3)}\right|^2$ , it is dependent on the square of the number of vibrational modes within the excitation volume. This is due to the coherent nature of the process with all of the vibrational modes oscillating in phase and interfering constructively. This fact increases the specificity of **CARS** when imaging lipids via the $CH_2$ bond vibrations. $CH_2$ bonds exist within most organic molecules, and the hydrocarbon tails of lipid molecules can be found at very high density.

There are three terms in $\chi^{(3)}$, being shown in Eq. 2.6,

$$\chi^{(3)} = \frac{A_R}{\Delta - I\sigma_R} + \chi^{(3)}_{NR} + \frac{A_T}{\omega_T - 2\omega_p - I\sigma_T}. \tag{2.6}$$

The first term represents the enhanced **CARS** signal via resonance when $(\omega_p - \omega_s)$ corresponds to the bond's vibration. The second term is a non-resonant term $\chi^{(3)}_{NR}$, which corresponds to the bulk electronic vibrations. Finally, the third term corresponds to the two-photon enhanced non-resonant contribution.

In Eq. 2.6, $\Delta = \omega_p - \omega_s - \Omega_R$ , with $\Omega_R$ corresponding to the central frequency of the Raman spectral line of vibrational mode being excited with a bandwidth of $\sigma_R$ [32]. $\omega_T$ corresponds to the frequency of an electronic transition and $\sigma_T$ is the band width of this transition. $A_R$ and $A_T$ are constants representing the cross-sections for the Raman scattering and two-photon absorption respectively [98].

The non-resonant term is largely independent of $(\omega_p - \omega_s)$, whereas the contribution of the non-resonant term is dependent on the actual laser frequencies. The contribution of the two-photon enhanced term can be minimized if the laser pump beam is tuned to wavelengths away from those that can excite electronic transitions via two-photon excitation and this is generally true when it is tuned to longer wavelengths [99].

In this way, the expansion of the expression for $\left|\chi^{(3)}\right|^2$ shows that the **CARS** signal is dependent on three terms. When $\omega_p$ is tuned away from the two-photon electronic transitions so that the two-photon enhancement term may be ignored,

$$I_{CARS}(\Delta) \propto \left|\chi^{(3)}_{NR}\right|^2 + \left|\chi^{(3)}_{R}(\Delta)\right|^2 + 2\chi^{(3)}_{NR} Re\chi^{(3)}_{R}(\Delta). \tag{2.7}$$

The first term in this expression represents the non-resonant background. The second term represents the resonant contribution, and hence provides information on the concentration of the resonant scatters within the sample. The last term is a combination of contributions from the resonant and non-resonant terms.

The non-resonant background limits the imaging contrast in **CARS** microscopy. The solvent in which the sample is contained often contributes to the non-resonant background. For example water produces a strong resonant signal with a broad spectral range. In order to distinguish the non-resonant background from the resonant **CARS** signal images need to be taken at different values of $(\omega_p - \omega_s)$ or off resonance.

At this point it is worthwhile to compare the advantages and contrast mechanisms of **SHG**, **THG** (third harmonic generation), and **CARS** microscopy. Multi-harmonic (**SHG** and **THG**) microscopy is advantageous in that it uses one laser beam and it can be easily incorporated with multiphoton fluorescence microscopy. **SHG** arises from samples lacking inversion symmetry. **THG** and **CARS** rely on the third-order suscep-

tibility and require no symmetry breaking. **THG** arises from symmetry breaking at interfaces between different structures and has poor chemical specificity. **CARS** spectra provide rich information about molecular vibration, making **CARS** microscopy often more informative than **SHG** and **THG** microscopy, by allowing vibrational mapping of unstained living cells and tissues, monitoring processes with chemical selectivity. On the other hand, **SHG** and **THG** can provide structural information about the sample.

## 2.3 A multimodality imaging approach

By combining **TPEF**, **SHG** and **CARS** into a common imaging microscope system, multimodal **NLOM** imaging can provide rapid biochemical maps of arterial tissue displaying information on key biochemical components and structures that are associated with atherosclerosis. Quantification of atherosclerosis progression then becomes possible when we combine the visual representation provided by **TPEF**, **SHG** and **CARS** images, and parameters derived from those images.

All the **TPEF**, **SHG** and **CARS** imaging carried out in this study was performed on unstained, un-cut tissue samples. Therefore, it is important to understand and identify the sources of multiphoton contrast in order to properly interpret these images. As discussed in the introduction, the source of **CARS** contrast is obtained from intrinsic molecular vibrations within the samples; the SHG sources are molecules lacking inversion symmetry, and the **TPEF** is from fluorophores which have an efficient two-photon autofluorescence upon excitation at $800nm$.

For tissues investigated in this study, collagen fibril is the main source of **SHG** contrast. **CARS** image contrast is primarily originating from the vibrations of the CH2 bonds in lipids. The source of **TPEF** however is less specific. In the case of healthy artery, the **TPEF** signal detected is most likely coming from elastin fibers, which exist in several vessel layers with different morphology. However, a number of two-photon fluorophores from atherosclerotic plaque can also be excited by the wavelength range used in this work, thus making identification of **TPEF** signals detected in the plaque

more challenging. The tables in Appendix A summarize possible **NLO** signal sources from biological samples.

# Chapter 3

# The NLO microscope, samples & data analysis

## 3.1 The multimodal NLO microscope

Conventional **CARS** microscopy uses picosecond (ps) lasers rather than femtosecond (fs) lasers for its narrower pulse-width. Alternatively, **CARS** microscopy based on a single femtosecond (fs) laser combined with a photonic crystal fiber (**PCF**) can achieve similar performance with important added advantages. By allowing **CARS** to be combined efficiently with other multiphoton techniques (e.g. **SHG**, **TPEF**), it is possible to acquire multimodal imaging without changing laser sources. The combination of a fs oscillator with a **PCF** leads to a natural extension of the existing technology (e.g. multiphoton microscope) [38, 100].

Based on this concept, an in-house developed multimodal **NLO** laser scanning microscope illustrated in Fig. 3.1 [38, 100] was used for **TPEF**, **SHG** and **CARS** imaging of cardiovascular tissues. The light source for **TPEF** and **SHG** imaging is a Ti:Sapphire oscillator (Tsunami, Spectra-Physics) operating at $800nm$ with a $100fs$ pulse duration and $20nm$ bandwidth. Average output power was measured to be $1W$ when the oscillator was pumped with a $7.25W$ of green light at $532nm$ (Millennium Pro, Spectra-Physics). A Faraday isolator (Newport) was placed close to the emission exit of the Ti:Sapphire

oscillator to prevent any back-reflections of the femtosecond pulses from re-entering the laser cavity. Re-compression of the pulses was accomplished using a pair of chirped laser mirrors (Layertec GmbH, Germany) to compensate for the large positive group velocity dispersion (**GVD**) introduced by the Faraday isolator and other microscope optics. The femtosecond pulses were then split into two beams using a 50 : 50 beam splitter.

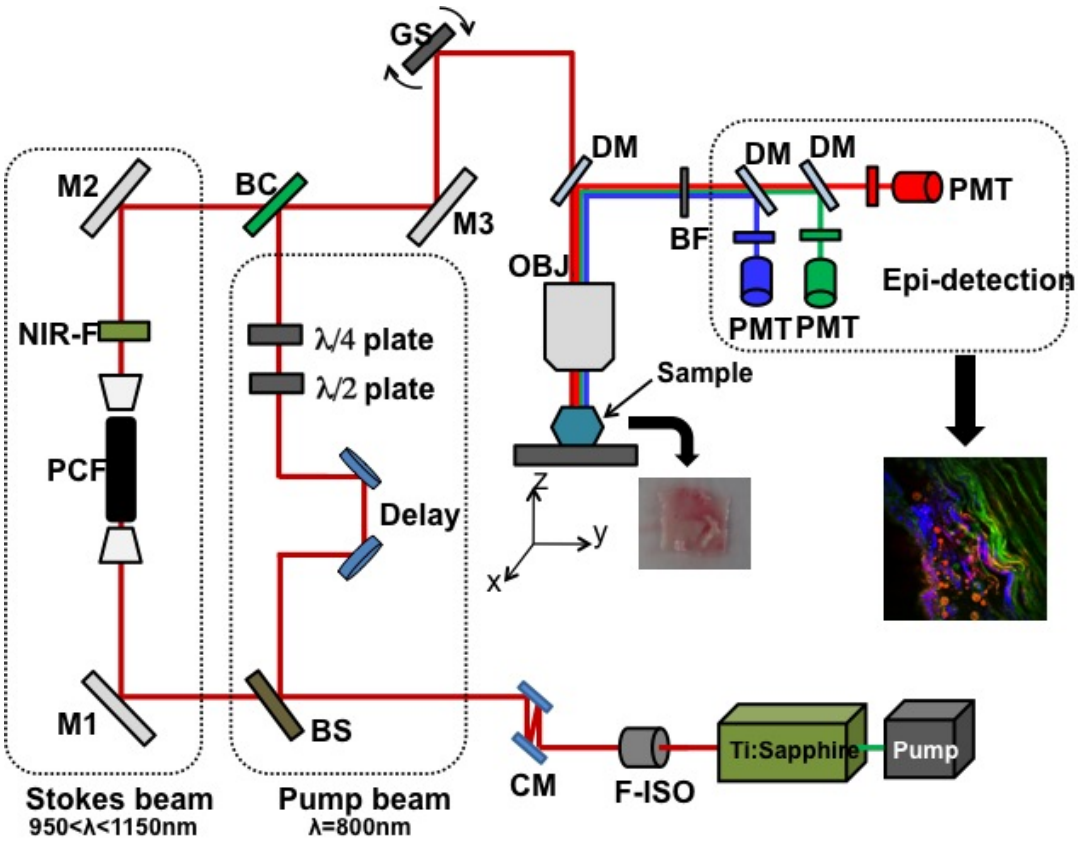


**Figure 3.1:** Schematic illustration of the home-built multimodal nonlinear optical laser scanning microscope. Light source for **TPEF** and **SHG** imaging is a Ti:Sapphire femto-second oscillator (Tsunami,Spectra-Physics). For **CARS** imaging, Stokes pulses are generated in PCF which is pumped by the same Ti:sapphire laser. M1,M2,M3: mirrors; **F-ISO**: Faraday isolator; **CM**: chirp laser mirrors; **BS**: beam splitter; **NIR-F**: near-IR filter; **GS**: galvo scanner; **DM**: dichroic mirror; **OBJ**: objective lens; **BF**: bandpass filter; $\lambda/4$: quarter waveplate; $\lambda/2$: half waveplate; **PMT**: photomultiplier tube.*(© L.Mostaço-Guidolin,2014)*

The reflected beam of the BS was used as the pump beam for **CARS** imaging and also as the light source for **TPEF** and **SHG** imaging. Approximately 300 mW of transmitted power after the beam splitter was coupled into a **PCF** (NL-1.4-775-945, NKT Photonics A/S, Denmark) through a 20× objective lens (Newport), generating a broadband emission both in the visible and in the near infrared (**NIR**). The **NIR**

portion ($> 900nm$) of this broadband emission was used as the Stokes beam for **CARS** imaging. Typically $25mW$ of pump and $8mW$ of Stokes (measured after the $20\times$ air objective lens) were used for imaging.

The pump and Stokes pulses were combined at a beam combiner before proceeding into the laser scanning microscope assembly co-linearly. An air objective lens focused the laser pulses on samples, collecting the epi (i.e. backward) or forward **TPEF/SHG/CARS** signals.

The collected **NLO** signals were transmitted to three non-descanned **PMT** detectors (H9656 series, Hamamatsu, Bridgewater, NJ, USA) mounted on the microscope assembly for simultaneous **TPEF**, **SHG** and **CARS** imaging at $530 \pm 20nm$, $400 \pm 30nm$ and $630 \pm 30nm$, respectively. A schematic representation showing more details for the detection is presented in Fig. 3.2.

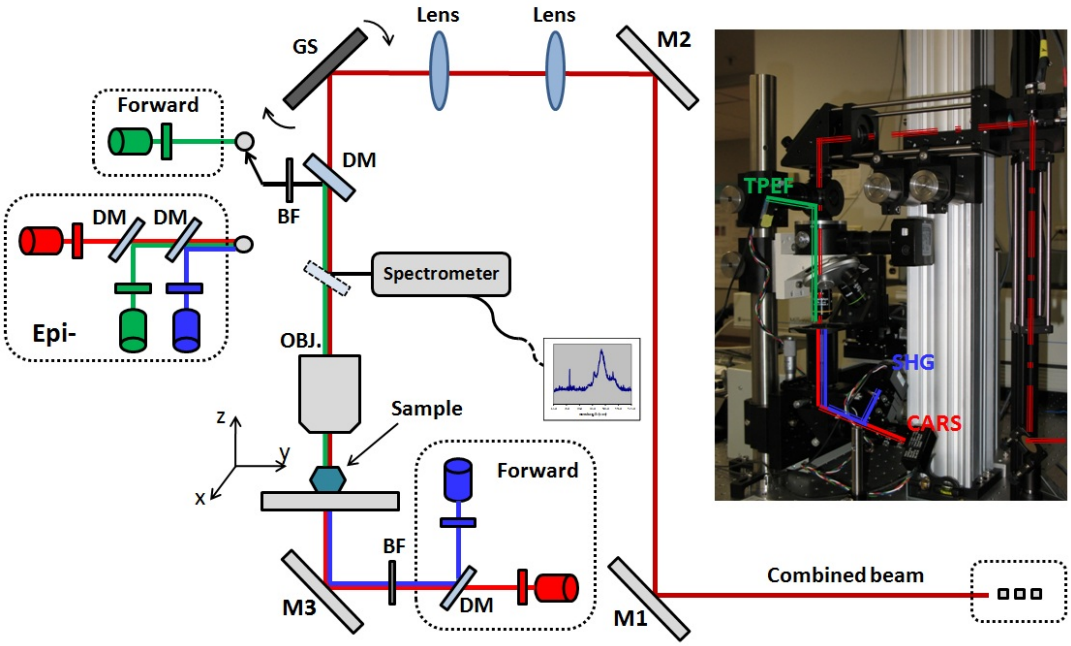


**Figure 3.2:** Illustration showing details of two configurations used in this study. Most bulk-tissue imaging was accomplished using backscattered (epi-) configuration. However, an alternative forward-**CARS** and forward-**SHG** configuration was used to image thin-sections of arterial vessel. Additionally, a spectrometer is also coupled to the system, allowing acquisition of spectra from a specific sample location. M1,M2,M3: mirrors; **GS**: galvo scanner; **DM**: dichroic mirror; **OBJ**: objective lens; **BF**: bandpass filter; **PMT**: photomultiplier tube. *(© L.Mostaço-Guidolin, 2014)*

The laser light, after passing through the microscope objective lens, was focused on

a region of interest by moving the sample using a motorized translation stage (Sutter Instrument, Novato, CA, USA). This 3-axis stage was controlled by a motor controller (MP-285, Sutter Instrument, Novato, CA, USA) and had a resolution of $0.2\mu m$. The translational stage also allowed 3D image stacks to be built up at incrementally moving the sample at a set distance along the z-axis between each 2D raster scans.

The two objective lenses used for bulk tissue imaging included a $20\times$, $0.75NA$ infinity corrected air objective lens (Olympus Canada, Markham, ON, Canada) and a $10\times$, $0.40NA$ infinity corrected air objective lens (Olympus Canada, Markham, ON, Canada) with the majority of the imaging work done with the $20\times$, $0.75NA$ infinity corrected air objective lens, which gave a maximum scan size of approximately 450x450$\mu m$. ScanImage (ver.3.5) software [101] was used for image acquisition and laser scanning control. Typical pixel dwell time for an average of 4 scans for a single frame collection was $21\mu s$.

## 3.2 Tissue and sample preparation

The animal study was approved by the local Animal Care Committee at National Research Council Canada - Winnipeg. Arterial samples were harvested from 28 **WHHLMI** rabbits aged from 0 to 27 month-old. This sampling provides good representation of atherosclerotic disease progression, with the 27 months rabbit being considered to be nearing the end of its life cycle (it died of natural cause).

During the harvest, segments of tissue starting from the ascending aorta to the external iliac artery were excised from all specimens and then rinsed in heparinized saline. The exterior surfaces of these aorta sections were delicately cleaned of connective tissue prior to being subdivided into four tissue pieces. Each of these segments represents a specific location along the artery: *aorta arch (***AA***)*, *thoracic artery (***TA***)*, *abdominal artery (***AbA***)*, and *external iliac artery (***EIA***)*, as shown in Fig. 3.3.

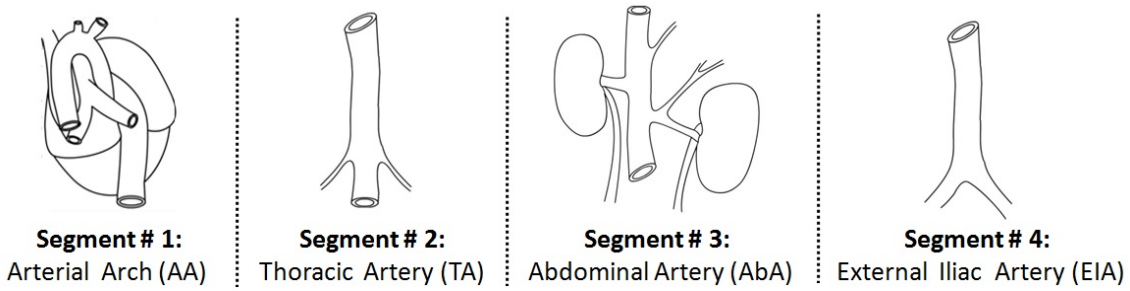


**Figure 3.3:** Main aorta segments used in this study. The first segment is called aorta arch (**AA**); the second one is the thoracic artery (**TA**); the third and the fourth segments were named as abdominal artery (**AbA**) and external iliac artery (**EIA**), respectively. *(© L.Mostaço-Guidolin, 2014)*

Additionally, short segments from each piece were set aside for histology and **IHC**. Each artery segment was cut open longitudinally exposing the luminal surface. A schematic illustration of this procedure is shown in Fig. 3.4.

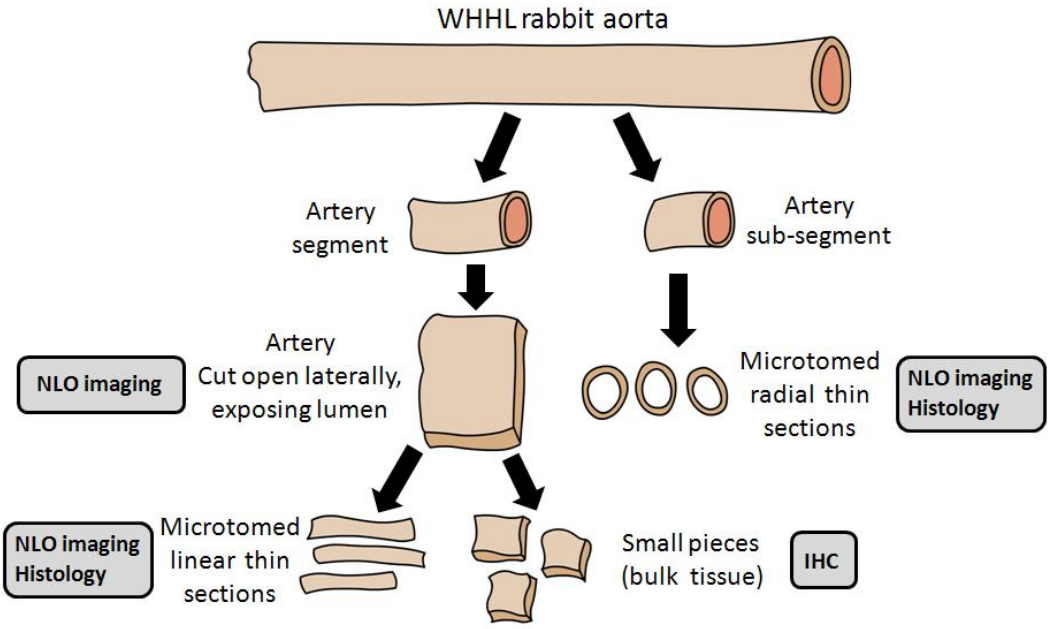


**Figure 3.4:** General view of sample cutting . The aorta is divided in four segments (as mentioned earlier); each segment is further divided in smaller pieces to be used for imaging (**IHC**) experiments. Some artery subsegments are also stored and prepared for histology. *(© L.Mostaço-Guidolin, 2014)*

The samples were placed in petri-dishes with the luminal surface facing up on a moist surface. Hydration was maintained throughout the measurements by periodically applying phosphate buffered saline (**PBS**) solution onto sample surface. Digital photographs were acquired and regions of interest were identified prior to measurements.

## 3.3 NLO imaging and histology of artery

For histology, the artery was cross-sectioned on a cryotome into sections while embedded in Optical Cutting Temperature medium. The tissue sections prepared for **NLO** imaging received no further treatment after cutting while those prepared for histology were immersion-fixed in either 95% methanol or 10% buffered formalin based on individual staining protocols. Artery sections used in multimodal **NLO** imaging were compared to adjacent H&E (hematoxylin and eosin) stained sections which revealed general tissue morphology, picro-sirius red stained sections highlighting collagen and elastin fibers under cross-handed circularly-polarized condition [102], and oil red O staining accenting high-lipid structures. Histology images were obtained using a 10x air objective lens on a Zeiss Axio Observer Z1 system equipped with AxioCam ICc3 **CCD** camera (Carl Zeiss Canada, Toronto, ON, Canada).

**NLO** images from sections of the aorta vessel were characterized through a visual comparison with histological images from matched sections, and an example is shown in Fig. 3.5.

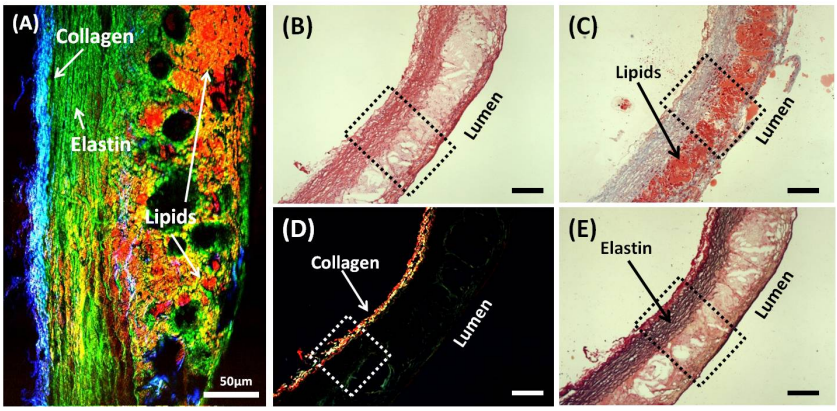


**Figure 3.5:** Atherosclerotic plaque features and its major components visualized by (A) **NLO** microscopy, where the elastin fiber is color-coded in green (**TPEF**), collagen fibrils in blue (**SHG**) and lipids in red (**CARS**). Both **SHG** and **CARS** signals are collected in the forward-direction while **TPEF** is collected in the backscattered (epi-direction). Histological images of adjacent artery sections stained with (B) H&E (bright field), and (C) oil red O (bright field). The section in (D) and (E) is double stained with picro-sirius red (collagen) and Verhoeff's (elastin). (D) was imaged using circular polarized light to detect the collagen fiber stained by picro-sirius red and, in (E) the bright field image captures the elastin fibers stained black by the Verhoeff's. *Reproduced with the permission from IOP Publishing Ltd (2011) [16]*

The good correspondence between the histological sections and the multimodal **NLO** images validates our understanding of what gives rise to imaging contrast in the multimodal **NLO** images of the vessel wall.

## 3.4 Immunohistochemistry: locating inflammation sites within the artery

Antibodies (also called immunoglobulins, or **IgG** molecules) are used by the immune system to attack foreign substances, called antigens, that enter the body. This property can be used to generate antibodies of clinical interest. For example, if an antigen from human cells is injected into a rabbit, the rabbit's immune system will produce specific antibodies against that antigen. The resulting rabbit antibodies can then be withdrawn, purified, and applied to human tissue specimens to identify the location of the antigen within a cell.

Antigens are typically proteins or polysaccharides within or on the surface of cells. Antibodies bind specifically to the antigen that triggered the antibody's production and, as a result, immunohistochemical reactions can be very precise.

To identify the location of the bound antibody, and thus the location of the antigen, we can use a procedure called the direct method. In this method, the antibody is attached (or conjugated) to an indicator molecule. Different indicators include biotin, horseradish peroxidase (HRP), or in this case, fluorescent molecules, as shown in the diagram presented in Fig. 3.6. In the direct method, the purified conjugated antibody is applied to the tissue and allowed to react with the antigen. Unbound antibody is washed away. In the case of atherosclerosis, certain types of cellular adhesion molecules are identified as indicating antigen.

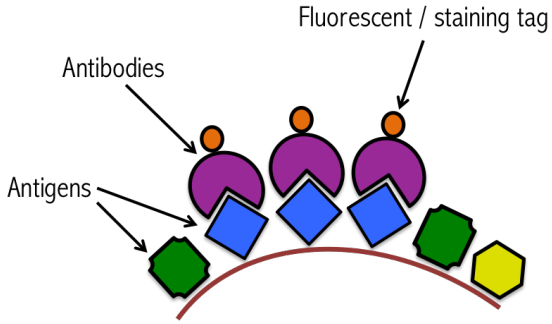


**Figure 3.6:** Simplified diagram showing the basic idea behind immunohistochemistry experiments. Antigens are typically on the surface of cells. Antibodies bind specifically to the antigen that triggered the antibody's production and, by attaching a fluorescent molecule it is possible to located precisely sites of interest. (© L.Mostaço-Guidolin, 2014)

Binding and recruitment of circulating leukocytes to the vascular endothelium and further migration into the sub-endothelial spaces are major processes in the development of atherosclerosis and are mediated through a diverse family of cellular adhesion molecules that are expressed on the surface of vascular endothelial cells [103].

Among all identified adhesion molecules, the expression and biological properties of intercellular adhesion molecule 1 (**ICAM-1**) are well characterized [104–106]. **ICAM-1** concentration is elevated during inflammatory conditions in which detailed pathology studies have documented increased expression of cellular adhesion molecules on endothelial cells and other tissue types [107, 108].

Bulk tissue **IHC** tests based on near-IR fluorescence imaging of **ICAM-1** were carried out in order to confirm and quantify the plaque severity at various locations along the aorta. These experiments were important to validate the results obtained by our *in-house* developed index for quantifying plaque burden.

The protocol adopted can be found elsewhere [106]. In summary, frozen arterial tissue samples were cut into smaller segments and then fixed for 10 minutes at room temperature in methanol (MeOH). Samples were then washed three times with phosphate-buffered saline (**PBS**) followed by incubation in a 10% normal goat serum solution (in **PBS** with 0.03% Triton) at room temperature for 1 hour and then washed once with **PBS**. Samples were then incubated overnight with 1:250 solution of Cy5.5 labelled **ICAM-1**.

Samples were washed again with PBS and kept in PBS until imaging. After imaging, samples were stored in the -80°C freezer. The Cy5.5 dye present in ICAM-1 was stimulated with an array of light emitting diodes emitting at 675 nm. The fluorescence was obtained at 700 nm and the images were acquired using a Photometrics **CCD** camera at 1 second acquisition time, defined after testing the signal-to-noise ratio for each sample. The **CCD** camera was equipped with a 700 nm bandpass filter.

All of the fluorescence data collected were analyzed using Matlab. The region containing the sample in each image was segmented, in order to consider only the pixels which were carrying information regarding the sample itself. In other words, the background area where no sample was present was not counted. The mean fluorescent intensity for each image was computed by averaging over all pixels carrying the sample's fluorescence information.

## 3.5 Data analysis: an overview

The data analysis comprised of two parts and can be summarized in Fig. 3.7. The post image processing, feature extraction, statistical analysis, and classification were performed in ImageJ ver1.42b, Fiji, [R], Origin 8.0, and Matlab.

The first part, related to the general characterization of atherosclerotic plaques and its progression, was mostly based on signal intensity [1] of images acquired from each modality. The intensity-based information acquired through each **NLO** technique was combined, and formed the basis of a new optical index for quantifying plaque burden (denominated **OIPB**). Detailed methodology and results will be discussed in Chapter 4.

Additionally, texture analysis of images acquired from all three modalities was also performed. The goal is to test if such analyses of **NLO** images can extract additional information relevant to the understanding of atherosclerosis progression in rabbit model. The results are presented in Chapter 5.

[1] Although some textural parameters are not simply intensity-based, most of the results presented in the first part of this thesis are, and were used to better characterize atherosclerotic lesions.

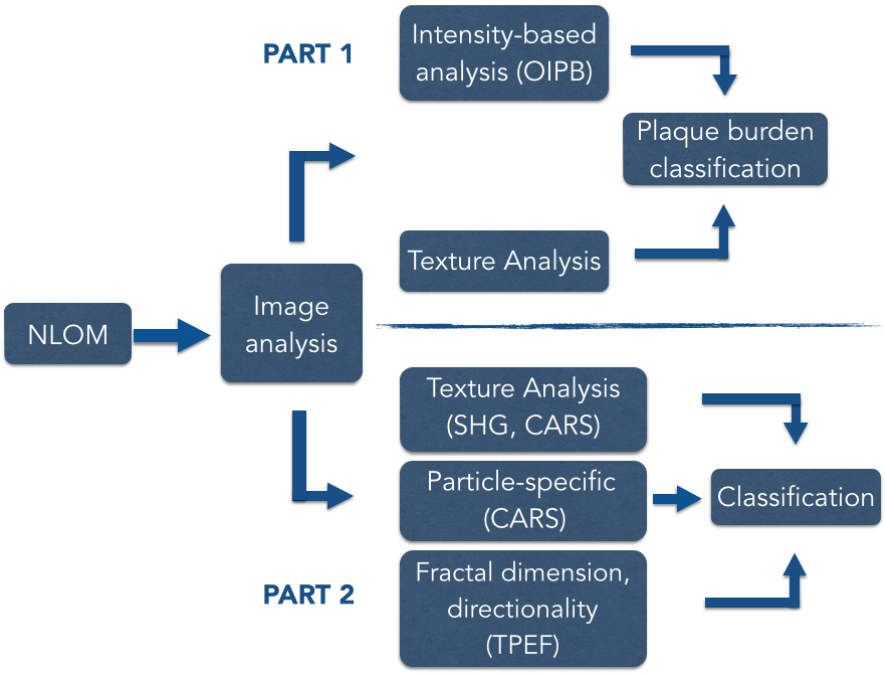


**Figure 3.7:** Simplified chart of data analysis performed in each part of this thesis. **NLO** images were analyzed using two approaches: the calculations of the **OIPB** index and the extraction of individual parameters from **NLO** images acquired by each modality. *(© L.Mostaço-Guidolin, 2014)*

The second part of this study investigated specific methods that can be used to extract morphological information presented in those **NLO** images acquired in each imaging modality. In addition to texture analysis, an other two imaging analysis methods, particle and fractal dimension, were tested for their potential in decoding these images. Details are provided in sections 3.5.1, 3.5.2, and 3.5.3. Image classification was also attempted using **SVM** methods, which is to be discussed in detail in section 3.5.5.

### 3.5.1 Texture analysis: an efficient way to look at all NLO images

Ten texture parameters were determined using the histogram or gray level co-occurrence matrix (**GLCM**) of the image. The "co-occurrence matrix" represents the probability of occurrence of a pixel pair, with a given gray-tone difference, separated by predefined distance taken in a predefined direction. In comparison, the image "histogram" is the frequency of occurrence of a gray tone in an investigated region.

Image first-order statistics are not textural features because only the intensities of individual pixels are considered independently from their neighboring pixels. These first-order statistics merely describe the gray levels of the histogram corresponding to an image. Among these parameters, five were selected for further analyses (the mean, standard deviation, integrated density, skewness, and kurtosis), as they have demonstrated better correlation in preliminary tests.

The mean and integrated density provide measures of the overall lightness/darkness of the image, while the standard deviation describes its overall contrast. The skewness quantitatively evaluates the asymmetry of the shape of the distribution of pixel intensities around mean value of the histogram while the kurtosis measures the peakedness of the distribution relative to the length and size of the histogram tails.

On the other hand, image second order statistics measures the spatial arrangement of the gray levels present in the region of interest and provide textural information for that region. Co-occurrence matrices are commonly used to describe the second order statistics of an image. This method is based on the estimation of the second order joint conditional probability density functions $P_{d,\theta}(i,j)$, where $P_{d,\theta}(i,j)$is the probability of going from a grey level $i$ to a gray level $j$ in a given direction $\theta$ at a given inter-sample spacing $d$.

The co-occurrence matrix $P_{d,\theta}(i,j)$ is a representation of the estimated values. It is a square matrix of dimension $N_g$ ($N_g$ is the number of gray levels in the image). A number of texture features can be defined based on the co-occurence matrix $P$.

A set of fourteen features, defined by Haralick *et al.* [109], were studied for their potential in relating multimodal **NLO** images to vessel wall morphology. These were the angular second moment, inertia, correlation, variance, inverse difference moment, sum average, sum variance, difference variance, sum entropy, entropy, difference entropy, information measures of correlation one, information measures of correlation two, and maximum probability. However, in a preliminary study, only five of them were found to be useful in the context of characterizing structures in the **NLO** images of the vessel wall. Therefore, only the results obtained using the energy, inertia, correlation, inverse

difference moment, and entropy texture features are reported. The mathematical expressions defining the **FOS** and the **GLCM** parameters to be used in thesis are given in table 3.1.

| Category | Textural Feature | Expression |
|---|---|---|
| FOS | Mean | $\sum_{i=0}^{N-1} i \sum_{j=0}^{N-1} P_{i,j} = \sum_{j=0}^{N-1} j \sum_{i=0}^{N-1} P_{i,j}$ |
| FOS | Standard deviation | $\sum_{i=0}^{N-1}(i-\mu)^2 \sum_{j=0}^{N-1} P_{i,j}$ |
| FOS | Integrated density | $\sum_{i=0}^{N-1} n(N_i)$ |
| FOS | Skewness | $\sigma^{-3} \sum_{i=0}^{N-1}(i-\mu)^3 P_i$ |
| FOS | Kurtosis | $\sigma^{-4} \sum_{i=0}^{N-1}(i-\mu)^4 P_i - 3$ |
| GLCM | Energy | $\sum_{i,j=0}^{N-1} P_{i,j}^2$ |
| GLCM | Correlation | $-\sum_{i,j=0}^{N-1} P_{i,j} \left[\frac{(i-\mu)(j-\mu)}{\sigma^2}\right]$ |
| GLCM | Inertia | $\sum_{i,j=0}^{N-1}(i-j)^2 P_{i,j}$ |
| GLCM | Inverse Difference Moment | $\sum_{i,j=0}^{N-1} \frac{P_{i,j}^2}{1+(i-j)^2}$ |
| GLCM | Entropy | $-\sum_{i,j=0}^{N-1} P_{i,j} \log P_{i,j}$ |

**Table 3.1:** General description of each image feature used in this thesis. **FOS**: first order statistics; **GLCM**: gray level co-occurrence matrix; $\sigma$ corresponds to the standard deviation. *(© L.Mostaço-Guidolin, 2014)*

The co-occurrence matrix was calculated in four orientations: horizontal, vertical, and the two diagonals (directions defined by four angles: 0°, 45°, 90°, and 135°), and then the average value was obtained. A window size with eight pixels was adopted to extract features from 16 bit images.

Extraction of textural features were obtained by using a custom-built texture analysis toolkit. This toolkit contains some of the texture analysis functions available in the Matlab image processing toolbox as well as ImageJ's histogram analysis toolbox .

### 3.5.2 Particle-specific features

Particle-specific features were determined to be a better method to evaluate lipid-rich structures due to their common round/oval shapes. The aspect ratio, Feret diameter, density and number of particles were calculated for all **CARS** images and then used as additional parameters to help classifying the images. A short description of each feature is presented below.

### Object identification

The number of particles (or, in this case, lipid-rich structures) was defined by setting a threshold on the image; subsequently, all pixels which intensity is above the threshold are be considered as object's pixels whilst other pixels are considered as background [110].

On the first pass, the image will be scanned from its top left corner to its lower right corner. When the first object's pixel is found, a tag is given to it. The tag is a unique number which will be carried by all pixels constitutive of the same object. While the scan process goes on, each time a new object's pixel is found, its previous neighbours are checked for an existing tag. The lowest tag found in the surrounding is then attributed to this current pixel. Fig. 3.8 illustrates the connexity analysis process.

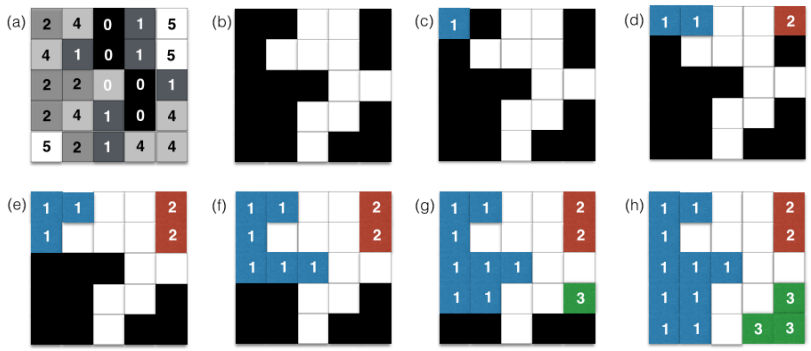


**Figure 3.8:** Summary of the process of object identification: (a) original image; (b) binarized image; (c) a tag is given to the first object's pixel found; (d) tagging of the first line; (e) tagging of the second line; (f) tagging of the third line; (g) tagging of the forth line; (h) tags' map. *(© L.Mostaço-Guidolin, 2014)*

On the second pass, ambiguities are resolved. For instance, when a U-shaped object is found, its two branches are tagged separately during the first pass as the two branches are only connected by their bottom parts. The same object is therefore considered as two. During this regulation process, two adjacent pixels carrying two different tags are detected and the higher tag is replaced on the full image by the lower tag.

Once objects are defined, the density is calculated by dividing the total number of identified objects by the total number of pixels in each image.

### Feret diameter

The Feret Diameter is the longest (maximum diameter) or the shortest (minimum diameter) distance between any two points along the selection boundary, also known as maximum caliper. It is deducted from the projected area of the particles using a slide gauge. In general, it is defined as the distance between two parallel tangents of the particle at an arbitrary angle. Figure 3.9 illustrates the possible definitions of Feret diameters.

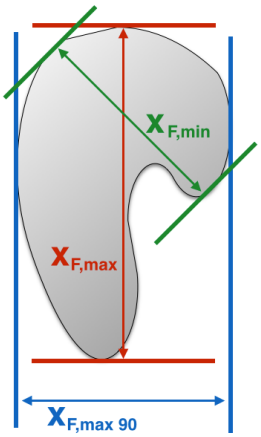


**Figure 3.9:** Schematic illustrates the definitions of Feret diameters. *(© L.Mostaço-Guidolin, 2014)*

The possible values that can be obtained are the minimum $x_{F,min}$ and maximum Feret diameter $x_{F,max}$; the mean Feret diameter and the Feret diameters obtained at 90 degrees to the direction of the minimum or maximum Feret diameters (defined as $x_{F,max90}$). The minimum Feret diameter is often used as the diameter equivalent to a sieve analysis.

### Aspect ratio (AR)

Finally, the aspect ratio (**AR**) ($0 < AR \leq 1$) is defined by the ratio of the minimum to the maximum Feret diameter,

$$AR = \frac{x_{FeretMin}}{x_{FeretMax}}. \tag{3.1}$$

It gives an indication for the elongation of the particle. Some literature also uses

$1/AR$ as the definition of sphericity. A value of 1.0 indicates a perfect circle. As the value approaches 0.0, it indicates an increasingly elongated shape [111].

### 3.5.3 Fractal dimension

The structure of the fibers in biological tissues, such as elastin and collagen, are commonly disrupted or damaged during injury, aging, and pathological processes. Quantification of these changes is traditionally a laborious and subjective task. However, fractal dimension analysis can be applied to quantify the organization of fibers in a very efficient way.

The word "fractal" describes a pattern that repeats as it gets smaller. Figure 3.10 shows examples of this repeating self-similarity. One well-known is the Koch Curve (also known as the Koch Snowflake), in which four lines of equal length are arranged so that they are the length of only three segments and then four of the line groups are treated the same way (Fig. 3.10b).

There are many well-known fractals occurring in multiple dimensions, including the Sierpinski Triangle (Fig. 3.10c), and the more complex Julius and Mandelbrot Sets. Fractals are also commonly seen in nature: snowflakes, cloud shapes, trees [112, 113], artery branching [114], and respiratory structures [115]. Each of these fractal patterns has a degree of self-similarity that can be measured using a fractal number.

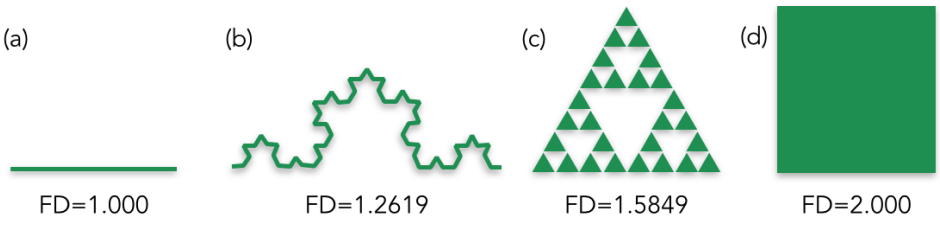


**Figure 3.10:** Examples of fractals with dimensions. a) A line is one-dimensional [Fractal Dimension = 1.0000]; b) the Koch Curve is somewhere between one and two dimensions [D = 1.2619]; c) The Sierpinski triangle is closer to two dimensions than the Koch Curve [Fractal Dimension = 1.5849]; d) a solid rectangle is two-dimensional [Fractal Dimension = 2.0000]. *(© L.Mostaço-Guidolin, 2014)*

A fractal number describes the amount of space and self-similarity of the structure. For example, a line exists in a single dimension, therefore it has a fractal dimension of

1 (Fig. 3.10a), while a square exists in two dimensions and has a fractal number of 2 (Fig. 3.10b). A simple fractal like the Koch Curve has more "dimension" and self-similarity than a line but not as much as a square, so its fractal dimension is 1.26, and the Sierpinski Triangle, which is closer to a square than the Koch Curve has a greater fractal dimension of 1.58. Fractal analysis has been applied in several different biological and medical applications, such as tumour characterization, cellular deposition, among others, and it serves as a good descriptor to evaluate elastin and collagen fibers [116].

### Box counting dimension

Several approaches have been developed to estimate the fractal dimension of an image. Of the wide variety of methods, the box-counting method is one of the most widely used [113], as it can be applied to patterns with or without self-similarity.

The box counting method partitions the image space into square boxes of equal size. The box covers the image space of the function or pattern of interest and the number of boxes that contain at least one pixel of the function is counted. The process is repeated with different box sizes.

The fractal dimension is obtained from the slope of the best fitting straight line to the graph plotting the log of the number of boxes counted versus the log of the magnification index for every stage of partitioning. For example, an image measuring size $M$x$M$ pixels in size is scaled down to $s$x$s$, where $1 < s < M/2$, and $s$ is an integer. Then, $r = sM$.

Fractal dimension D is given by,

$$D = \frac{\log(N_r)}{\log(1/r)}, \tag{3.2}$$

One possible limitation of this method is that different textures may have the same fractal dimension. This may be due to combined differences in coarseness and directionality i.e. dominant orientation and degree of anisotropy. For the specific case illustrated here, fractal dimension showed favorable results, as they will be presented and discussed in the following sections. However, if needed, the combination of methods (e.g. texture analysis, directionality, etc) can be helpful to achieve better accuracy in other applica-

tions of evaluating **TPEF** objects.

### 3.5.4 Fiber directionality

In the past, directional filters have been developed in the frequency domain using the Fourier transform (**FT**) to extract linear pattern information from an image. Using the linearity and rotation properties of FT, an image can be decomposed into components lying in different directions. Extracting components in an angle band from the Fourier transformed image is equivalent to extracting, from the original image, the components lying in the corresponding orthogonal angle band. In an effort to develop methods for the analysis of collagen alignment in ligaments, Liu [117] developed directional filters in the Fourier domain for processing of images composed of linear patterns or linear segments oriented in different directions.

In his work, Liu Q.-Z. introduced a new method for linear pattern extraction and directional analysis. This method is based on Fourier spectrum analysis. For a square image, structures with a preferred orientation generate a periodic pattern at +90 degrees orientation in the Fourier transform of the image, compared to the direction of the objects in the input image.

Then the image is chopped into square pieces and their Fourier power spectra are computed. The later are analyzed in polar coordinates, and the power is measured for each angle using the spatial filters proposed in [117].

Based on his method, it is possible to capture linear patterns defined by their physical boundaries (edges) obtained over various scales. Also, it is possible to quantitatively analyze the directional distribution of patterns.

### 3.5.5 Classification - support vector machine (SVM)

Support Vector Machine (**SVM**) methods have been shown to be powerful tools for supervised classification [118]. **SVM** was first introduced by Boser, Guyon, and Vapnik at COLT-92 [119]. **SVM**s are a set of related supervised learning methods used for classification and regression. They belong to a family of generalized linear classifiers. In

another terms, **SVM** is a classification and regression prediction tool that uses machine learning theory to maximize predictive accuracy while automatically avoiding over-fit to the data.

When compared to other classes of classifiers, the main advantages of **SVM**s are that they are easy to use, often have good generalization performance, and the same algorithm solves a variety of problems with little tuning [120]. For example, K-nearest neighbors [121] are the simplest classifiers to implement; they are often effective but slow and requires lots of memory. On the other extreme, neural networks [122] are usually slow to train but very fast to run.

After evaluating many of the available classifiers, the decision to use **SVM**s was made due to the nature of this application. Aiming to build a robust package for classifying non-linear optical images originated from several applications, the simplicity, computational cost and capability of dealing effectively with multigroup classifications (and eventually non-linear decision boundaries) were factors heavily weighted towards the employment of **SVM**s.

In general words, **SVM**s start from the goal of separating the data with a hyperplane, and extend this to non-linear decision boundaries using the Kernel trick, which will be discussed below. The equation of a general hyperplane is

$$w'x + b = 0, \tag{3.3}$$

with $x$ being the point (a vector), $w$ the weights (also a vector). The hyperplane should separate the data, so that $w'x_k + b > 0$ for all the $x_k$ of one class, and $w'x_j + b < 0$ for all the $x_j$ of the other class. If the data are in fact separable in this way, there is probably more than one way to do it.

Among the possible hyperplanes, **SVM**s select the one where the distance of the hyperplane from the closest data points (the "margin") is as large as possible (Fig. 3.11).

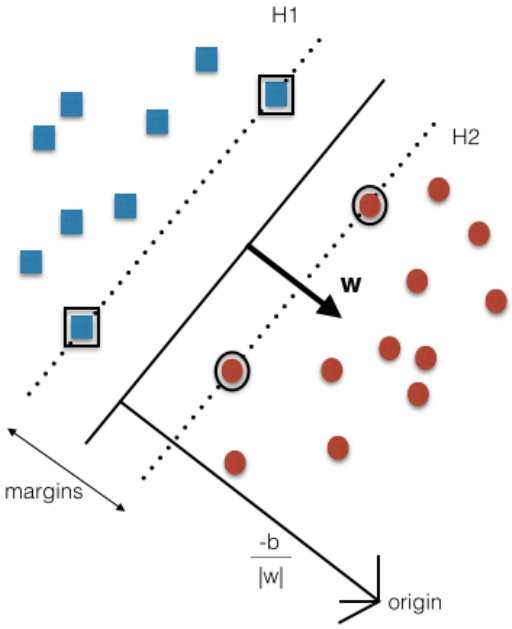


**Figure 3.11:** Linear separating hyperplanes for the separable case. The support vectors are circled. (© L.Mostaço-Guidolin, 2014)

Suppose the training data are good, in a sense that every possible test vector is within some radius $r$ of a training vector. Then, if the chosen hyperplane is at least $r$ from any training vector it will correctly separate all the test data. By making the hyperplane as far as possible from any data, $r$ is allowed to be correspondingly large. The desired hyperplane (that maximizes the margin) is also the bisector of the line between the closest points on the convex hulls of the two data sets.

In most real world problems, it is not likely to obtain a clear straight line dividing the data within the space, and a curved decision boundary could be possible. At times a hyperplane which clearly separates the data may not be desirable if the data has noise in it. In this type of classification, smooth boundary is more desirable than corners or loops around the outliers, even when it means to ignore few data points.

This can be handled in a different way: by introducing a term "slack variables". This allows a point to be at a small distance on the wrong side of the hyperplane without violating the constraint. Some extra calculations are introduced in order to penalize the large slacks; otherwise, we might end up having huge slack variables which allow any line to separate the data. More details about **SVM** can be found in the literature

[119, 120, 123, 124].

One aspect relevant to this study is what is called the *Kernel trick* [123,124]. If data is linear, a separating hyperplane may be used to divide the data. However it is often the case that the data is far from linear and the datasets are inseparable. To allow for this, kernels are used to non-linearly map the input data to a higher-dimensional space. The new mapping is then linearly separable. A very simple illustration of this is shown below in Fig. 3.12).

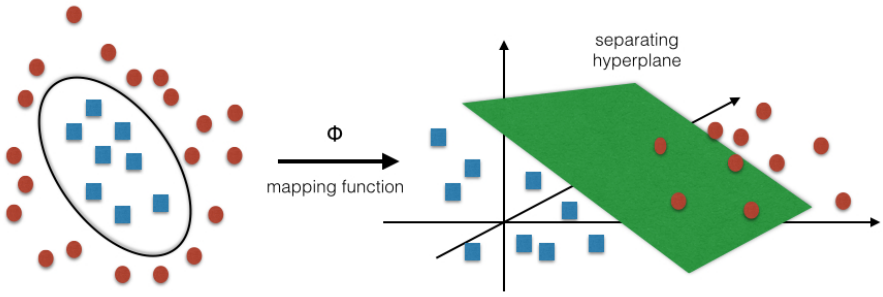


**Figure 3.12:** With an appropriate mapping function $\Phi$ we could map these data from the $\Re^2$ to the $\Re^n$ where a linear separation is possible. (© L.Mostaço-Guidolin, 2014)

The idea of the kernel function is to enable operations to be performed in the input space rather than the potentially high dimensional feature space. We want the function to perform mapping of the attributes of the input space to the feature space [125–128]. The kernel function plays a critical role in **SVM** and its performance. More information about the most commonly available kernels for **SVM**s can be found in the Appendix C.

A nonlinear classification based on **SVM** (ksvm in the R package kernlab) was used to classify **NLO** images in this thesis [129]. Using the built-in rbfdot kernel function in the package, a training set and a validation set were randomly created from the ensemble of **NLO** images.

A classification task usually involves training and testing data which consist of some data instances. Each instance in the training set contains target values and several attributes. The goal of **SVM** is to produce a model which predicts target value of data instances in the testing set which are given only the attributes.

For all analysis in which image classification was performed, the training set consisted of 2/3 of the whole data set, while the test set consisted of the 1/3 of the remaining

images. The **SVM** nonlinear classifier was trained and validated using k-fold cross-validation. For experiments involving two groups, k was equal to 3 and for experiments with 4 or more groups the used k was 5.

A grid search was performed aiming to best define the cost and gamma parameters. The grid search was done on k-fold cross-validation of the training set, and after reaching the maximum possibly accuracy, these parameters were then applied to classify the test set. The procedure of defining the cost and gamma parameters was independently repeated for each data set.

# Part I

# Nonlinear optical imaging for decoding atherosclerosis

# Chapter 4

# From the qualitative to quantitative: development of a novel optical index (OIPB) for plaque burden differentiation

Multimodal epi-**NLO** images were acquired from smooth/healthy luminal surface and atherosclerotic plaques of **WHHLMI** rabbits of different ages. Some examples of **NLO** images of arterial lumen are presented in Fig. 4.1.

Observing these images, they show several morphological differences among healthy and plaque regions. Composed by a more complex distribution of compounds than the healthy arterial lumen, an example of a region dominated by atherosclerotic plaque is shown in Fig. 4.1a.

Atherosclerotic plaque is a structure containing a fibrous cap that covers a necrotic core. The fibrous cap is composed largely of **SMC**, which produce collagen and small amounts of elastin. The necrotic core is filled mainly by lipid-filled macrophages and necrotic smooth muscle cells debris.

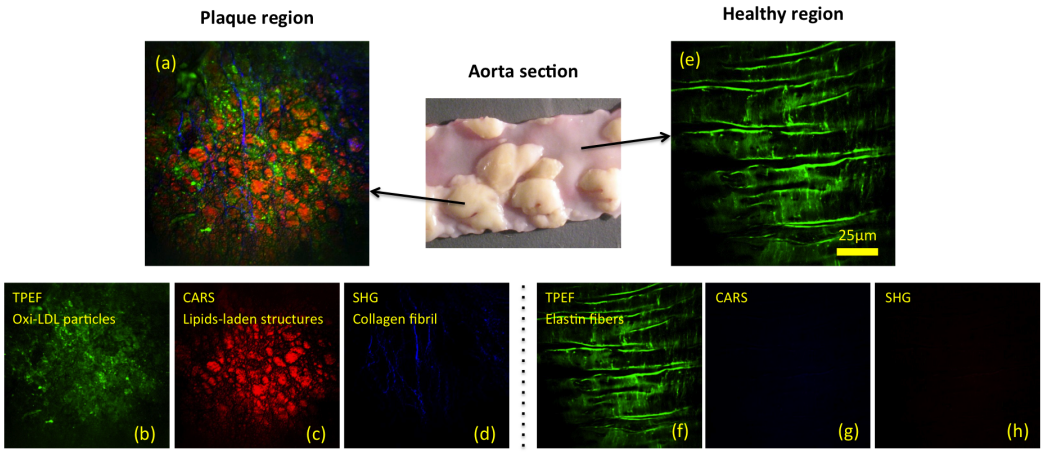


**Figure 4.1:** Images acquired with 20× air objective (0.75NA) lens from **WHHLMI** rabbit's aorta. **NLO** microscopy from (a) plaque region with (b) oxi-**LDL** particles color-coded in green (**TPEF**), (c) lipids in red (**CARS**), and collagen fibrils in blue (**SHG**). (e) Healthy region where (f) the elastin fibers are color-coded in green (**TPEF**), (g) lipids in red (**CARS**) and (h) collagen fibrils in blue (**SHG**). Both **SHG** and **CARS** signals were collected in the forward-direction while **TPEF** was collected in the backscattered (epi-) direction. *Reprinted with permission from Mostaço-Guidolin, Leila B., et al."Quantitative nonlinear optical assessment of atherosclerosis progression in rabbits.", Analytical Chemistry (2014) [17]. Copyright 2014 American Chemical Society.*

Figure 4.1b shows an image acquired from the **TPEF** modality, the signal of which can be associated mainly with the presence of oxidized low-density lipoprotein cholesterol (oxi-**LDL**) particles. Meanwhile, the **CARS** modality, when tuned to image the CH stretching vibrations, can visualize lipid-rich structures located at the necrotic core, as shown in Fig. 4.1c.

The fibrous cap can be identified by a network of collagen fibrils. **SHG** microscopy was used to probe collagen fibrils as presented in Fig. 4.1d. Since collagen fibrils give rise to a very strong second-harmonic signal, they can be imaged without using any exogenous dye thus not altering the proteins structure, as discussed in Chapter 2. In Fig. 4.1d it can be seen that the collagen molecules do not appear centre-symmetrical, and are organized in helicoidally oriented structures.

Healthy lumen (Fig. 4.1e) is mainly characterized by the presence of distinctively defined elastic fibers. Elastic fibers are composed of elastin, which generates strong **TPEF** signal (Fig. 4.1f). These biological tissues contain several chemical compounds which are detected through the **CARS** modality (Fig. 4.1g).

Although less frequently detected in healthy tissue than in regions dominated by plaque, it is also possible to observe sparse collagen fibrils in the **SHG** modality (Fig. 4.1h).

Besides the clear differences between images acquired from plaque and healthy arterial lumen, it is important to highlight morphological and biochemical alterations noted during the disease progression. Fig. 4.2a and b were acquired at a healthy region of the arterial lumen of a newborn and a 4 month-old rabbit, while Fig. 4.2C and D were acquired from healthy lumen of the 16 and 24 month-old rabbits, respectively. The images in Fig. 4.2e, f, g, and h were acquired from atherosclerotic plaques found in the 2, 4, 16, and 24 month-old rabbits, respectively.

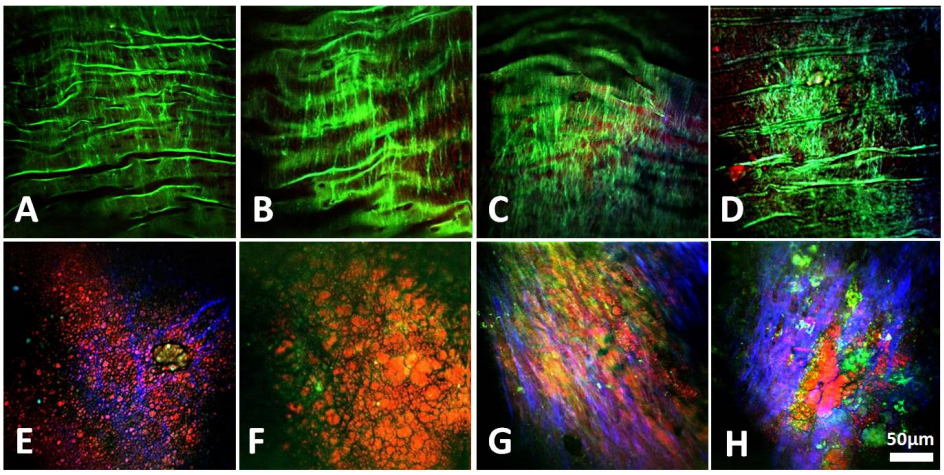


**Figure 4.2:** Representative multimodal epi-**NLO** images acquired from smooth/healthy luminal surface of the **WHHLMI** rabbit artery, that was (a) newborn, (b) 4 month-old, (c) 16 month-old, (d) 24 month-old, and atherosclerotic plaques found on the **WHHLMI** rabbit arteries that were (e) 2 month-old, (f) 4 month-old, (g) 16 months-old, and (H) 24 month-old. (20× air objective lens, 0.75 NA). *Adapted with permission from Mostaço-Guidolin, Leila B., et al."Differentiating atherosclerotic plaque burden in arterial tissues using femtosecond CARS-based multimodal nonlinear optical imaging", Biomedical Optical Express (2010) [18]. Copyright 2010 Optical Society of America.*

In representative **NLO** images of a healthy lumen, only the luminal elastic lamina is clearly visible from the **TPEF** signal. As the rabbit's age increases, small lipid-rich structures become evident (Fig. 4.2d), although with **TPEF** signal still prevailing.

On the other hand, representative **NLO** images from the surface of an advanced arterial plaque, show abundant lipid-rich structures (**CARS** in red), collagen fibrils (**SHG** in blue) along with strongly fluorescent (**TPEF** in green) macromolecules, as

shown, for example in Fig. 4.2h.

The diminishing elastin content at the region of plaque is compensated for by an increasing number of other fluorescent macromolecules detected by **TPEF**.

The enhanced **SHG** intensity arising from collagen fibrils and the **CARS** intensity arising from lipid-rich structures from regions of plaque are consistent with known plaque pathology.

Collagen fibril scoring was previously developed using parameters extracted from **SHG** images, according to Strupler *et al.* [130]. In that work the authors used three phenomenological scores - $D$, $S$, and $SF$ - to quantify the distribution of collagen fibrils in unlabeled fibrotic murine kidney tissue sections.

This study was based on **SHG** images, where $D$ (density) is the volume density of pixels exhibiting a significant **SHG** signal; $S$ (signal) is the average value of the **SHG** signal in a corrected **SHG** image and $SF$ (signal in fibers) is the ratio of the other two scores: $SF = S/D$, representing average **SHG** signal intensity in regions exhibiting significant **SHG** signals.

This method was adequate in scoring collagen from sectioned kidney tissue, but may prove challenging in classifying complex biological structures such as atherosclerotic lesions, especially when using multi-dimensional information (collagen, elastin, and lipids).

In order to evaluate the potential of the methods proposed by Strupler and colleagues, we followed their approach to calculate $SF$ scores from individual and co-registered **SHG**, **TPEF** and **CARS** images of the same sample.

Parameters $D$ and $S$ were first calculated for all **SHG**, **TPEF** and **CARS** images. Note that while Strupler *et al.*defined $S/D$ as a signal in fibers score ($SF$), in this study we were using a more generic term, significant signal score ($SS$), since not all imaged biomolecules in our study have fibrous structures. A significant signal score ($SS$) was calculated for each image using the equation $SS = S/D$.

Each individual image (**SHG**, **TPEF** and **CARS**) was first corrected for **PMT** dark signal counts and for the **PMT** amplification level used in different modalities by normalizing the whole image to a pre-determined **PMT** amplification curve.

Three SS scores ($SS_{SHG}, SS_{CARS}$ and $SS_{TPEF}$) were calculated using the corrected **SHG**, **TPEF** and **CARS** images collected over the same sampling location.

In order to better illustrate the change in $SS$ scores with respect to plaque progression represented by the age of the rabbit, the average $SS$ scores obtained from the images of four rabbits are presented in Fig. 4.3. Data from animals aged 4, 16, 18, and 24 months is presented as a representation of $SS$ score behavior.

The average $SS$ scores and their standard deviations were obtained by averaging over all $SS$ scores extracted from all of the measurements performed in all samples, including healthy and atherosclerotic luminal surfaces, along the artery of the same animal. A total of 820 different points were measured, with an average of 55 measured points per animal.

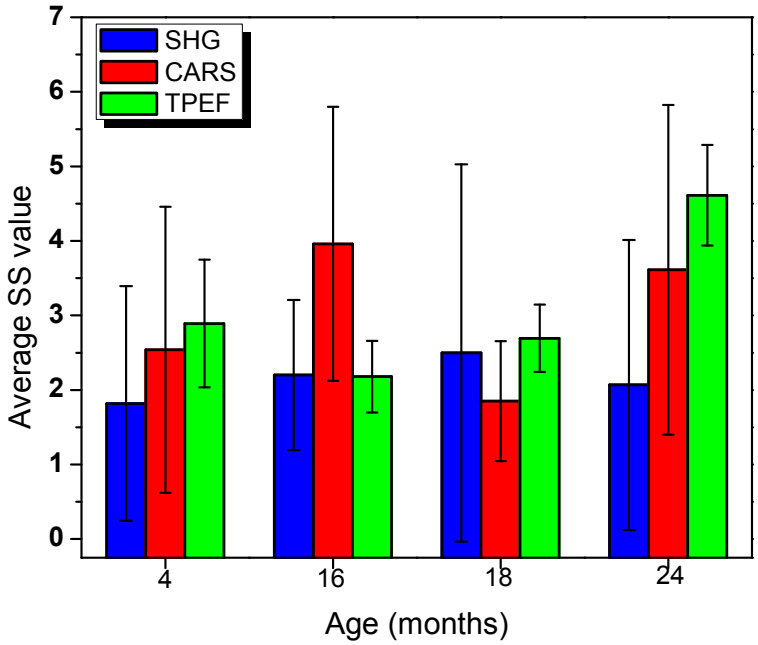


**Figure 4.3:** Comparison of the $SS$ scores extracted from **SHG**, **CARS** and **TPEF** images acquired from the arterial lumen of four **WHHLMI** rabbits: 4 month-old, 16 month-old, 18 month-old and 24 month-old. *Reproduced with permission from Mostaço-Guidolin, Leila B., et al."Differentiating atherosclerotic plaque burden in arterial tissues using femtosecond CARS-based multimodal nonlinear optical imaging", Biomedical Optical Express (2010) [18]. Copyright 2010 Optical Society of America.*

According to the data presented in Fig. 4.3, it is clear that it is not possible to differentiate atherosclerotic plaque burden using SS scores from any of three modalities.

Generally, atherosclerotic progression should lead to an increase in **SHG** and **CARS**

signals as both collagen and lipids content increase; however, $SS_{SHG}$ and $SS_{CARS}$ scores are not increasing proportionally to plaque development.

Considering the score sets obtained for each animal, we can conclude that these values are not statistically different according to the Mann–Whitney test. Therefore, $SS$ scores alone are not good indicator to differentiate plaque burden.

## 4.1 Disease progression: plaque burden *versus* animal age

Although $SS$ scores are well correlated in scoring collagen in sectioned fibrotic kidney tissue [130], but they are not reliable indicators for distinguishing atherosclerotic plaques.

In order to address the complexity and the dynamic nature of atherosclerotic disease progression, we developed a new parameter that can better track plaque burden in the vessel using biochemical data collected through combined elastin, collagen and lipid imaging. We named this parameter Optical Index for Plaque Burden, or **OIPB**.

Considering the images presented in Fig. 4.4, which are organized based on the level of plaque burden, it is possible to define some patterns of changes in all three **NLO** signal modalities while fig. 4.4A-C show examples of healthy arterial lumen, Fig. 4.4D shows an early atherosclerotic lesion found in a young rabbit, and in Fig. 4.4E we can see some collagen fibers formation (shown in blue) within an atherosclerotic plaque.

Finally, Fig. 4.4F is an atherosclerotic plaque with higher lipid (shown in red) content; Fig. 4.4G is an atherosclerotic plaque containing a high density of collagen fibers and lipids, and finally Fig. 4.4H is a very advanced lesion.

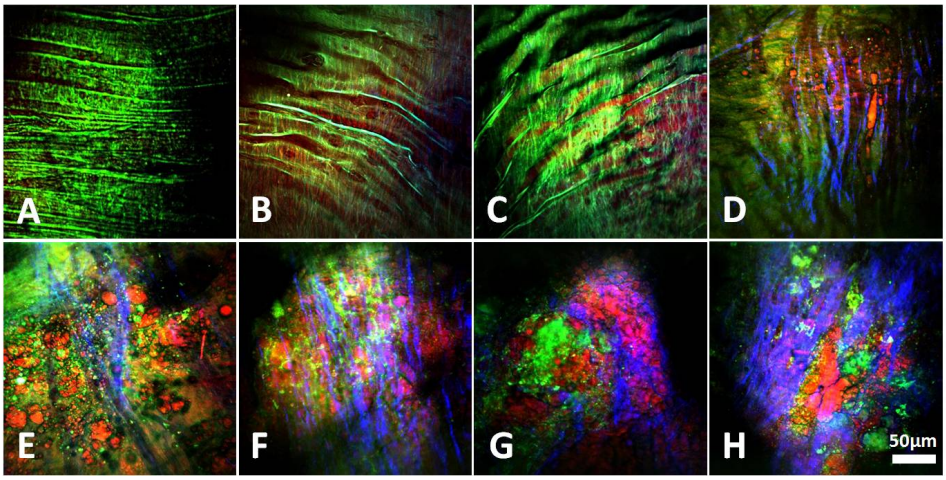


**Figure 4.4:** Representative multi-modal epi-**NLO** images acquired with 20× air objective lens, 0.75 NA, from the luminal surface of WHHLMI rabbit arteries, with (A)-(C) healthy lumen; (D) early atherosclerotic plaque found in young rabbit; (E) atherosclerotic plaque (with dense collagen fibers shown in blue); (F) atherosclerotic plaque with higher lipid content shown in red; (G) atherosclerotic plaque containing collagen fibers and lipids, and (H) very advanced plaque. *Adapted with permission from Mostaço-Guidolin, Leila B., et al."Differentiating atherosclerotic plaque burden in arterial tissues using femtosecond CARS-based multimodal nonlinear optical imaging", Biomedical Optical Express (2010) [18]. Copyright 2010 Optical Society.*

Values of $SS_{SHG}$, $SS_{TPEF}$ and $SS_{CARS}$ for each image shown in Fig. 4.4 were calculated and then presented in Fig. 4.5, where the $SS_{SHG}$ and $SS_{CARS}$ scores are associated with collagen and lipids (both are related to plaque regions), and $SS_{TPEF}$ scores can be associated with elastin in healthy tissue or with other fluorescent macromolecules in the region of plaque.

From Fig. 4.5, we clearly observe a pattern for each of the $SS$ scores, which can be summarized as follows. The healthier the tissue is, the lower are the $SS_{SHG}$ and the $SS_{CARS}$, but the higher is the $SS_{TPEF}$. The opposite is true if the tissue has an increased plaque burden. In addition, we also observe some correlation in the value differences between the three $SS$ scores based on the health condition of the tissue. For instance, the healthier the tissue is, the greater is the difference between the $SS_{SHG}$ and $SS_{TPEF}$, with $SS_{TPEF}$ being higher than $SS_{SHG}$; and also the greater is the difference between $SS_{CARS}$ and $SS_{TPEF}$, with $SS_{TPEF}$ higher than $SS_{CARS}$.

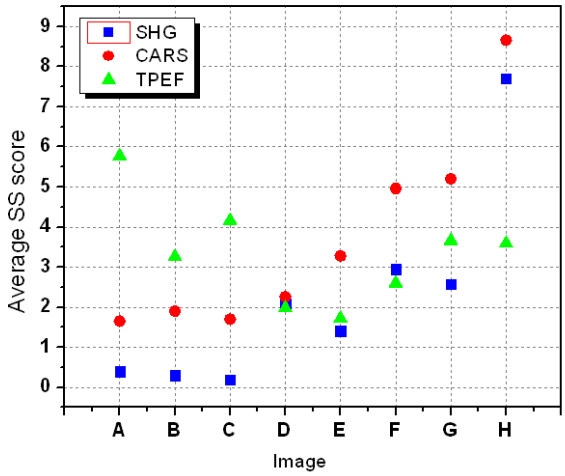


**Figure 4.5:** *SS* scores extracted from **SHG** (blue squares), **CARS** (red circles) and **TPEF** (green triangles) images acquired from the arterial lumen of **WHHLMI** rabbits. Images A-H correspond to those shown in Fig. 4.4. *Reproduced with permission from Mostaço-Guidolin, Leila B., et al."Differentiating atherosclerotic plaque burden in arterial tissues using femtosecond CARS-based multimodal nonlinear optical imaging", Biomedical Optical Express (2010) [18]. Copyright 2010 Optical Society.*

Based on these observations, a new plaque burden index (**OIPB**) is proposed and is defined as follows:

$$\begin{aligned} OIPB = \; & SS_{SHG} + SS_{CARS} \; + \\ & d(SS_{SHG}, SS_{TPEF}) \; + \\ & d(SS_{CARS}, SS_{TPEF}) \; + \\ & d(SS_{CARS}, SS_{SHG}), \end{aligned} \tag{4.1}$$

where the terms $d(SS_x, SS_y)$ are the differences between the two $SS$ scores (**SHG**, **CARS** and **TPEF**), $d(SS_x, SS_y) = SS_x - SS_y$. Note that $SS_{TPEF}$ score alone was not included in the calculation of **OIPB** values because provides no additional contrast in discriminating between the atherosclerosis lesions from healthy vessel wall. The term $d(SS_{CARS}, SS_{SHG})$ was added in the calculation for its value in discriminating between a lipid-rich Type-IV atheroma and a Type-V fibrous atheroma. For instance, $d(SS_{CARS}, SS_{SHG})$ shows be larger for Type-IV atheroma than for Type-V fibrous atheroma.

**OIPB** values for images shown in Fig. 4.4A-H were calculated and are illustrated in Fig. 4.6, where a clear correlation between **OIPB** values and image features is evident. Fig. 4.6 also indicates that **OIPB** is a better indicator for atherosclerotic plaque burden.

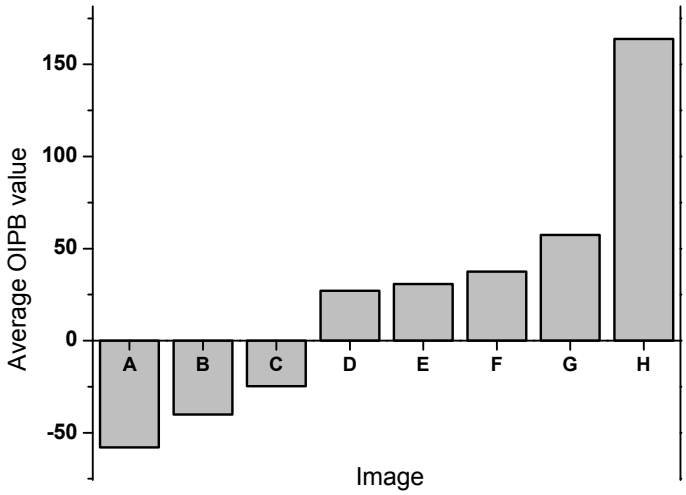


**Figure 4.6:** **OIPB** values of all images shown in Fig. 4.4. **OIPB** is a better discriminatory indicator in differentiating plaque burden than SS scores. *Reproduced with permission from Mostaço-Guidolin, Leila B., et al."Differentiating atherosclerotic plaque burden in arterial tissues using femtosecond CARS-based multimodal nonlinear optical imaging", Biomedical Optical Express (2010) [18]. Copyright 2010 Optical Society.*

Based on this result, the correlation between **OIPB** and plaque burden represented by rabbit's age was investigated. Examples of **OIPB** values and images are illustrated in Fig. 4.7. Each image in Fig. 4.7 is shown with rabbit's age and corresponding **OIPB** value (highlighted in yellow). Fig. 4.7a-e show relatively healthy lumens with low **OIPB** values, while Fig. 4.7f-j show representative images of atherosclerotic lumens captured with increasing ages that have corresponding higher **OIPB**. Fig. 4.7f shows an image of a plaque from a 4-month-old rabbit artery which has an **OIPB** of 17.3 whereas Fig. 4.7j, shows an image of a 24-month-old rabbit artery which has an **OIPB** value of 69.3.

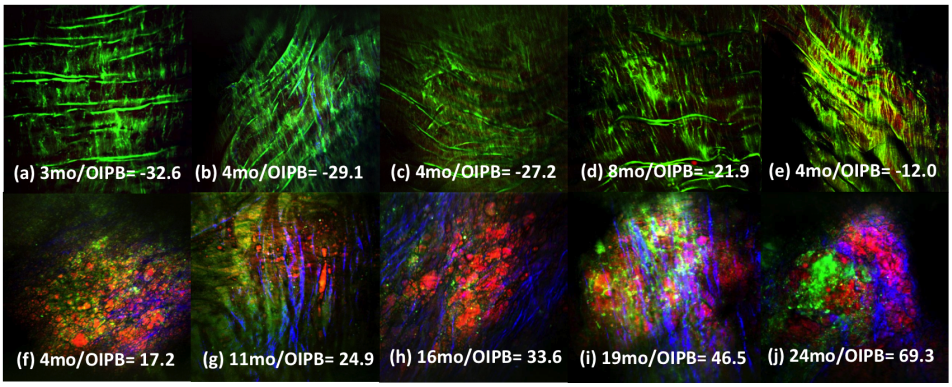


**Figure 4.7:** Representative epi-**NLO** images obtained from the luminal surface of healthy rabbits aorta (a)-(e), and obtained from the luminal surface of atherosclerotic plaques (f)-(j). Each image is labeled with the age of the rabbit and its corresponding **OIPB** calculated using Eq. 4.1. Images were collected using 20x air objective lens. *Reprinted with permission from Mostaço-Guidolin, Leila B., et al."Quantitative nonlinear optical assessment of atherosclerosis progression in rabbits.", Analytical Chemistry (2014) [17]. Copyright 2014 American Chemical Society.*

The average **OIPB** values obtained from images of healthy lumen surfaces ($OIPB_{healthy}$) and atherosclerotic ($OIPB_{athero}$) locations are plotted against rabbit's age in Fig. 4.8.

Each point shown corresponds to the averaged measurements taken from either plaque or healthy regions, averaged, representing each individual rabbit. In the majority of these 21 rabbits, the values of $OIPB_{athero}$ are significantly higher than those of $OIPB_{healthy}$. The $OIPB_{healthy}$ values are distributed between -73 and 5, while most of the $OIPB_{athero}$ values range from 15 to 70. The high level of $OIPB_{athero}$ values are attributed to the higher level of collagen re-modeling and higher-density of lipid deposition in plaques, thus translating into the higher $SS_{SHG}$ and $SS_{CARS}$ terms.

Additionally, an interesting trend can be noticed when looking at data presented in Fig. 4.8. The current findings indicate that atherosclerosis in **WHHLMI** rabbits is characterized by the evolution of progressive intimal lesions, including fatty streaks, raised foam cell lesions, plaques (atheromas) as well as by medial lipid deposition.

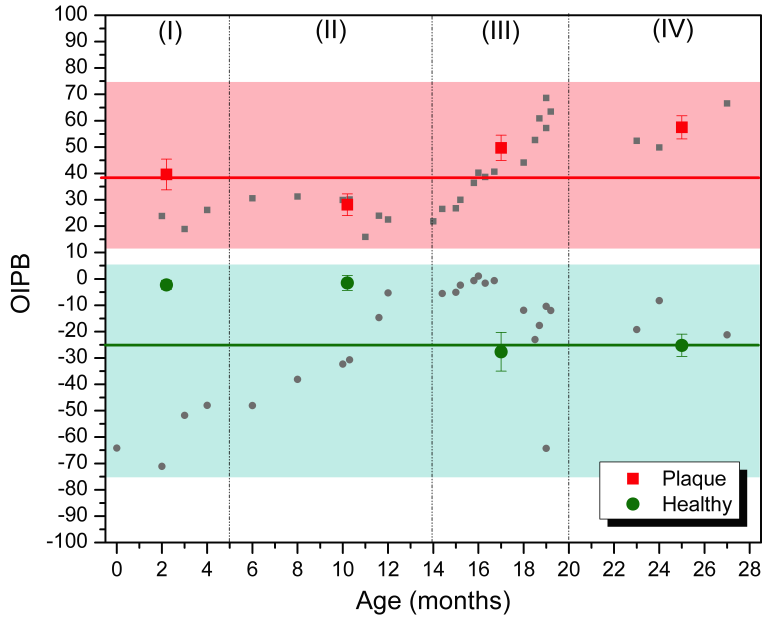


**Figure 4.8:** Mean OIPB values for images acquired from plaque (large squares) and healthy (large circles) regions of each rabbit, plotted against rabbit's age. The large symbols represent the mean value of each region. As the rabbit's age increases, regions dominated by plaque show higher **OIPB** values, suggesting that the lesions are advancing with age. The solid line is the mean value, considering all animals, and the two colored regions are the standard deviation around the mean. *Reprinted with permission from Mostaço-Guidolin, Leila B., et al."Quantitative nonlinear optical assessment of atherosclerosis progression in rabbits.", Analytical Chemistry (2014) [17]. Copyright 2014 American Chemical Society.*

Disruptions of healthy regions seem to increase until approximately half of the animal's life cycle (at around 14-15 month-old), as shown in the green areas of "healthy" **OIPB** age groups I-II presented in Fig. 4.8. At the same time, the plaque's composition and structure until the age of 14-15 months remains quite stable. At a later age its development becomes quite aggressive (age group III, red area – Fig. 4.8), reaching a plateau at the rabbit's age of approximately 20 months (age group IV).

According to the **OIPB** values calculated for healthy (green) regions of lumen found in older animals (age groups III and IV), it is interesting to notice that they also seem to reach a plateau in their disruption around the same age ( 20 months). This trend could be useful when trying to test and perform therapies aiming at the recovery and/or regression of atherosclerotic plaque. Our results suggest that there is a critical threshold regarding the disease development and progression.

In Fig. 4.9, the mean **OIPB** values from all rabbits are presented as a function of age.

In this plot each rabbit was represented by a mean **OIPB** value, obtained by averaging data collected from all imaged healthy and atherosclerotic locations.

As the disease progresses, the fraction of luminal area covered by lesions increases; in this way, a higher number of measurements taken from older rabbits tend to present features associated with plaque when compared to younger animals. All points where the images were taken were selected randomly in specific anatomical regions. Since larger portion of the lumen is covered by plaques at an old age, the number of images acquired from points that represent plaque regions also increases with age.

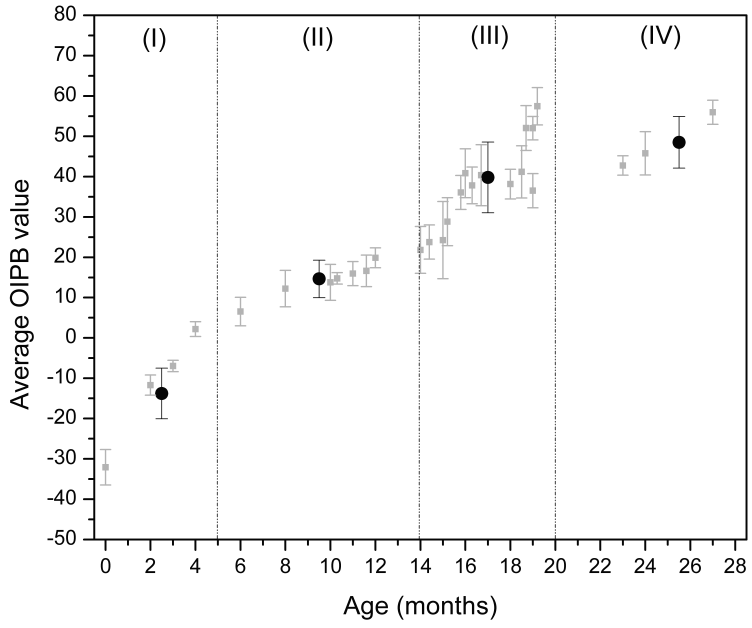


**Figure 4.9:** Mean **OIPB** values for all rabbits, considering both plaque and healthy regions. The Greek numbers on top of each graph are associated with age groups presenting similar histopathological patterns (Buja *et al.* [19]). *Reprinted with permission from Mostaço-Guidolin, Leila B., et al."Quantitative nonlinear optical assessment of atherosclerosis progression in rabbits.", Analytical Chemistry (2014) [17]. Copyright 2014 American Chemical Society.*

The index shows a clear correlation with age. Since plaque burden increases with the age of the rabbit this result implies that the **OIPB** value is indicative of severity of the atherosclerotic lesions, or plaque burden. The regions (I), (II), (III), and (IV) indicated in Fig. 4.8 and Fig. 4.9 represent age groups which present similar histopathological patterns in the arterial wall. Region (I) contains data from rabbits aged from 0 to 5 months; region (II) presents data collected from 5.5 to 14 months old animals; region

(III) and (IV) show data acquired from the rabbits within the 14.5 to 20 months and 20.5 to 27 months aged groups, respectively. This categorization was also previously reported by Buja *et al.* [19].

Additionally, Kolodgie *et al.* [131] has published an extensive work showing the progression and the varying degrees of atherosclerotic plaques, using **WHHLMI** rabbits as a model. One of the conclusions reached by the authors is that rabbits within the age group ranging from approximately 3 to 5 month-old presented mild lesions along the aorta. When the age increased from 6 to 9 month-old, these lesions became moderated and severe plaque accumulation was observed in animals older than 12-14 month-old.

Similar conclusion can be reached, as shown in Fig. 4.9, the difference between the mean value (black dot shown in each region) is the highest when comparing the **OIPB** values of rabbits from regions (II) and (III). When comparing regions (III) and (IV) the values are statistically comparable, suggesting that after a certain age (between 12 and 16 month-old) the disease reaches its most severe stage.

## 4.2 Indexing plaque burden at critical locations along the aorta

During the course of atherosclerosis progression, certain locations along the aorta are more prone to plaque development than others [132]. These locations include transition zones such as bends, arches and bifurcations. At these locations the rate and pattern of blood flow are altered thus affecting local hemodynamics [133, 134].

Attempts have been made to assess the role of hemodynamic factors in atherosclerosis by correlating the distribution of intimal lesions, usually in excised collapsed arteries, with presumed changes in blood flow conditions or with flow patterns visualized in idealized glass or plastic models. Elevations or variations in flow velocity and shear stress [134, 135], flow separation [136], and turbulence [137–139] have each been proposed as hemodynamic potentiating of lesion formation.

In this context, since we have demonstrated that **OIPB** was a good indicator for

assessing plaque burden in a longitudinal study, it was interesting to test if **OIPB** was also capable of accurate detection of the higher plaque burden at certain critical locations along the aorta. **NLO** images acquired at four pre-defined points per segment (i.e., arterial arch, thoracic artery, abdominal artery and external iliac artery) were thus analyzed and then compared with immunohistological data based upon **ICAM-1** fluorescence imaging. The approximate location of each point is shown in Fig. 4.10.

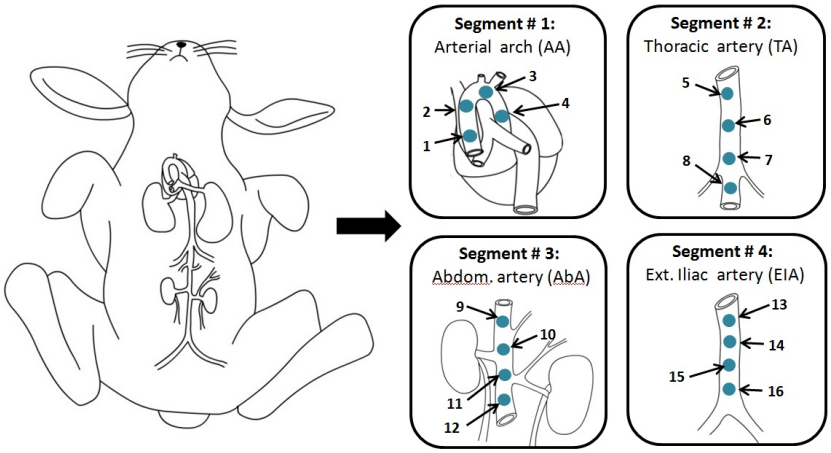


**Figure 4.10:** Points along the aorta which were used as a reference. These points represent possbile interesting locations to be studied with respect to plaque burden accumulation along the vessel. *Reprinted with permission from Mostaço-Guidolin, Leila B., et al."Quantitative nonlinear optical assessment of atherosclerosis progression in rabbits.", Analytical Chemistry (2014) [17]. Copyright 2014 American Chemical Society.*

The average **OIPB** value for each point shown in Fig. 4.10, calculated by considering both healthy and plaque regions, is presented in Fig. 4.11a (black trace, with squared points). Note that locations 3, 8 and 10 are characterized by the highest **OIPB** values, hence the highest plaque burden along the entire aorta tree. When compared with the **OIPB** data, immunohistological data (blue trace) based on **ICAM-1** fluorescence intensity showed marked similarity. In addition, Fig. 4.11b and Fig. 4.11c illustrate representative **ICAM-1** fluorescence images and white-light video images of the 4 pre-defined arterial segments.

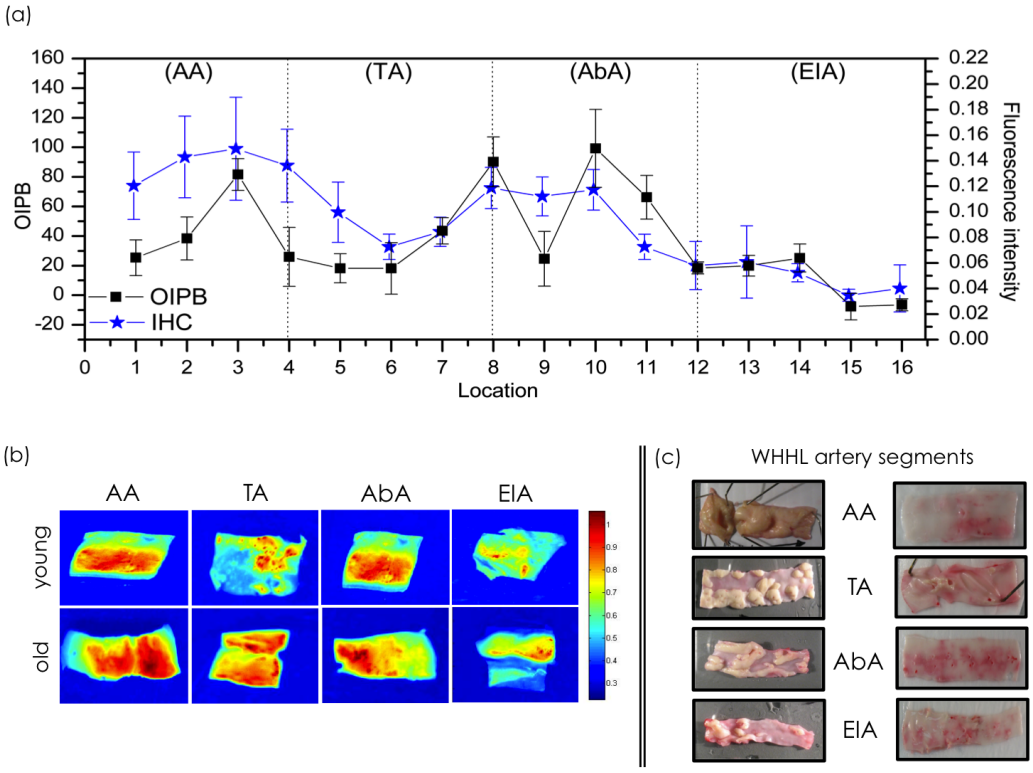


**Figure 4.11:** a) **OIPB** values for each point along the aorta; (b) Average fluorescence intensity values related to **ICAM-1** distribution in arterial samples from **WHHLMI** rabbits. In both cases the highest values can be associated to more severe plaque accumulation. Those values were obtained mainly at branch and vessel bifurcations, confirming the capability of this index to also track/highlight the plaque burden development along the aorta. **AA**: aortic arch; **TA**: thoracic artery; **AbA**: abdominal aorta; **EIA**: external iliac aorta. *Reprinted with permission from Mostaço-Guidolin, Leila B., et al."Quantitative nonlinear optical assessment of atherosclerosis progression in rabbits.", Analytical Chemistry (2014) [17]. Copyright 2014 American Chemical Society.*

Matching results in Fig. 4.11a with location maps in Fig. 4.10, it becomes clear that the 3 locations with the highest **OIPB** values and **ICAM-1** fluorescence intensities correspond to the aortic arch, and regions close to the two kidneys' artery branches, respectively.

In the aortic arch, the pattern of blood flow is more complex than in the other regions along the descending abdominal aorta, with constant helical and extensive reversal flow resulting from the curvature of the arch and the strong pulsatility of flow [140–142]. As a result, this turbulence of blood flow and change in arterial wall shear stress leads to elevated probability of plaque development within the vessel [141]. Similarly, re-

gions which are close to kidneys' artery branches also experience non-laminar blood flow due to arterial bifurcation. This too, significantly enhances the early development of atherosclerosis lesions [143].

Although similar patterns were observed, the **ICAM-1** data does look slightly different from the **OIPB** data. From Fig. 4.11a one can see that the drop and rise in **OIPB** values around these critical locations are much steeper than those presented in the **ICAM-1** fluorescence data. This can be explained by the different sampling size of these two very different optical techniques. While each **NLO** imaged area was 200x200 $\mu m^2$ in size (with 20x objective lens), **ICAM-1** fluorescence was typically evaluated over an area of 1x1$cm^2$.

The smaller sampling size in **NLOM** gives a more localized snapshot, whereas the **ICAM-1** data present a picture with information averaged over a larger area. This characteristic of **NLOM** makes it a more sensitive tool in detecting local changes thus generating a sharper contrast between different locations. Nonetheless, regions with a greater tendency to be affected by atherosclerotic lesions were successfully tracked by both the **OIPB** and the **ICAM-1**.

The relation between vessel's wall shear stress and the development and progression of atherosclerosis has been well established [143, 144, 144, 145]. Low and oscillating wall shear stress seems to favor the development of atherosclerosis as determined by the inverse relation between the wall shear stress and arterial wall thickness. Wall shear stress also seems to depend on age, blood pressure, and body mass index. The value of wall shear stress is subject-specific and vessel-specific. Wall shear stress varies along the same vessel and around the vessel's circumference.

Another interesting observation is that as the rabbit's age increases, all four studied aorta regions (**AA**, **TA**, **AbA**, **EIA**) show increasing **OIPB** values, suggesting that the lesions are also advancing with age and are successfully tracked by the **OIPB**.

# Chapter 5

# Looking inside the plaque: texture analysis to extract biochemical and morphological details

Visual investigation of the **NLO** images not only shows the formation of collagen fibrils and lipid-rich structures on the lumen surface of progressive plaques, but also permits the differentiation of those structures, based on their texture. For example, an image acquired from an early lesion shows only thin sparse collagen fibrils (Fig. 5.1) but in advanced lesions the collagen fibrils are thicker and more directional.

Another change is observed in the lipid accumulation. It starts as droplets and then becomes bigger (as shown in Fig. 5.1) and is more homogeneously distributed in the tissue.

**TPEF** images can be useful to track changes that occur in healthy tissue (Fig. 5.1). Elastin fibers can be imaged and the observed changes can be quantified by applying several methodologies. **TPEF** images from plaque regions show the accumulation of unkown fluorescent particles.

All results presented in this chapter are related to the analysis of **NLO** images acquired only at plaque regions. The analysis of changes observed in healthy tissue are presented in Chapter 9.

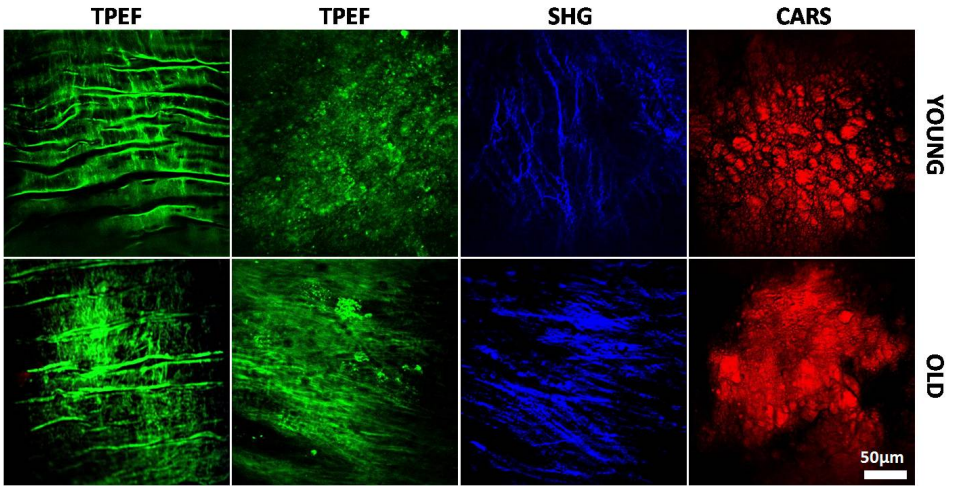


**Figure 5.1:** Images from **NLO** channels using a 20x air lens. Each **NLO** channel is shown separately (at a focal position around $25-30\mu m$ below the sample surface for the old specimen, and around $10-20\mu m$ below the sample surface for the young specimen). Blue: **SHG** (collagen fibrils); red: **CARS** (lipids); green: **TPEF** (elastin from healthy tissue and fluorescent particles from plaques). Images for the early plaque and healthy region were acquired from a sample harvested from a 4 month-old **WHHLMI** rabbit and images of the developed plaque were acquired from a sample collected from an 18 month-old **WHHLMI** rabbit. *Adapted with permission from Mostaço-Guidolin, Leila B., et al."Evaluation of texture parameters for the quantitative description of multimodal nonlinear optical images from atherosclerotic rabbit arteries." Physics in Medicine and Biology (2011) [16]. Copyright 2011 IOP Publishing Ltd*

Based on the observed differences in tissue morphology, we believe that image texture analysis can provide additional objective measures to evaluate plaque development.

## 5.1 Evaluation of plaque depth

Atherosclerotic lesions develop progressively through a series of events leading to the development of mature lesions named atheromatous plaques. Figure 5.2A is a sketch representing a mature lesion consisting of a fibrous cap (I), (II) a necrotic core, and (III) the media layer. The fibrous cap is composed largely of smooth muscle cells (**SMC**), which produce collagen, small amounts of elastin, and glycosaminogycans; the necrotic core is composed mainly of lipid-filled macrophages and necrotic smooth muscle cells debris, and finally, the media layer consists mainly of smooth muscle cells.

Figure 5.2B compares a sequence of **NLO** images acquired from arterial samples, with the lumen exposed to the incoming probe beam. An image is obtained by raster

scanning of the focused laser beam across a plane located at a particular depth within the sample. By changing the focal plane, images were acquired at different depths within the artery. The first column of images is an example of the optical sectioning obtained by recording the **TPEF**, **SHG** and **CARS** intensities at various depths within the aorta of a 4 month-old rabbit (labeled young). This set of images represents an early lesion. The second column of images shows the optical sectioning of an older plaque (labeled old), a specimen obtained from a 24 month-old rabbit.

These optical sections (generated by a combination of **TPEF**, **SHG**, and **CARS** images) resolve many of the classic histological features associated with plaque development and provide the depth dependence of these features.

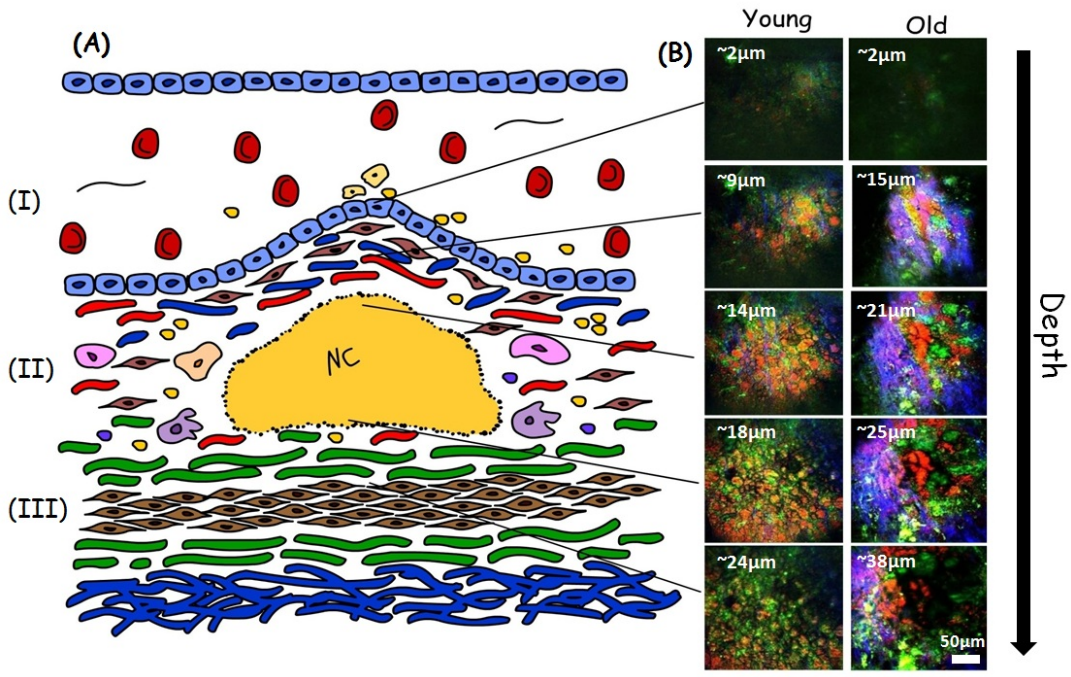


**Figure 5.2:** (A) The atherosclerotic plaque is composed of three major layers: (I) fibrous cap, consisting mainly of smooth muscle cells (**SMC**), which produce collagen, small amounts of elastin, and glycosaminogycans; (II) necrotic core (NC) consisting of lipid-filled macrophages, necrotic smooth muscle and cellular debris; and (III) the media layer, consisting of smooth muscle cells (B) Examples of multimodal **NLO** images acquired with a 20x air lens at various depths within atheromatous plaques. The first image set shows plaque from a 4 month-old rabbit, while the second image set is from the aorta harvested from a 24 month-old rabbit. Blue: **SHG** (collagen fibrils). Red: **CARS** (lipids). Green: **TPEF** (fluorescent macromolecules). *Adapted with permission from Mostaço-Guidolin, Leila B., et al."Evaluation of texture parameters for the quantitative description of multimodal nonlinear optical images from atherosclerotic rabbit arteries." Physics in Medicine and Biology (2011) [16]. Copyright 2011 IOP Publishing Ltd*

Aiming to track changes that occur during plaque development inside of the vascular wall, image texture analysis was performed. Information regarding the morphological alterations could be quantitatively obtained for images acquired by using all three modalities.

Comparing values of the mean gray level and its standard deviation, it is possible to verify significant changes occurring to the **SHG** signal as deeper regions of the samples are probed, as shown in Fig. 5.3A and Fig. 5.3B. In these figures, the reading on x-axis represents the position of the imaging focal point in relation to the lumen surface.

In a healthy artery, the collagen fibers are mostly located within the tunica media, delimited by an internal elastic membrane. In contrast, in diseased arteries, common among the older specimens, collagen fibers are found to extend beyond an interrupted internal elastic layer. Plaques observed in old animals present a mean gray level value around 4 times more intense than the ones associated with plaques in younger animals.

This difference reflects the well-known feature that fibrous caps of plaques from old animals are denser than those found in young animals. These histological characteristics of atherosclerosis correlate well with our experimental measurements where higher **SHG** intensities are observed at depths between $15 - 30\mu m$ in the samples coming from the older specimens, whereas the maximum **SHG** intensities are observed at depths of around $5\mu m$ in samples harvested from younger animals.

Observing the variation of the **CARS** signal, its maximum intensity in older animals appeared approximately $5 - 7\mu m$ deeper than observed in young animals. Consistent with histology, the **CARS** signal, which highlights lipids, shows that lipid accumulation occurs in the intermediate portion of the plaque. For example, in the case of young animals, the lipid pool appears approximately $5\mu m$ deeper than collagen fibrils signaled by the **SHG** channel and can be explained with fibrous cap formation over the surface of lipid pools.

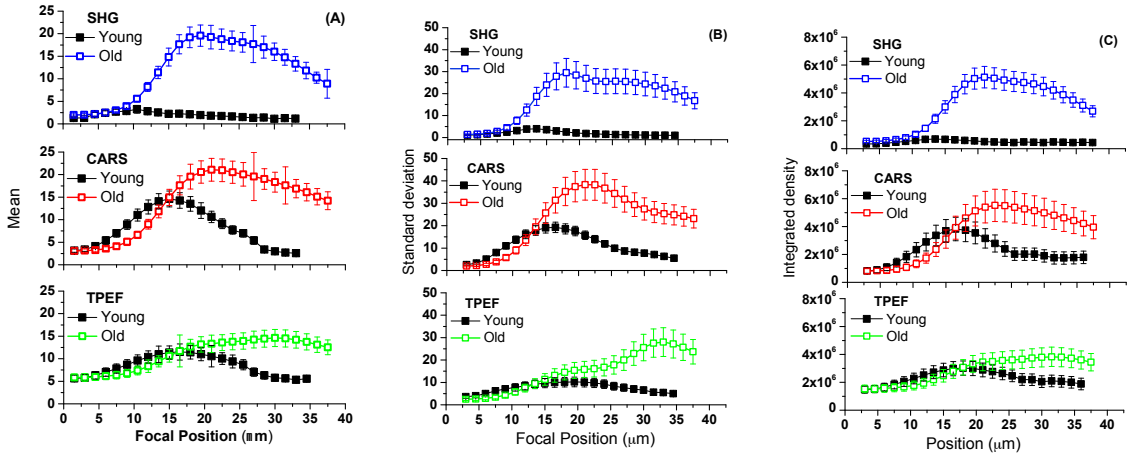


**Figure 5.3:** First order statistics: (A) mean, (B) standard deviation and (C) integrated density. Features were individually calculated for each **NLO** imaging modality (**TPEF**, **CARS**, and **SHG**) and analyzed as a function of imaging depth within the aorta wall. In most cases, distinct differences were observed in the first order statistics between young and old animals and with imaging depth. The analysis was done starting from the sample surface (i.e., the lumen) to the depths of almost $40\mu m$. The intensity recorded for each of the **NLO** channels depends on both the depth and specimen age. The old group includes specimens that were 18 and 24 month-old while the young group contains specimens from 4 and 10 month-old animals. *Adapted with permission from Mostaço-Guidolin, Leila B., et al."Evaluation of texture parameters for the quantitative description of multimodal nonlinear optical images from atherosclerotic rabbit arteries." Physics in Medicine and Biology (2011) [16]. Copyright 2011 IOP Publishing Ltd*

Proliferation of collagen fibrils and lipid accumulation play key roles in the development and vulnerability of atherosclerotic plaques where a thin fibrous cap coupled with a large lipid filled core represent a high risk lesion. Old animals present a more complex necrotic core, due to the extended lipid pools and higher concentration of both collagen fibrils and lipid-rich cells in the same region, near the arterial lumen.

In fact, the strongest **CARS** and **SHG** signals are observed to be almost overlapped in the plaques from older animals. On the other hand, the maximum **CARS** and **SHG** signals are observed at different depths for the less fully developed plaques in the young specimens.

A significant **TPEF** signal starts at depths of about $10\mu m$ and extends throughout the rest of the optical section of the plaque. The origin of the **TPEF** signal could be either from elastin fibers or several types of macromolecules associated with plaque formation. It is not trivial to establish what generates the **TPEF** signal without histological

correlation.

We observe fluorescent objects within fibrous caps and lipid cores whose origin has not been determined yet. The **TPEF** signal that we observed clustering in small groups among the collagen fibers , has been identified as coming from the foam cells (macrophages with intracellular lipid droplets) [35, 38, 146]. As the lipid core is mainly necrotic cells, and the fluorescent objects appear as different sizes, the corresponding **TPEF** signal could be also related to extracellular lipid droplets.

A study conducted by Blankenhorn *et al.* has reported a strong, green, one-photon autofluorescence generated from the lipid core of atherosclerotic plaques [147]. This has been associated with carotenoids, which are known to be lipophilic. Another study found one-photon autofluorescence from various biochemical components, which are known to be present in atherosclerotic plaques (e.g., oxidized lipoproteins and cholesterol esters). Further studies have been supporting the hypothesis that the **TPEF** signal is related to the lipid-rich substances in the plaques [148].

The kurtosis and the skewness of the gray level intensity histograms were calculated and the results are shown in Fig. 5.4. The skewness value is a first order texture feature that measures the extent to which the pixel intensity values are not distributed in a Gaussian manner. In other words, the skewness of a set of intensity values indicates the imbalance between extents of areas (or number of pixels) that are darker or lighter than the mean.

On the other hand, even-order statistics (e.g. variance and kurtosis) are always the same for an image and its negative, so that they are blind to any asymmetries in light and dark (such as those that occur with highlights and shadows). The kurtosis is a measure of the spread of gray tones about the mean.

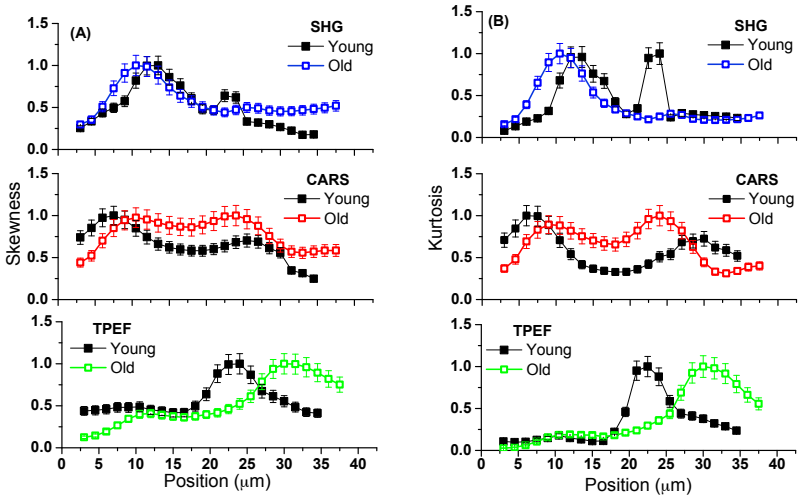


**Figure 5.4:** First order statistics: (A) skewness and (B) kurtosis. Features were individually calculated for each **NLO** imaging modality (**TPEF**, **CARS**, and **SHG**) and were analyzed as a function of depth and specimen age, where the old and young groups correspond to 18 and 24 month-old, and 4 and 10 month-old specimens, respectively. *Adapted with permission from Mostaço-Guidolin, Leila B., et al."Evaluation of texture parameters for the quantitative description of multimodal nonlinear optical images from atherosclerotic rabbit arteries." Physics in Medicine and Biology (2011) [16]. Copyright 2011 IOP Publishing Ltd*

According to data presented in Fig. 5.4, due to the formation of fibrous caps, the **SHG** signal from the old rabbits presents an asymmetrical pattern more superficially localized than the **SHG** pattern observed in plaques of younger animals. The maximum value of the asymmetry is located approximately $4\mu m$ deeper in young animals than in the old specimens.

The **CARS** images show a bimodal variation in skewness and kurtosis as a function of depth into the vessel's wall. In the more fully developed plaques, high values of skewness and kurtosis extend deeper into the wall of the aorta (approx. $10\mu m$ to $25\mu m$). Considering that the **CARS** signal is associated with lipid deposits and that the old plaques characteristically have deeper and more extensive accumulation of lipids than the plaques in young animals, the skewness and kurtosis measures are consistent with the lipid profiles observed in these plaques.

The **TPEF** images show similar depth dependence for both texture features. Young plaques present a maximum in skewness and kurtosis at around $20 - 25\mu m$ below the surface; on the other hand, the maximum of these parameters for the old plaques occur

around $25 - 35\mu m$ below the surface. Glossy structures in the images (Fig. 5.1)can be observed $10\mu m$ shallower in young plaques compared to the old ones.

Five texture parameters extracted from the co-occurrence gray level matrix (**GLCM**) were selected from the 14 defined by Haralick *et al.*: inverse difference moment (**IDM** ), energy, inertia, entropy, and correlation. In Fig. 5.5, data related to the **IDM** , energy and contrast are presented. Considering that the **IDM** (also called local homogeneity) quantifies the local similarities inside the computational window, it is expected to be larger for **GLCM**s with elements concentrated near the diagonal. These **GLCM**s correspond to textures of organized and poorly contrasted features, with only a few gray levels at the same distance d from one another. This parameter quantifies the degree of homogeneity in the region of interest.

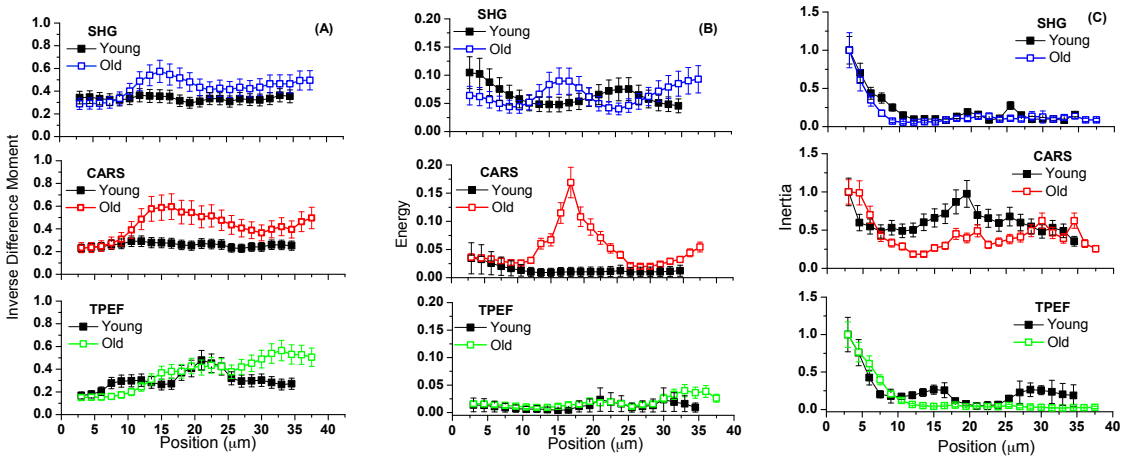


**Figure 5.5:** Second order parameters extracted from the **GLCM**: (A) Inverse difference moment (**IDM** ); (B) Energy; (C) Inertia. Features were individually calculated for each **NLO** modality (**TPEF**, **CARS**, and **SHG**). *Adapted with permission from Mostaço-Guidolin, Leila B., et al."Evaluation of texture parameters for the quantitative description of multimodal nonlinear optical images from atherosclerotic rabbit arteries." Physics in Medicine and Biology (2011) [16]. Copyright 2011 IOP Publishing Ltd*

In **CARS**, we observe that lipid accumulation in older plaques is more homogeneous than in the plaques of young animals (Fig. 5.5A). At approximately $25\mu m$ into the wall of the aorta, it is noted that fluorescent structures (**TPEF** channel) detected in old plaques tend to be more homogeneous than those identified in young plaques. However, this texture feature for the collagen fibril distribution (**SHG** channel) showed no significant

statistical difference between the young and old plaques.

The energy feature, shown in Fig. 5.5B, is sometimes referred to as the second angular moment or uniformity of the **GLCM**. The lowest value of the energy is attained when all the $P_d, \theta(i, j)$ are equal, and there are no dominant gray levels. Most gray levels are equally probable.

The energy parameter associated with the **TPEF** channel has a constant and low value over the depth of the optical scan; energy values for the **SHG** channel show some variations, but they are not statistically significant. On the other hand, the energy parameter calculated for the **CARS** images shows a distinctly different depth profile between the younger and older plaques.

The high energy values observed in the **CARS** signal from older plaques at a depth centered around $18\mu m$ show that only a few gray levels dominate the image at this depth. The region inside the computational window is more homogeneous or exhibits some regular structures. In this case, regular structures are concentrated only at the region between depths of $10\mu m$ and $30\mu m$ from the surface of the plaque developed by the old animals. Based on this observation of energy variation it is possible to locate the depth and size of the lipid core. They are significant histological features of a plaque, where the amount of thrombogenic (lipid) material is related to its potential to cause a significant ischemic event.

The inertia texture feature, presented in Fig. 5.5C (also called second difference moment), is very sensitive to large differences occurring inside the co-occurrence matrix. Highly contrasted regions will have a high inertia, whereas more homogeneous regions will have a low inertia.

Inertia data from **SHG** and **TPEF** present similar contrast level in both old and young plaques. Meanwhile the inertia from the **CARS** signal shows some fluctuation concentrated at the intermediate portion of the plaque (around $10\mu m$ and $30\mu m$). It can be related to the lipid accumulation inside the necrotic core, being more homogeneous in the plaques developed by old animals.

Finally, additional information can be acquired by analyzing the entropy and the

correlation of the **NLO** images. The correlation quantifies the dependence of gray levels between two pixels separated by a distance $d$. Low correlation means that the gray levels are generally independent from one another, i.e., there is no regular structure in the image. However, if correlation is high, there is a high probability that one or several patterns repeat themselves inside the computational window. The entropy measures the lack of spatial organization inside the computational window.

The entropy is high when all $P_d, \theta(i, j)$ are equal, which corresponds to a rough texture, and low when the texture is more homogeneous or smoother. Collagen fibers in young plaques tend to be spatially more randomly distributed compared to the collagen network observed in older plaques. Therefore, this denser and more homogeneous distributed collagen network in older plaques can be identified by the entropy and correlation of the **SHG** images, as shown in Fig. 5.6.

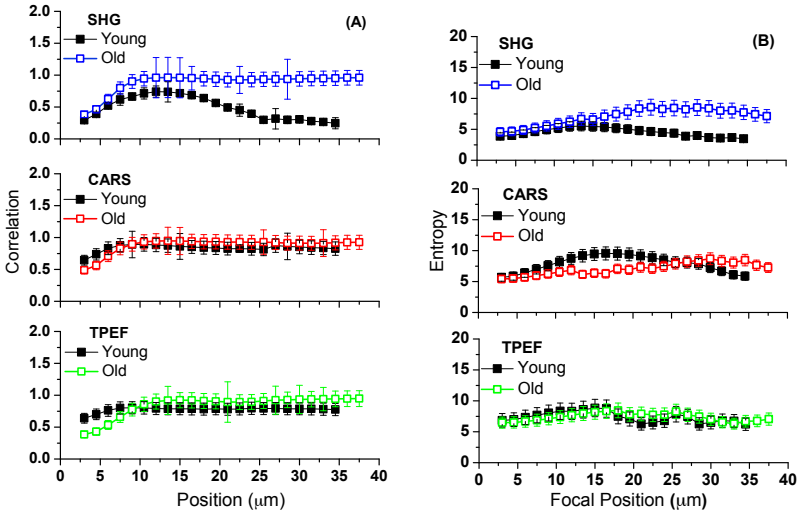


**Figure 5.6:** Second order parameters extracted from the **GLCM**: (A) correlation and (B) entropy. Features were individually calculated for each **NLO** modality (**TPEF**, **CARS**, and **SHG**), being analyzed as a function of plaque depth. *Adapted with permission from Mostaço-Guidolin, Leila B., et al."Evaluation of texture parameters for the quantitative description of multimodal nonlinear optical images from atherosclerotic rabbit arteries." Physics in Medicine and Biology (2011) [16]. Copyright 2011 IOP Publishing Ltd*

The entropy of the **CARS** images could also be useful for tracking the randomness of lipid accumulation in young plaques. Entropy values from **CARS** images increase with depth in young rabbits and they are consistent with the observation that older, more

developed plaques tend to have larger lipid pools filled by homogeneously distributed lipid structures, therefore presenting lower entropy values.

## 5.2 Evaluation of plaque and healthy regions

Texture features were sensitive to the changes occurring in the vessel wall, related to plaque development. In Fig. 5.7, several morphological differences among healthy and plaque regions can be observed. Healthy vessel wall (Fig. 5.7a) are mainly characterized by the presence of distinctively defined elastic fibers, which generates strong **TPEF** signal. It looks distinguishably different from atherosclerotic lumen, shown in Fig. 5.7b.

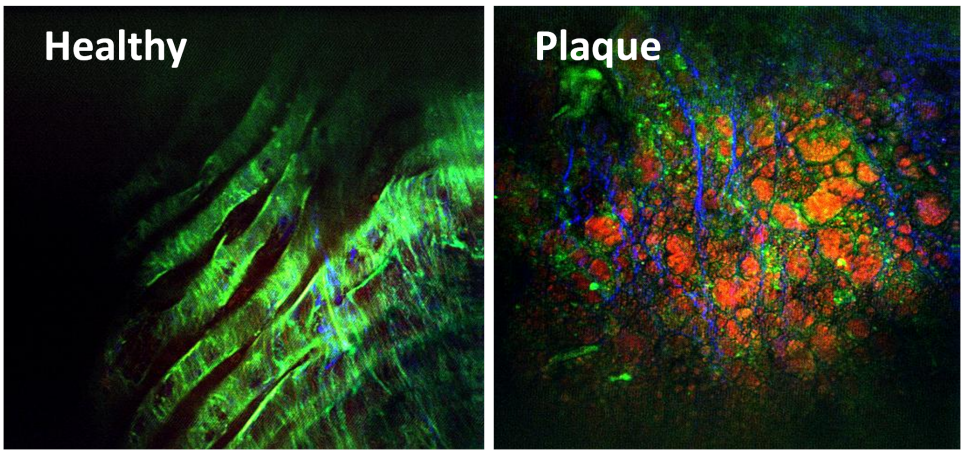


**Figure 5.7:** Images acquired with 20x dry lens from **WHHLMI** rabbit's aorta. **NLO** microscopy from plaque region with oxi-LDL particles color-coded in green (**TPEF**), lipids in red (**CARS**), and collagen fibrils in blue (**SHG**). Healthy region where the elastin fibers are color-coded in green (**TPEF**). Both **SHG** and **CARS** signals are collected in the forward-direction while **TPEF** is collected in the backscattered (epi-) direction. *Reprinted with permission from Mostaço-Guidolin, Leila B., et al."Quantitative nonlinear optical assessment of atherosclerosis progression in rabbits.", Analytical Chemistry (2014) [17]. Copyright 2014 American Chemical Society.*

Five first order statistical parameters (mean, standard deviation, integrated density, kurtosis, and skewness) and five texture parameters extracted from the co-occurrence gray level matrix (**GLCM**): inverse difference moment (**IDM** ), energy, inertia, entropy, and correlation were calculated for both plaque and healthy regions. They are presented in Fig. 5.8 and Fig. 5.9, respectively.

Using the non-parametric Kruskal-Wallis statistical test (considering $p < 0.05$), it

was determined that mean, standard deviation, and the integrated deviation were able to better distinguish and quantify changes that occur in healthy arterial vessel as function of the plaque development. With exception of the integrated density, all others were sensitive to changes occurred with **SHG** signal, as **SHG** signal is significantly high in plaque regions.

As the source of **TPEF** signal is different when comparing plaque and healthy regions, no significant information could be extracted from the analysis of the first order parameters.

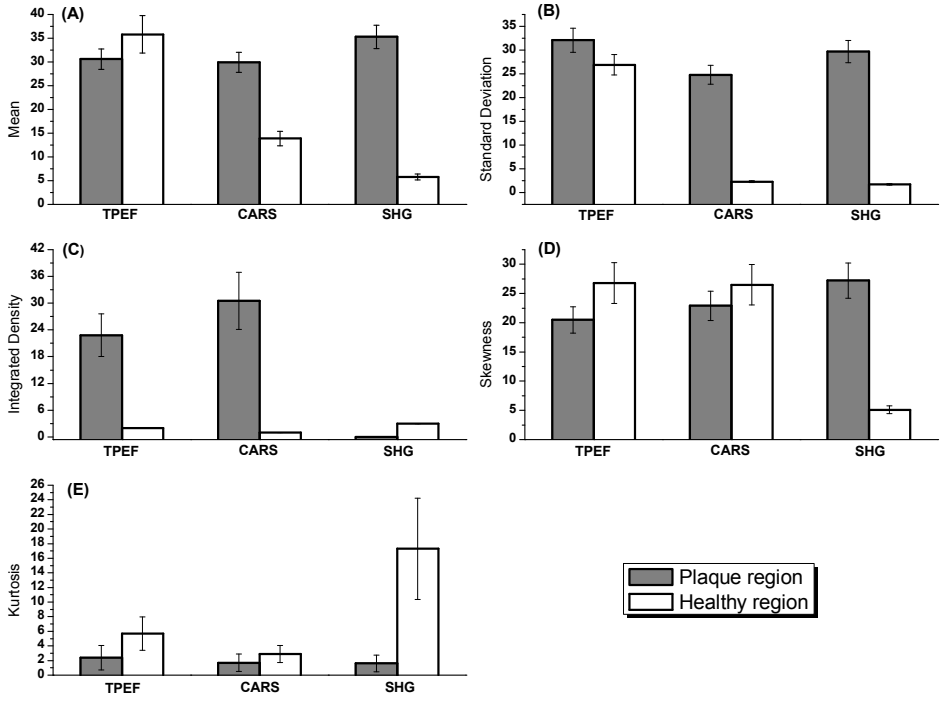


**Figure 5.8:** First order statistics: (A) mean, (B) standard deviation, (C) integrated density, (D) skewness, and (E) kurtosis. Features were individually calculated for each set of images acquired with all three **NLO** techniques (**TPEF**, **CARS**, and **SHG**). Gray bars: plaque region; White bars: healthy regions. *(© L.Mostaço-Guidolin, 2014)*

Integrated density, contrary to what its name suggests, is not directly related to the images' intensity since, images containing spatially well defined structures (e.g. collagen and elastin fibers) tend to have low integrated density values.

As it can be seen, in both **TPEF** and **CARS** exhibit higher value in integrated density due to more homogeneous distribution of particles and/or structures. In **SHG** however, shows the reverse because of formation of well-defined fiber structure.

The kurtosis and the skewness of the gray level intensity histograms were also calculated and the results are shown in the Fig. 5.8D and Fig. 5.8E. According with data presented in Fig. 5.8D, they are statistically compatible according to the Kruskal-Wallis test; however, skewness is only useful in **SHG** images.

Similarly, in kurtosis data shown in the Fig. 5.8E it is only useful in differentiating **SHG** images acquired from healthy or atherosclerotic regions. Images from plaque regions are characterized by a narrow distribution with short tails around the mean value of gray levels. **SHG** images from healthy regions have a broad gray level distribution with long tails around the mean value. Since it is possible to detect sparse collagen fibrils in healthy regions, the detected signal contains many gray level values, characterized by a more spread distribution, presenting histograms with gray levels from 0 to 255.

Five **GLCM** texture parameters obtained from healthy and plaque regions are shown in Fig. 5.9.

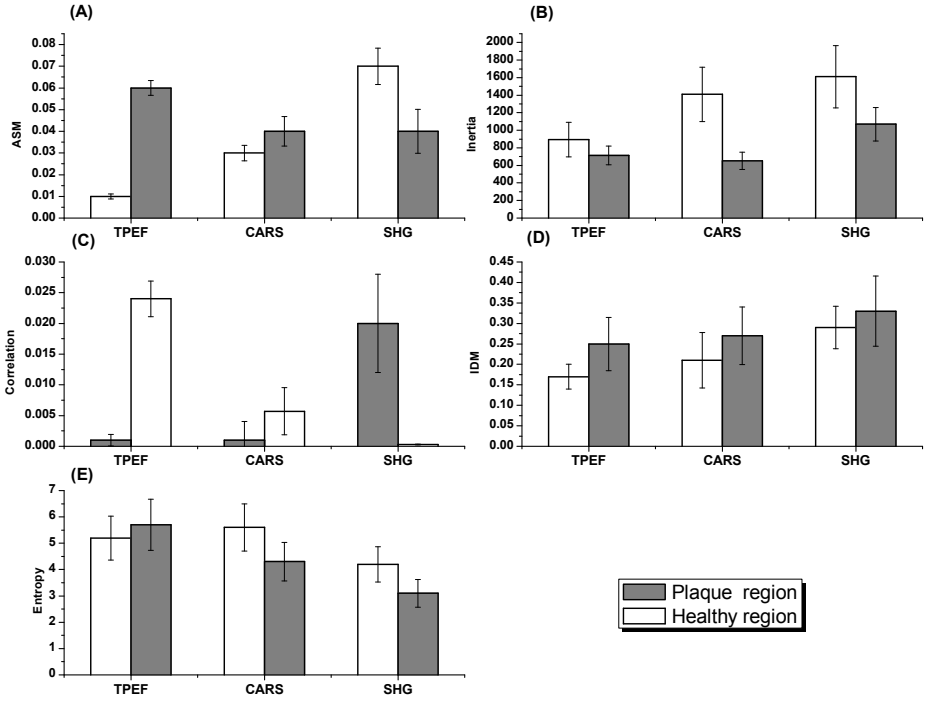


**Figure 5.9:** Second order parameters extracted from the **GLCM**: (A) angular second moment (**ASM** ); (B) inertia; (C) correlation; (D) inverse difference moment (**IDM** ) and (E) entropy. Features were individually calculated for each set of images acquired with all three **NLO** techniques (**TPEF** , **CARS**, and **SHG**). Gray bars: plaque region; White bars: healthy regions. *(© L.Mostaço-Guidolin, 2014)*

Although the **ASM**, **IDM**, and entropy did not present significant difference, the inertia, presented in Fig. 5.9B, was very sensitive to highly contrasted regions. Information acquired from **TPEF** present similar contrast level in both plaque and healthy regions. Meanwhile the inertia from the **CARS** images shows better contrast, with the atherosclerotic plaques regions displaying lower value than healthy regions. For example, it can be related to the lipid accumulation inside the necrotic core, where shows a more homogeneous distribution of **CARS**-contrasted structures.

The correlation parameter quantifies the difference in the recorded gray levels between two pixels separated by distance a $d$. Healthy regions are characterized by the presence of elastin fibers, detected by the **TPEF** channel. As these fibers are regular structures, the correlation values of **TPEF** images in healthy regions are high (Fig. 5.9C).

The same principle also apply in **SHG** images from plaque regions, as those images are dominated by well-defined collagen network, leading to high correlation values in plaque. In **CARS** images the presence of lipids droplets, gives a higher correlation value compared to the tissue background dominating the healthy vessel wall.

As a general conclusion for this chapter, it is clear that the texture analysis emerges as an important tool to be considered in the analysis of images acquired through **NLO** microscopy. Due to the biological complexity of this problem, we need to consider several parameters to characterize images acquired through all three modalities in order to better quantify those alterations. However, by combining several texture parameters, the process of correlating the results with the biological meaning of the problem can become challenging.

# Chapter 6

# Classification of atherosclerotic plaques

Until now we have demonstrated that the texture parameters are capable of providing certain power in differentiating plaque burden. The next step is to test if we can correlate these imaging statistics with clinical classification of atherosclerosis. This would enable a better description of atherosclerotic lesions using clinical standards.

## 6.1 ACC/AHA definitions for plaque classification

Currently, the 1995 **ACC/AHA** (American College of Cardiology/American Heart Association) definition for atherosclerotic lesions is the most widely used classification system, defining six lesion categories based on their histological features. This definition are summarized in Table 6.1.

| | | Description |
|---|---|---|
| Type I | Initial lesion | Isolated, scattered macrophage foam cells at the luminal proximity with adaptive intima thickening. |
| Type II | Fatty streak | Layers of foam cells closely spaced in the thickened region of the intima. The term "intimal xanthoma" has been proposed for this alteration. |
| Type III | Intermediate lesion | Pathological intimal thickening with aggregates of lipid-laden cells and scattered extracellular lipid droplets with no necrotic lipid core. |
| Type IV | Atheroma | Confluent accumulation of extracellular lipid and debris forming a necrotic core. |
| Type V ($V_a$) | Fibrous atheroma | Plaque with a well-formed necrotic core covered by a fibrous cap. |
| Type VI | Complex lesion | Surface defect, hematoma, or thrombosis. |
| Type VII ($V_b$) | Calcific atheroma | Collagen-rich atheroma with large mineralized area dominating the core region. |
| Type VIII ($V_c$) | Fibrotic lesion | Fibrous tissue predominates. |

**Table 6.1:** Classification of atherosclerosis lesions according to the **AHA**'s Committee and authorities [1].

The initial Type I lesion contains isolated macrophage foam cells and exists already early in life. Type II lesions are macroscopically visible as small fatty streaks and present in over 65% of 12-14 year old children [69].

Ongoing lipid accumulation and the presence of extracellular lipids form the intermediate Type III plaque. In Type IV lesions these small lipid deposits have transformed into a larger central lipid pool, and the deposition of fibrous material characterizes Type V plaques. With the migration of **SMC**s into the intima, their phenotype is altered and the subsequent ECM accumulation gives rise to fibroatheromatous or Type Va lesions. In Type Vb lesions are partly calcified and Type Vc lesions have a relatively small lipid component, but fibrous tissue predominates.

The Type VI lesions may give rise to plaque rupture (VIa), intraplaque hemorrhage (VIb) or thrombosis on a non-ruptured plaque (VIc), which consists in a sequence of events that eventually may lead to arterial occlusion and critical ischemia of end organs.

Alternatively, in 2000, Virmani *et al.*proposed a classification to describe advanced

atherosclerotic lesions more adequately with regard to plaque stability [149]. Fibrous lesions (Type 1) and atheromatous plaques (Type 2) are considered stable, while thin cap fibroatheroma (TCFA, Type 3) with a relatively large necrotic core ($> 40\%$) and thin fibrous cap ($< 65\mu m$) are perceived as unstable.

Healed cap ruptures (Type 4) and acute plaque disruption or intraplaque hemorrhage (Type 5) is a distinct sign of plaque destabilization. In this classification, Type 6 lesions are described as plaque erosion which is defined as vascular thrombosis without any sign of fibrous cap discontinuity.

This classification system was used as reference, to validate the proposed methodologies, the **OIPB** and texture analysis, for plaque burden classification.

## 6.2 Plaque classification based on its features and NLO images

The images used for this part of the study were acquired directly from the lumen of the atherosclerotic arterial segments (unsectioned bulk). However, to better select regions that could be reliably linked to specific plaque levels, images acquired from tissue sections were examined and were used as guides.

Figure 6.1 shows how **NLO** images can be correlated with the description defined by **AHA** Committee, for classifying atherosclerotic lesions.

A total of 160 **NLO** images acquired from 28 rabbits were used in the classification. The age of the rabbits ranged from 0 to 27 months. Based on characteristics such as the presence of collagen, lipid-rich cells, shape, size and layers organization, the images were first visually examined and then manually divided into 4 distinct groups, as shown in Fig. 6.1. Images were assembled into groups A,B,C,D composed of 45, 31, 48, and 36 images, respectively.

Group A mainly represent healthy artery; group B present features seen in lesions Type I and II, which still considered initial. Group C is composed by images taken from more advanced lesions (Types IV and V), containing well-formed necrotic core

and fibrous cap. Finally, group D present features observed in most advanced lesions, classified as Types VI and VII plaques.

| | | Description | |
|---|---|---|---|
| 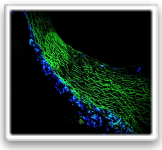 | Healthy | Absence of lipids, collagen and/or calcification within the intima and intermediate layers. | **Group A** |
| 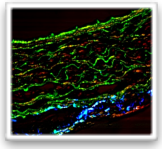 | Type I Initial lesion | Isolated, scattered macrophage foam cells at the luminal proximity with adaptive intima thickening | **Group B** |
| 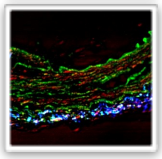 | Type II Fatty streak | Layers of foam cells closely spaced in the thickened region of the intima. The term "intimal xanthoma" has been proposed for this alteration. | |
| 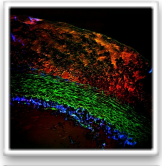 | Type IV Atheroma | Confluent accumulation of extracellular lipid and debris forming a necrotic core | **Group C** |
| 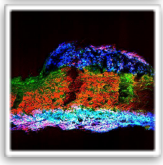 | Type V Fibrous atheroma | Plaque with a well-formed necrotic core covered by a fibrous cap | |
| 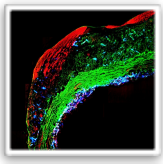 | Type VI Complex lesion | Surface defect, hematoma, or thrombosis | **Group D** |
| 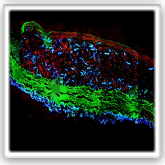 | Type VII (Vb) Calcific atheroma | Collagen-rich atheroma with large mineralized area dominating the core region | |

**Figure 6.1:** Simplified scheme for classifying atherosclerotic lesions modified from the current **AHA** recommendation. Examples of how each lesion looks like under the **NLO** microscope are shown in the first column. The groups used to classify all images are also presented(A-D). Images presented in the first column are color coded as: blue represents collagen (**SHG**); red represents lipid-rich structures (**CARS**); green (**TPEF**) represents either elastin (healthy) or fluorescent particles (plaque).

The **OIPB** was obtained for each image. Healthy regions tend to have negative **OIPB** values while most advanced lesions show values above 60.

The distribution of values obtained for each group of images is shown in Fig. 6.2. The

average **OIPB** obtained for group A, which was composed by images taken from healthy region, is -56. As we move towards more advanced lesions, the **OIPB** value increases; the average for group B is 23; groups C and D presented higher values, at 51 and 87 respectively.

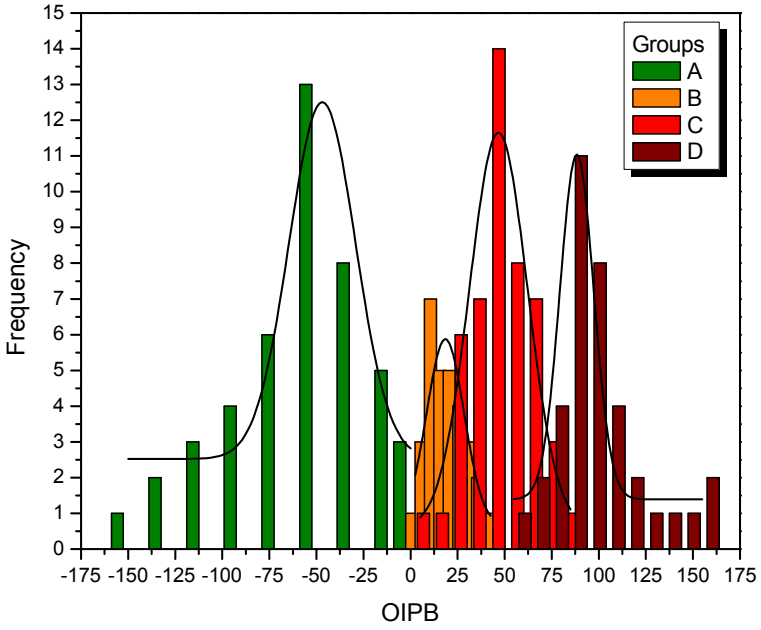


**Figure 6.2:** Correlation between **OIPB** distribution and lesion types. The features used to classify all images are based on the current **AHA** recommendation. Group A corresponds to **OIPB**s obtained from images acquired at healthy regions; groups B and C shows the **OIPB** distribution for initial and intermediate/advanced lesions, respectively. Group D is represented by severe lesions. *(© L.Mostaço-Guidolin, 2014)*

It is clear from Fig. 6.2 that these groups are reasonably well separated from each other, in particular group A and D. Some significant overlap is observed between group B and C, as they both represent intermediate stage of atherosclerotic plaque. In this sense, the **OIPB** alone could be a good parameter to differentiate early, intermediate, and severe plaque.

Additionally to the **OIPB** values, textural features were also extracted from these same images. **FOS** and **GLCM** parameters were calculated for each image from each group, and are summarized in Table 6.2.

| Parameter | Group A | Group B | Group C | Group D |
|---|---|---|---|---|
| Mean | 12.5(6) | 14.3(3) | 14.9(10) | 18.2(4) |
| Standard Deviation | 18.3(3) | 20.0(11) | 26.6(8) | 34.1(2) |
| Integrated Density | $4.0 \times 10^6(4)$ | $4.1 \times 10^6(6)$ | $3.6 \times 10^6(3)$ | $4.8 \times 10^6(2)$ |
| Skewness | 0.93(2) | 0.87(4) | 0.96 (7) | 0.94(1) |
| Kurtosis | 0.97(4) | 0.93(5) | 0.74(5) | 0.96(8) |
| Inverse Difference Moment | 0.42(6) | 0.47(10) | 0.58(4) | 0.60(7) |
| Energy | 0.03(12) | 0.06(11) | 0.04(20) | 0.11(16) |
| Inertia | 0.02(7) | 0.02(6) | 0.05(6) | 0.06(2) |
| Correlation | 0.96(3) | 0.93(17) | 1.00(5) | 0.97(9) |
| Entropy | 0.11(18) | 0.46(21) | 0.53(9) | 0.94(11) |

**Table 6.2:** Average **FOS** and **GLCM** texture parameters and their errors, obtained for each group. Group A is composed from images acquired from healthy regions; groups B, C and D are composed from images representing progressively advanced atherosclerotic lesions.

Comparing the values obtained for each group, one can notice that the mean, standard deviation, inverse difference moment, and the entropy present crescent values, when comparing healthy regions (group A) among plaques with increased severity levels (groups B,C, and D).

With exception of the skewness and kurtosis, all other features showed significant statistical difference when comparing the most extreme groups (A and D). The intermediate plaque levels (groups B and C) presented consistently compatible values for most of the features extracted.

Different from what was presented earlier, the texture parameters were extracted from images generated by the combination of all three channels - or techniques - **SHG**, **CARS** and **TPEF**. In general, as the lesion advances, more complex structures can be observed, and consequently, textural features will become distinguishable.

For example, as previously shown in Fig.5.7, healthy regions are mainly characterized by the absence of collagen and lipid-rich cells. These images show arterial elastic fibers, distributed along the image. As the plaques start to appear, small lipid droplets are observed and the overall image pattern starts to change. Finally, when observing more advanced lesions, images containing complex features are detected.

A classification of these images was then performed based on **OIPB**, **GLCM**, and

**FOS**. The combination of the **OIPB** with texture analysis could have the potential to improve the images classification from all 4 groups, by enhancing accuracy, sensitivity and specificity.

### 6.2.1 Atherosclerotic lesions classified by support vector machine (SVM)

As discussed in the Sec. 3.5.5, **SVM** is a classification method commonly used in bioinformatics and it is known for its ability to deal with high-dimensional data and flexibility for modeling diverse sources of data (refs). **SVM** performs classification by constructing an N-dimensional hyperplane that optimally separates the data into different categories. Using a nonlinear **SVM** classifier, we tested the ability of the **OIPB** and texture parameters to classify distinct groups of atherosclerotic plaques. More information regarding the parameters used for classifying **NLO** images, such as the definition of training and test sets, were presented in Sec. 3.5.5.

The overall performance of **SVM** classifier is shown in Table 6.3. The results shown are referent to image classification performed considering one *versus* all.

| **Parameters** | **Accuracy** (%) | **Sensitivity** (%) | **Specificity** (%) |
|---|---|---|---|
| OIPB | 90 | 87 | 88 |
| Texture (FOS) | 63 | 68 | 59 |
| Texture (GLCM) | 70 | 66 | 70 |
| OIPB + Texture | 98 | 96 | 97 |

**Table 6.3:** Summary of the **SVM** classification results obtained considering the **OIPB** and textural features. The accuracy, sensitivity and specificity presented were obtained by comparing images from a specific group against all remaining others.

The nonlinear **SVM** classifier showed an overall accuracy of 90% when only the **OIPB** values were included in the classification model. Accuracy drops to 63% and 70% when only textural features (**FOS** or **GLCM** parameters) were used, respectively. However, when combining the **OIPB** and texture parameters, the accuracy increase to 98%.

In Chapter 4, it was shown that the **OIPB** has a great potential for differentiating

lesions severity based on the **NLO** images.

However, since the **OIPB** is an intensity-based parameter, it has difficulties in quantifying features that involve morphological changes.Textural features, on the other hand, are able to track the spacial pixel distribution, and consequently can expose information related to the plaque morphology.

Based on the obtained results, **FOS** showed limited capacity for classifying images correctly. **FOS** parameters, similar to the **OIPB**, are also intensity-based. However, it shows that the **OIPB** is a better parameter than **FOS** for classification.

The reason could be that the **OIPB** also considers the relationship among all three biocompounds instead of simply tracking their increase/decrease during the plaque development.

When **GLCM** parameters were tested, one can notice that the overall accuracy increased when compared to the **FOS** parameters-only. However, its performance is still below the one achieved with the **OIPB**.

The combination of the **OIPB** with all texture parameters showed a noticeable gain in accuracy, sensitivity and specificity, reaching more than 95% in all three metrics. It shows that texture analysis can be used as a complementary data to classify atherosclerotic lesions, based on **NLO** images.

While textural features are tracking changes related to the image pixel distribution (Sec. 3.5.1), and the **OIPB** is able to successfully distinguish variations regarding plaque components; when combined, they provide a novel and powerful way to define atherosclerotic lesions based on the **NLO** images.

# Part II

# Specific image features & classification: tools for characterizing NLO images

# Chapter 7

# Collagen morphology and texture analysis: from statistics to classification

In this chapter we present the application of texture analysis to quantify morphological changes in tissue collagen fibril organization caused by pathological conditions.

Similar to the procedure adopted in early chapters of this thesis, features based on first-order statistics (**FOS**) and second-order statistics such as gray level co-occurrence matrix (**GLCM**) were explored to extract **SHG** image features that are associated with the structural and biochemical changes of tissue collagen networks.

A variety of pathological conditions in humans directly or indirectly involve remodeling or regenerating the collagenous framework in tissue. Some of these conditions are characterized by excessive collagen deposition while others present altered collagen organization (e.g., cirrhosis, scleroderma, keloid, pulmonary fibrosis, diabetes) [150–154].

Abnormal deposition of collagen may impair vital functions, and changes in the architecture of the focal collagen network may also lead to disabling conditions [155, 156]. The ability to accurately characterize collagen morphology is therefore an essential component in the pursuit of ultimate understanding of these pathologies.

Traditionally, tissue collagen organization is inspected using histochemistry, immuno-

histochemistry as well as in situ hybridization. These standard methods require multiple steps of tissue processing and such sample preparation can lead to un-desirable morphological alterations in the extracellular matrix. Several imaging methods, such as **MRI** [157, 158], small angle X-rays [159, 160], and electron microscopy [14] were tools developed in the past for direct imaging of collagen without the need for tissue processing. However, these imaging modalities often suffer from low chemical specificity and low spatial resolution. Special experimental conditions are often required for some procedures that can damage tissue structure permanently.

Despite the success of **SHG** microscopy in biomedical research, most published work relied on **SHG** imaging to describe collagen organization without using quantitative measures. In most studies, collagen **SHG** images were presented to describe empirical observations that were linked to a particular pathological condition. While understanding these empirical associations between collagen **SHG** images and pathology is important, it is equally important to be able to track such correlation using quantifiable measures for objective comparison. To date, quantitative collagen analysis methods have largely relied on image pixel-counting applied to histological images of tissue [161, 162].

Others have also used X-ray diffraction, **MRI** and electron microscopy images for collagen quantification but with less success [163, 164]. Despite these efforts, none of these methods was able to reliably define distinct collagen patterns based on pre-defined quantitative parameters and there are no reports in the literature on how to develop quantitative collagen pattern classification.

Quantitative **SHG** imaging has not received much attention among researchers until recently. Several **SHG** collagen studies have recently proposed new methodologies for quantifying imagery features [165–171]. These studies, however, either used simple image pixel intensity-based approaches [165–168], or only analyzed histological tissue sections, not intact bulk tissues [169–171].

In this chapter we present a methodology capable of quantifying changes in collagen networks caused by various pathological conditions. The method described fills an existing gap in the literature where empirical interpretation of **NLOM** images is used

to classify tissue's biochemical morphology. We explored the use of texture analysis tools to extract **SHG** image features that are related to the structural and biochemical changes associated with collagen network pathologies in both sectioned and intact tissues. We also performed multi-group classification of **SHG** images based on these extracted quantitative parameters.

Two types of collagenous tissue, infarcted myocardium (heart muscle) of rats and atherosclerotic arteries of rabbits, were used to develop and to test the proposed methodology. In the infarcted myocardium, collagen re-modeling occurs to repair the damage caused by myocardial infarction [172]. A recent study indicated that treatment of infarcted hearts using adipose-derived stem cells (**ASC**s) influenced the collagen remodeling process by reducing collagen deposition in the infarcted zone [173]. In this study, **SHG** images of collagen type I fibrils of tissue sections from the stem cells-treated hearts and un-treated hearts were compared using texture analysis. A binary classification based on images acquired from **ASC**s-treated and un-treated hearts, was subsequently performed.

A multi-group classification was tested subsequently to determine accuracy of the proposed method. The texture analysis method reported in this chapter is not limited to the conditions highlighted in this thesis. In fact, this method can be easily applied to a wide range of conditions involving collagen re-modeling.

While others have reported imaging of stem-cell treated infracted rat hearts with **TPEF** and **SHG** microcopy [174], our study was the first to characterize focal collagen organizational features in an infracted myocardium [20].

## 7.1 Texture analysis of SHG images of collagen remodeling occurred in infarcted rat hearts

A rat model of myocardial infarction was originally developed to study therapeutic potential of adipose-derived stem cells (**ASC**s) for treatment of heart failure [173]. Histological and MRI studies have both confirmed that **ASC**s reduced infarct size and im-

proved cardiac contractile function of the infarct rat hearts. In this section, we examined the utility of texture analysis of nonlinear optical images (mainly **SHG**) for quantitative tracking of the changes related to collagen fibril remodeling in the **ASC**s-treated and un-treated infarcted rat hearts.

Representative **SHG** collagen images from un-treated, **ASC**s-treated infracted rat hearts and non-infarcted heart are illustrated in Fig. 7.1a, 7.1b and 7.1c, respectively. Significant reduction of collagen deposition in the **ASC**s-treated infracted heart is clearly seen while the lack of collagen is also evident in non-infarcted heart. This observation is consistent with previous findings [173] in which **ASC**s demonstrated therapeutic effect in improving cardiac function via enhancement of cardiomyocyte regeneration and suppression of collagen fibrillogenesis.

The collagen density in images Fig. 7.1a and 7.1b was calculated using a simple threshold pixel counting method. The result shows approximately a 50% drop in collagen density for the **ASC**s-treated rat hearts compared to the un-treated hearts, which is also consistent with previous data [173]. More importantly, the **SHG** microscopic images reveal a highly–directional and organized collagen fibril morphology in the **ASC**s-treated infarct myocardium compared to a less-organized collagen structure characterized by shorter but denser fibril bundles in the un-treated infarcted myocardium.

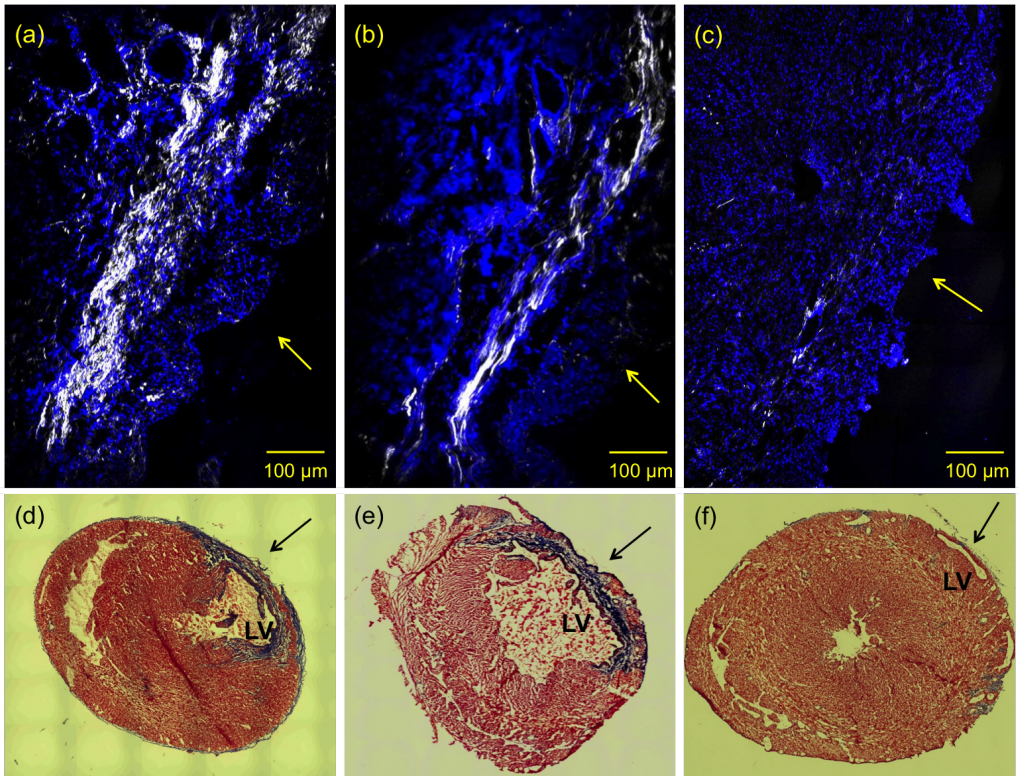


**Figure 7.1:** Co-localized **SHG** (shown in white, unlabeled) and **TPEF** (shown in blue, labeled with DAPI) images visualize collagen fibril organization and cardiac muscle cell nuclei, respectively, in the histological section of infarcted myocardium of (a) an untreated infarcted rat heart; (b) an **ASC**s- treated infarcted rat heart. (c) an image obtained from a histological section of a non-MI rat heart. Images were acquired using 10×0.45NA dry objective lens. Excitation wavelength was at 800 nm. Collagen **SHG** signal was collected using a 400±5 nm band-pass filter in the forward direction while the DAPI -TPEF signal was collected in the backscattered (epi) direction through a 505±50 nm filter. Arrows are pointing to the epicardium region. (d), (e) and (f) show representative short-axis histopathological sections of untreated, **ASC**s-treated infarct rat heart and non-MI heart, respectively. Heart tissue sections were stained with Masson's Trichrome to delineate the infarct region, and images were acquired using 53 objective lens. LV: left-ventricle. *Reprinted with permission from Mostaço-Guidolin, Leila B., et al."Collagen morphology and texture analysis: from statistics to classification.", Scientific reports 3 (2013) [20]. Copyright 2013 Nature Publishing Group.*

Additionally, representative images of histopathological sections obtained from **ASC**s-treated, un-treated and control heart are illustrated in Fig. 7.1d- 7.1f. Compared to the un-treated infarcted heart, **ASC**s-treated infarcted hearts contain a larger percentage of viable myocardium in the infarct zone.

Changes in collagen fibril morphology such as fibril length, fibril thickness, fibril alignment are tracked by texture analysis of **SHG** images using first-order statistics (**FOS**) and second-order statistics such as gray-level co-occurrence matrix (**GLCM**).

**FOS** textures are directly related to the gray tone distribution of pixels intensity and ignore inter-pixel correlations. In contrast, image second-order statistics depend on the spatial arrangements of pixels intensities present in the region of interest (**ROI**). It is a measure of the probability of a pair of pixel values occurring at selected distances apart in the image, providing textural information for that region. This probability function is known as co-occurrence matrix. In other words, **FOS** are parameters extracted directly from the original image while second-order statistics are derived from a matrix (e.g. gray-level co-occurrence matrix) that is built upon inter-pixel correlation of the original image [175].

Figure 7.2 shows the distribution of values extracted from 90 images for each texture parameter selected from a set of **FOS** and **GLCM** parameters. These texture parameters provide a means of capturing and quantifying the morphological changes on these images.

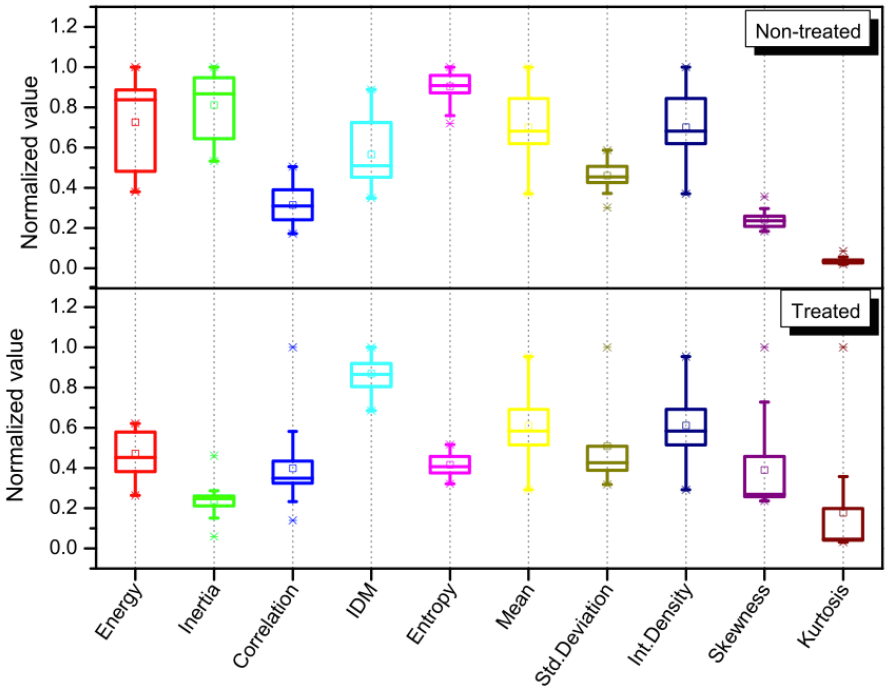


**Figure 7.2: FOS** (mean, standard deviation, integrated density, skewness and kurtosis) and **GLCM** (energy, inertia, correlation, **IDM** and entropy) texture parameters extracted from **SHG** images of the **ASC**s-treated and un-treated infarcted rat hearts. The top and bottom of each rectangular box denote the 75th and 25th percentiles, respectively, with the median shown inside the boxes. Vertical bars extending from each box represent the 90th and 10th percentiles. *Reprinted with permission from Mostaço-Guidolin, Leila B., et al."Collagen morphology and texture analysis: from statistics to classification.", Scientific reports 3 (2013) [20]. Copyright 2013 Nature Publishing Group.*

From Fig. 7.2 , it is clear that little statistical difference exists in the **FOS** parameters between the un-treated and **ASC**s-treated infarcted rat hearts, according to the Kruskal-Wallis test. **GLCM** parameters (i.e. **IDM**, entropy and inertia), on the other hand, show distinction between these two groups. For example, the group of the **ASC**s-treated hearts has a statistically higher **IDM**, lower entropy and lower inertia values when compared to its non-treated counterpart. The Shapiro-Wilk test was applied for checking the normality of the data distribution.

## 7.2 Classification of images of the infarcted rat hearts: ASCs-treated vs. un-treated

Data classification is a supervised learning strategy that is used to analyze the organization and categorization of data into distinct classes. A widely used classifier, support vector machine (**SVM**), was chosen to test the strength of using **FOS** and **GLCM** parameters to differentiate between **ASC**s-treated from un-treated infarcted rat hearts.

**SVM** is a classification method commonly used in bioinformatics and is known for its ability to deal with high-dimensional data and flexibility for modeling diverse sources of data [118, 176]. Using a nonlinear SVM classifier, we tested the ability of the texture parameters to classify distinct groups of collagen fibers, based on the first (**FOS**) and second (**GLCM**) order features extracted from **SHG** images. Figure 7.3 shows the receiver operating characteristic (**ROC**) curve obtained by combining all texture features (both **FOS** and **GLCM**), and those obtained from individual group of features (**FOS** or **GLCM**).

The accuracy of the classifier, as represented by the area under the **ROC** curve was determined to be 0.95 when combined **GLCM** and **FOS** parameters were used for classification. This value dropped to 0.86 and 0.72 when only the **GLCM** parameters or only the **FOS** parameters were used, respectively, to classify the infarcted tissue. These values suggest that classification based on combined **GLCM** and **FOS** parameters has an improved predictive power in differentiating ASCs-treated from un-treated rat hearts

compared using either **GLCM** or **FOS** alone.

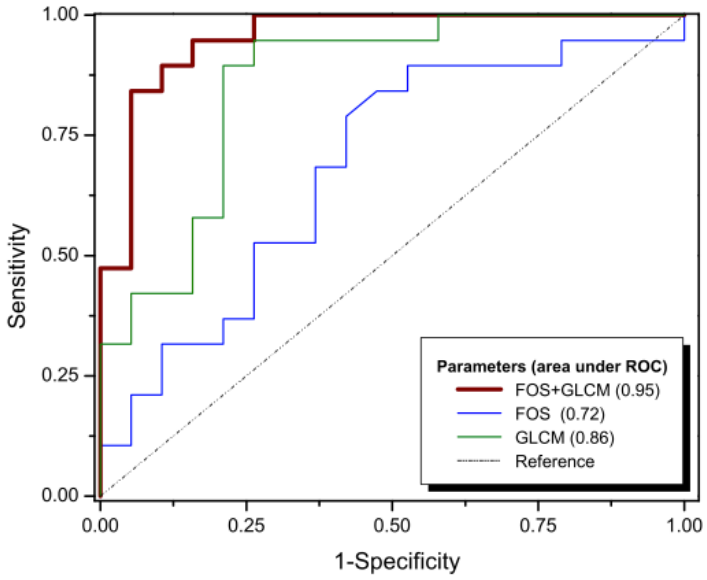


**Figure 7.3:** **ROC** curves for all three texture sets tested: **FOS**, **GLCM** and **FOS+GLCM**. Values suggest that the classification based on texture analysis has a good predictive value, as the area under the **ROC** curve was 0.95 for all texture parameters (**FOS** and **GLCM**), 0.72 for **FOS** parameters and 0.86 for **GLCM** parameters. *Reprinted with permission from Mostaço-Guidolin, Leila B., et al."Collagen morphology and texture analysis: from statistics to classification.", Scientific reports 3 (2013) [20]. Copyright 2013 Nature Publishing Group.*

In summary, the binary classification of the **ASC**s-treated and un-treated infarcted rat hearts, showed that **GLCM** parameters were able to provide effective classification with very high accuracy, conveying both high sensitivity and specificity. From Fig. 7.2, it is very clear that none of the **FOS** variables were able to reveal significant differences between the **ASC**s-treated and un-treated infarcted hearts, suggesting that the intensity-based image features were not sensitive enough to capture the variability of properties of the collagen deposited in infarcted myocardium.

**GLCM** parameters, on the other hand, consider every pixel and its neighborhood, thus generating a map that is able to account for more complex structures in the images.

Three **GLCM** parameters, **IDM**, entropy and inertia, all exhibit certain differentiating power. For **IDM**, a higher value can be associated with a denser or thicker collagen fibril structure in the **ASC**s-treated hearts.

As for entropy, a lower value typically means that the **ASC**s-treated hearts have

a more homogeneous local collagen morphology than the non-treated hearts. This interpretation is supported by the presence of thicker and better defined fibers in the **ASC**s-treated hearts (see Fig. 7.1).

Inertia is another texture parameter that quantifies the heterogeneous distribution of collagen in the un-treated hearts. A higher inertia value is often associated with a greater variability of gray levels inside a computational window. In other words, structures and/or particles are distributed within a certain area without a preferential alignment nor orientation, as one would expect in the case of fibrils.

## 7.3 Texture analysis of collagen fibrils accumulated in atherosclerotic plaques

In order to evaluate the strength and the limitations of the proposed methodology to solve more complex problems, we performed texture analysis on collagen **SHG** images acquired from bulk atherosclerotic artery tissues.

In previous studies, it has been documented that nonlinear optical imaging microscopy employing **TPEF**, **SHG** and coherent anti-Stokes Raman scattering (**CARS**) could be used to visualize extracellular morphology characteristic of atherosclerotic plaques[54-60]. Collagen remodeling throughout the progression of atherosclerosis is dynamic, complex and multi-factored.

The complexity of this process makes it a good candidate model to assess the power of texture analysis in recognizing various morphological features found in collagen networks.

The images used in this study were acquired directly from the lumen of atherosclerotic arterial segments (un-sectioned bulk) harvested from **WHHLMI** rabbits. Figure 7.4 shows examples of several collagen patterns captured with **SHG** images along the aorta affected by atherosclerotic plaques. Different patterns in the collagen distribution during plaque development are clearly evident.

A total of 414 **SHG** images acquired from 14 rabbits were used in the analysis. The age of the rabbits ranged from 2 to 24 months. Based on fibril characteristics such as

shape, size and organization, the images were first visually examined and then manually divided into 5 distinct groups by two individuals, independently. The origin of the images was blind to the examiners during this manual classification process.

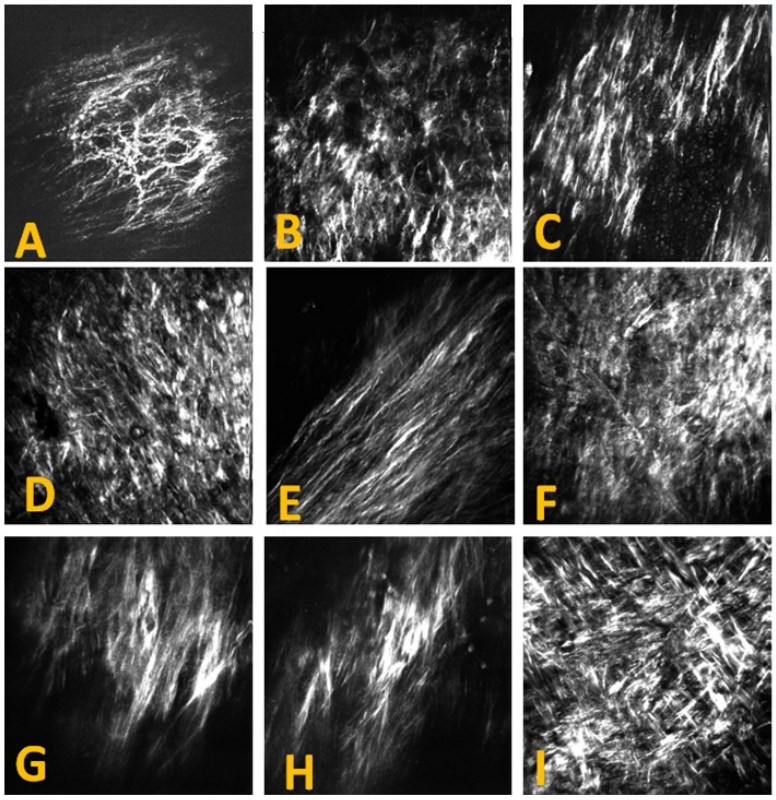


**Figure 7.4:** Epi-**SHG** images acquired from the atherosclerotic plaques in the aorta of **WHHLMI** rabbits, showing examples of different collagen fibril morphology detected on atherosclerotic artery. **SHG** images were acquired using 20x 0.75 NA dry objective lens (Olympus) and 800 nm laser excitation. A 2x digital zoom was used for imaging. Each image shown has 512 x 512 pixels or approx. 200 x 200 $\mu m$. *Reprinted with permission from Mostaço-Guidolin, Leila B., et al."Collagen morphology and texture analysis: from statistics to classification.", Scientific reports 3 (2013) [20]. Copyright 2013 Nature Publishing Group.*

Only those images that received the same categorization from both examiners were used for subsequent texture analysis. Images were segregated into groups A,B,C,D and E, composed of 87, 72, 68, 79 and 108 images, respectively. Representative images from each of the five groups are illustrated in Fig. 7.5.

Group A images are characterized by thinner, well-defined curled fibrils with a certain degree of fibril orientation. Group B images show a higher focal collagen density and more uniform fibril orientation compared to group A. In contrast, group C and D images both display a more randomly oriented network with shorter fibril length. Group E

images are marked by the presence of long, straight and uniformly orientated fibrils. Some level of correlation between distribution of the age groups and that of the 5 image groups were observed.

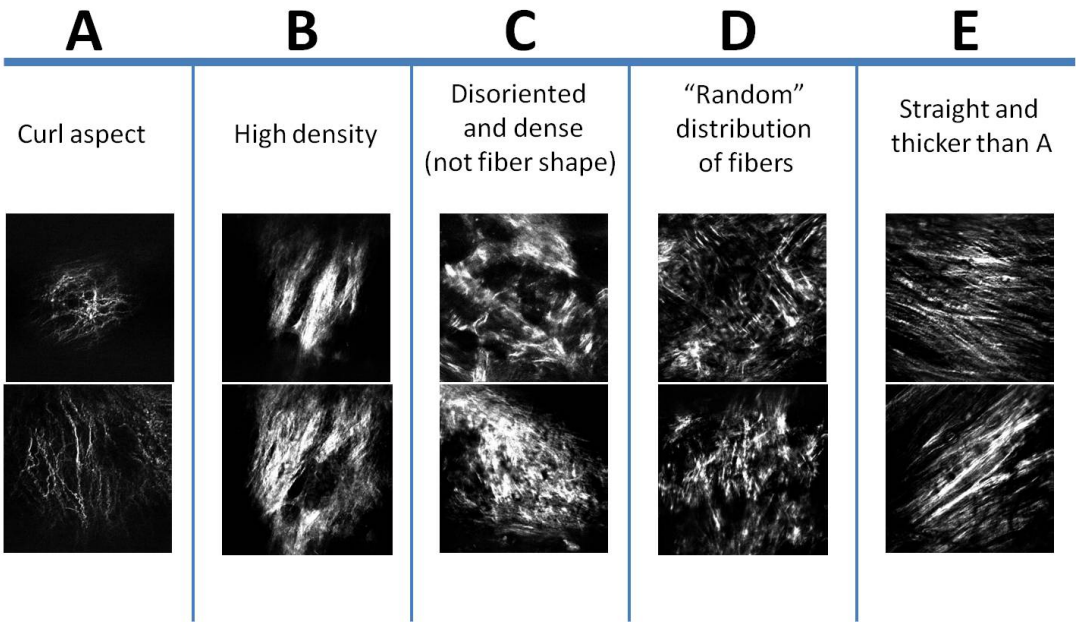


**Figure 7.5:** All collagen **SHG** images acquired from the atheriosclerotic aortic segments of the **WHHLMI** rabbits were classified into five groups A–E. Each group of the images has its own characteristic morphological features such as the fibril's shape, size and organization. Images are showing the fibrous cap, accumulated closer to the intima layer. Representative images from each group (A–E) are shown. *Reprinted with permission from Mostaço-Guidolin, Leila B., et al."Collagen morphology and texture analysis: from statistics to classification.", Scientific reports 3 (2013) [20]. Copyright 2013 Nature Publishing Group.*

While group A images could be largely correlated with younger rabbits at an age between 0 and 4 months , collagen features represented in group B-E images were mostly found in rabbits older than 6 months. Furthermore, features shown in group B and C were mainly associated with older rabbits at an age $>$ 16 months.

Five **FOS** parameters (mean, standard deviation, integrated density, kurtosis, and skewness) were calculated for all 414 images. The distributions of these **FOS** values corresponding to each group are illustrated in Fig. 7.6.

In three **FOS** parameters, mean, standard deviation, and integrated density, images in group A received low values compared to the other 4 groups, as a result of the thin and sparse fibrillar organization in this type of plaque. The distribution of skewness and

the kurtosis values of the gray level intensity histograms are also illustrated in Fig. 7.6.

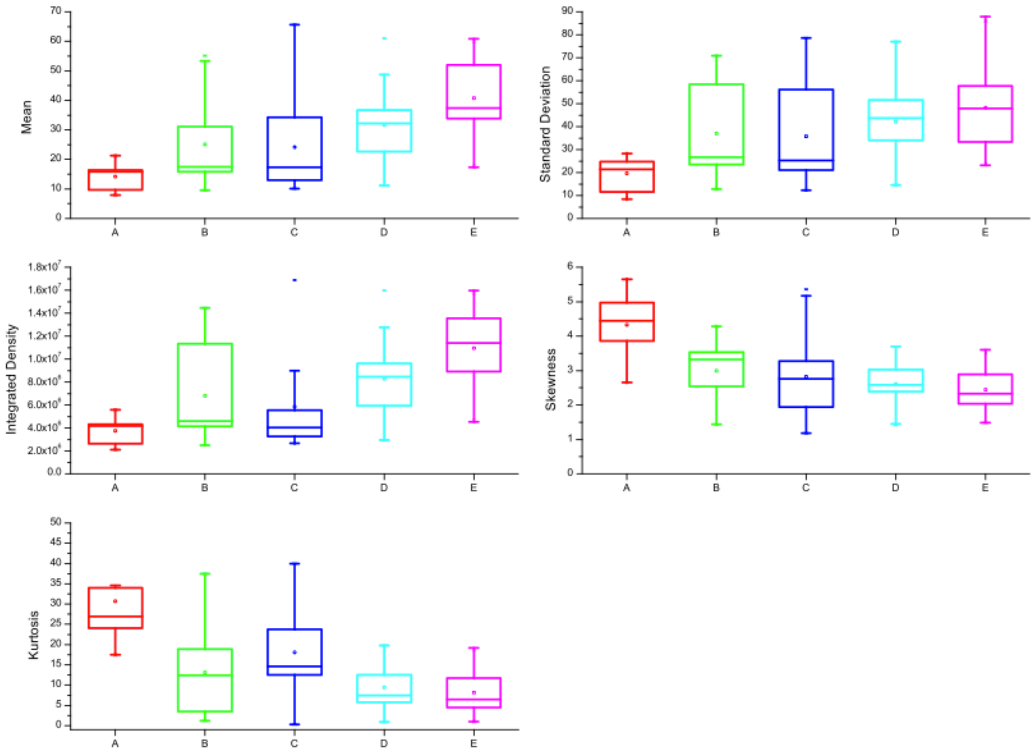


**Figure 7.6:** Comparison of texture parameters calculated for each group defined in Fig. 7.5. The top and bottom of each rectangular box denote the 75th and 25th percentiles, respectively, with the median shown inside the box. Vertical bars extending from each box represent the 90th and 10th percentiles. *Reprinted with permission from Mostaço-Guidolin, Leila B., et al."Collagen morphology and texture analysis: from statistics to classification.", Scientific reports 3 (2013) [20]. Copyright 2013 Nature Publishing Group.*

The skewness indicates the imbalance between the extent of areas (or number of pixels) that are darker or brighter than the mean. Images containing thicker fibrils, typically from older plaques, present a more asymmetrical left-tailed pattern than that captured in early plaque images (e.g. group A images). Therefore group A images display higher skewness than the other groups

While skewness is a measure of asymmetry of a distribution relative to the mean value, the kurtosis describes whether distribution of gray tones is more spread-out (flat) or it is more concentrated around the mean (peaked). In advanced plaques, most collagenous networks are better developed, generally thicker and cover larger area therefore generating stronger **SHG** signals. This usually leads to a more spread-out distribution of pixel intensities , thus lower kurtosis values.

Complementary to the five **FOS** parameters, five second-order **GLCM** parameters, inverse difference moment (**IDM**), energy, inertia, entropy and correlation were extracted from the images as well. Their values are presented in Fig. 7.1.

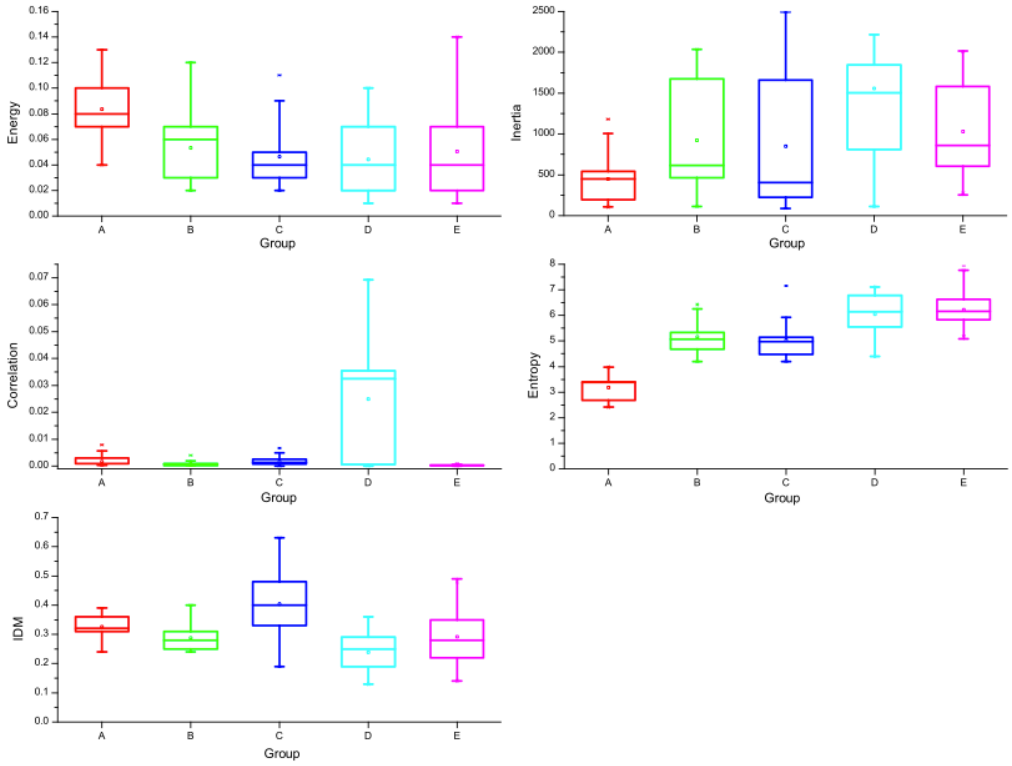


**Figure 7.7:** Values of **GLCM** texture parameters calculated from each group. The top and bottom of each rectangular box denote the 75th and 25th percentiles, respectively, with the median shown inside the box. Vertical bars extending from each box represent the 90th and 10th percentiles. *Reprinted with permission from Mostaço-Guidolin, Leila B., et al."Collagen morphology and texture analysis: from statistics to classification.", Scientific reports 3 (2013) [20]. Copyright 2013 Nature Publishing Group.*

Kruskal-Wallis test was performed to test for statistical differences between any two groups. These results indicate insufficient differentiating power for most of the tested **FOS** and **GLCM** parameters in classifying atherosclerotic collagen fibril development, when used individually. One exception is with group A, which stands out as the only group with distinct texture characteristics that can be easily differentiated from the other groups using any of the **GLCM** parameters, or some of the **FOS** parameters.

## 7.4 Multi-group classification of SHG images

A nonlinear **SVM** classifier was trained and applied to classify collagen **SHG** images of bulk atherosclerotic arterial tissues using **FOS** and **GLCM** texture parameter descriptors of the images. This time, the performance of **SVM** classifier was tested for a 5-group classification. Results are shown in Table 7.1.

| Group | Test Set | Accuracy | Sensitivity | Specificity |
|---|---|---|---|---|
| A | 6160 | 100% | 100% | 98% |
| B | 6520 | 73% | 79% | 100% |
| C | 6640 | 88% | 65% | 88% |
| D | 6360 | 90% | 86% | 94% |
| E | 4480 | 93% | 95% | 90% |
| **Overall** | **30160** | **90**% | **91**% | **92**% |

**Table 7.1:** Summary of the nonlinear SVM classification for collagen **SHG** images acquired from atherosclerotic arteries based on a 5- group model and combined **FOS** and **GLCM** parameters.

The nonlinear **SVM** classifier has an overall accuracy of 90% when 10 combined **FOS** and **GLCM** parameters were included in the classification model. Accuracy drops to 84% and 87% when only **FOS** (Table 7.2) or **GLCM** (Table 7.3) parameters were used, respectively. Sensitivity and specificity were, however, statistically unaffected. This indicates that **FOS** and **GLCM** measures are somewhat complementary to each other in terms of tracking pattern difference in these **SHG** images.

Group A was distinguished from other groups as it shows the highest accuracy, sensitivity and specificity, with little dependence upon the selection of textural parameter (Tables 7.2, 7.3). Classification of other groups, however, is more sensitive to the selection of classification parameters.

| Group | Test Set | Accuracy | Sensitivity | Specificity |
|---|---|---|---|---|
| A | 308000 | 92% | 100% | 98% |
| B | 326000 | 84% | 77% | 63% |
| C | 332000 | 83% | 64% | 88% |
| D | 318000 | 81% | 83% | 90% |
| E | 224000 | 83% | 95% | 93% |
| **Overall** | **1508000** | **84%** | **81%** | **82%** |

**Table 7.2:** Summary of the results obtained considering **FOS** texture parameters.

Based on data presented in Table 7.1, it is quite evident that group A is the most distinct group and can be easily distinguished from the other groups. The collagen textures detected in group A predominately arise from younger rabbits exhibiting early stage atherosclerosis.

The collagen fibers visualized in these images can be characterized by curlier aspect and a sparse distribution without a preferential direction. A closer look at the general results also reveals that from a pattern-recognition point of view, group A is the only group that can be separated from the other 4 groups with high confidence. Based on these observations, we can conclude that the collagen features presented in early stage atherosclerotic plaques (rabbits younger than 4 months) are distinctly different from those found in rabbits older than 6 months. This conclusion is consistent with the observation that the progression of atherosclerosis in this rabbit model proceeds faster in the younger animal and then slowly levels off after a certain age.

| Group | Test Set | Accuracy | Sensitivity | Specificity |
|---|---|---|---|---|
| A | 308000 | 100% | 100% | 92% |
| B | 326000 | 73% | 100% | 100% |
| C | 332000 | 79% | 86% | 72% |
| D | 318000 | 79% | 75% | 92% |
| E | 224000 | 91% | 98% | 92% |
| **Overall** | **1508000** | **87%** | **92%** | **91%** |

**Table 7.3:** Summary of the results obtained considering **GLCM** texture parameters.

As for groups B and C, they are mainly characterized by a lack of collagen organization. Interestingly, **GLCM** textures could not identify most of the groups as accurately as **FOS** textures (Tables 7.2, 7.3). This was one of the reasons why 5-group classifica-

tion was more accurate when both **FOS** and **GLCM** parameters were included in the classification analysis. This demonstrated the benefits of using complementary texture parameters for evaluating more complex collagen morphologies.

Overall, classifiers using the full set of calculated texture parameters (combined **FOS** and **GLCM**) give the best classification accuracy. When comparing **GLCM** with **FOS** parameters, **GLCM** textures typically give a more accurate classification than classifiers based on **FOS** textures.

In contrast to data collected from infarcted hearts, the interpretation of data collected from atherosclerotic plaques is not so straightforward due to the more complex and diverse nature of the collagen networks. While it was still possible to link some variations in the **FOS** parameters directly to certain visual differences between the images, we found that it is much harder to do the same kind of comparison with the **GLCM** parameters. As a result, we did not attempt to interpret the direct correlation between the **GLCM** parameters and the visual presentation of the original images.

Finally, additional tests were also performed to evaluate the effectiveness of the proposed methodology for classification across data sets (atherosclerosis vs. infarcted heart). All images acquired from the arteries (all five groups) and from infarcted hearts (**ASC**s-treated and un-treated) were included for analysis.

Collagen images collected from artery could be confidently differentiated from those collected from infarcted hearts with 99% accuracy when all texture parameters (**FOS**+**GLCM**) were used for classification. Accuracy dropped to 81% when considering only **FOS** parameters, and 96% when considering only **GLCM** parameters. Figure 7.8 compares each texture parameters calculated for images acquired from atherosclerotic arteries and infarcted myocardium. The obtained ROC curve is presented in Fig. 7.9 for each test set.

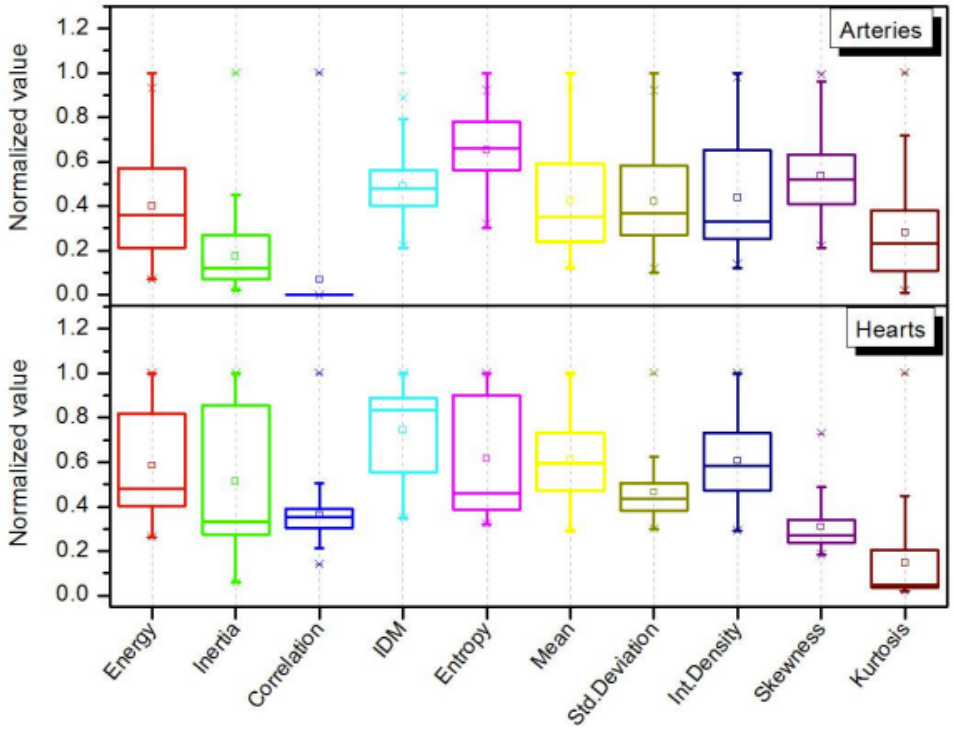


**Figure 7.8:** Comparison of each texture parameter calculated for images acquired from atherosclerotic arteries and myocardium infarcted hearts. The top and bottom of each rectangular box denote the 75th and 25th percentiles,respectively, with the median shown inside the box. Vertical bars extending from each box represent the 90th and 10th percentiles. *Reprinted with permission from Mostaço-Guidolin, Leila B., et al."Collagen morphology and texture analysis: from statistics to classification.", Scientific reports 3 (2013) [20]. Copyright 2013 Nature Publishing Group.*

Although it was cast as a binary classification problem, individual groups in this test in fact contained much more diversity compared to those presented in the case of the infarcted hearts.

With such high level of image inhomogeneity, we were able to obtain a very high classification accuracy using combined **FOS/GLCM** parameters, or **GLCM** alone, respectively. However, the **FOS** texture parameters alone delivered a modest result. Once again we have shown that our methodology is robust in distinguishing structural variations present in collagen network, whether it is for intra- or inter-data set comparison. Secondly, we also proved that this type of collagen feature classification benefits from using a combined **FOS/GLCM** model.

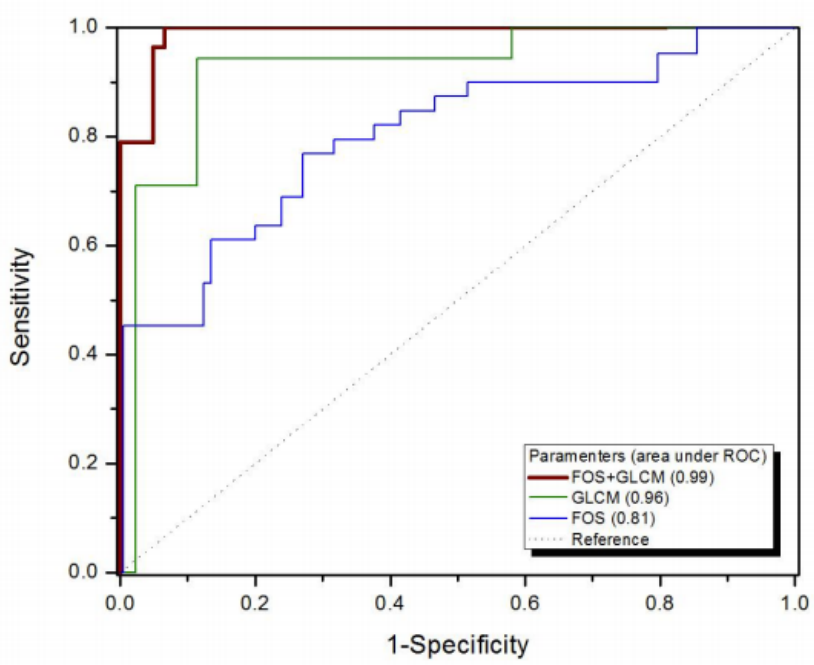


**Figure 7.9:** - ROC curves for all three texture sets tested: **FOS**, **GLCM** and **FOS+GLCM**. Values suggest that the classification across data sets has a good predictive value, as the area under the ROC curve was 0.99 for all texture parameters (**FOS+GLCM**), 0.81 for **FOS** parameters and 0.96 for **GLCM** parameters. *Reprinted with permission from Mostaço-Guidolin, Leila B., et al."Collagen morphology and texture analysis: from statistics to classification.", Scientific reports 3 (2013) [20]. Copyright 2013 Nature Publishing Group.*

In summary, using two disease models we have demonstrated the feasibility of performing classification of collagen fibril morphology based on first-order and second-order texture statistical parameters derived from **SHG** images. Using a nonlinear **SVM** classifier, it was shown that in more complex cases, the classification accuracy can be improved with combined **FOS** and **GLCM** texture variables, compared to the case when either one is used.

In a binary classification of ASCs-treated and un-treated infarcted hearts, one group of texture parameters was sufficient to generate classification accuracy of better than 90%. However, when comparing collagen morphology observed in two different data sets (artery vs. heart), the combined **FOS/GLCM** model is superior to the model that uses individual group textures (**FOS** or **GLCM**).

Although the results presented in this chapter are only a proof-of-concept with a limited sample size, its implication is that non-subjective texture based classification of

**SHG** images could have practical clinical applications in distinguishing collagen pathologies. In the clinical world where digital pathology is becoming more popular, automatic classification could be a very helpful tool for the pathologist to increase sample throughput and to help minimize interpretation errors.

# Chapter 8

# Statistical, textural and structural analysis of CARS images to classify lipid-rich structures

Lipid deposition is commonly present in several pathological conditions and biological processes, such as inflammatory responses to stem cell development. In arterial diseases dysfunctional lipid metabolism plays an important role in the pathogenesis of atherosclerosis [50, 51].

Recently, **CARS** microscopy has been established as a promising optical technique in medicine, mainly due to its specific power in lipid imaging. The detected morphological changes in tissue lipids could be strongly associated with important biological functions or disease progressions.

In this study, textural features from images acquired by **CARS** microscopy were extracted and then used to differentiate and to classify lipid-rich structures for its morphology and its correlation with the disease stage.

In addition, specific characteristics in lipid-rich objects inherent to particle-like structures were also defined, calculated and used as complementary features for image classification. The methodology presented was not only capable of quantifying changes in lipid accumulation caused by atherosclerosis, but can also be easily applied to other

pathological evaluations.

## 8.1 Lipid accumulation within the vessel walls

A total of 508 **CARS** images acquired from 21 rabbits were used in this analysis. Based on textural and morphological characteristics such as shape, size and organization, images were divided into 4 distinct groups defined by age. Group A (or "young") was composed from 121 images acquired from rabbits between 2 and 4 month of age. Group B (or "middle I") was composed from 110 images from rabbits aged between 6 to 12 month-old. Finally, groups C and D (or "old") were composed from 135 and 142 images acquired from rabbits aged between 14 to 16 month-old and 18-27 month-old, respectively. Figure 8.1 shows examples of lipids images seen in each of these groups.

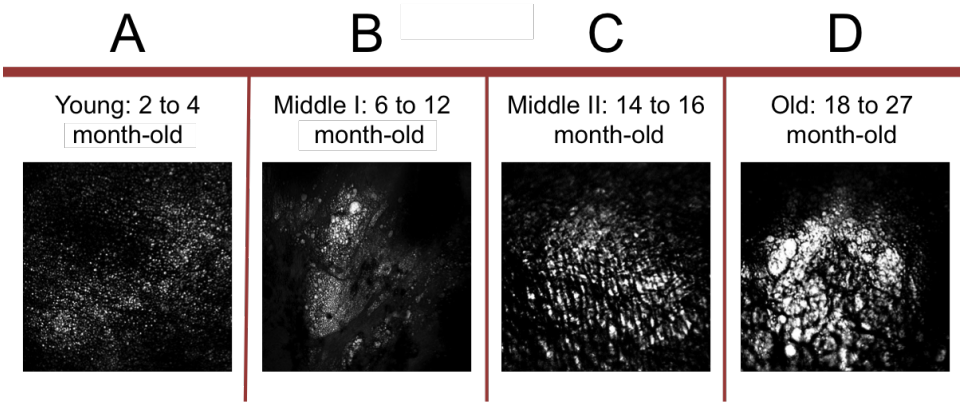


**Figure 8.1:** All **CARS** images acquired from the arteriosclerotic aortic segments of the **WHHLMI** rabbits were classified into four groups A–D, according to the rabbits'age. Each group of the images has its own characteristic morphological features such as shape, size and organization. Images are showing lipid-rich structures, accumulated inside of the necrotic core. *(© L.Mostaço-Guidolin, 2014)*

Five **FOS** parameters (mean, standard deviation, integrated density, kurtosis, and skewness) were calculated for all 508 images. The distributions of these **FOS** values corresponding to each group are illustrated in Fig. 8.2.

From group A to D, a general elevating trend is noticeable in three parameters: mean, standard deviation, and integrated density. With the exception of group A, the values obtained for groups B, C and D are statistically compatible. The increase in the values is associated with higher accumulation of lipids as the rabbits age increases. The lesions

found in middle and old animals are known to be more severe than the ones normally found in younger subjects.

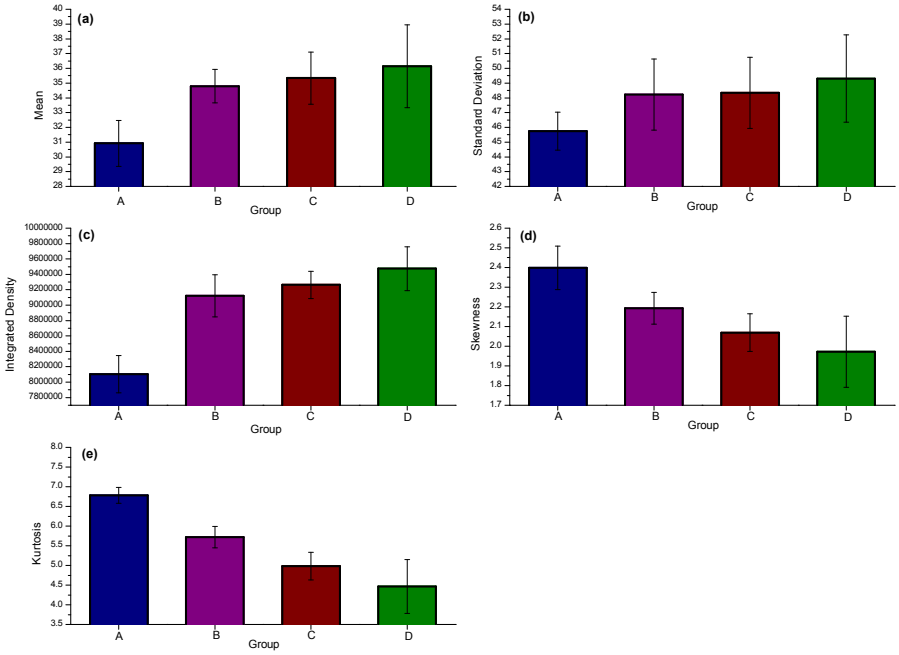


**Figure 8.2:** Values of **FOS** texture parameters calculated from each group. Group A: 2-4month-old; group B: 6-12 month-old; group C: 14-16 month-old; group D: 18-27 month-old. *(© L.Mostaço-Guidolin, 2014)*

The distribution of skewness and kurtosis values of the gray level intensity histograms are also illustrated in Fig. 8.2. The skewness indicates the imbalance between the extent of the areas (or number of pixels) that are darker or brighter than the mean.

Group A images display higher skewness than the other groups. While skewness is a measure of asymmetry of a distribution relative to the mean value, the kurtosis describes whether gray tones are more distributed (flat) or concentrated around the mean (peaked). Since the lipid-rich structures observed in images acquired from advanced plaques (group D, for example) are bigger, cover larger area and generate stronger **CARS** signal with a more spread-out pixel intensities distribution, they result in lower kurtosis value.

Additionally, five co-occurrence gray level matrix (**GLCM**) parameters, were also extracted from the images. They are: inverse difference moment (**IDM**), energy, inertia, entropy and correlation. It is interesting to notice that most of the parameters (with the exception of the "energy") present statistically compatible values when comparing all 4

groups.

**GLCM** parameters consider every pixel and its neighborhood, generating a map that is able to account for more complex structures in the images. Each of these features bring different information when used as a base to perform classification analysis. All **GLCM** values are presented in Fig. 8.3.

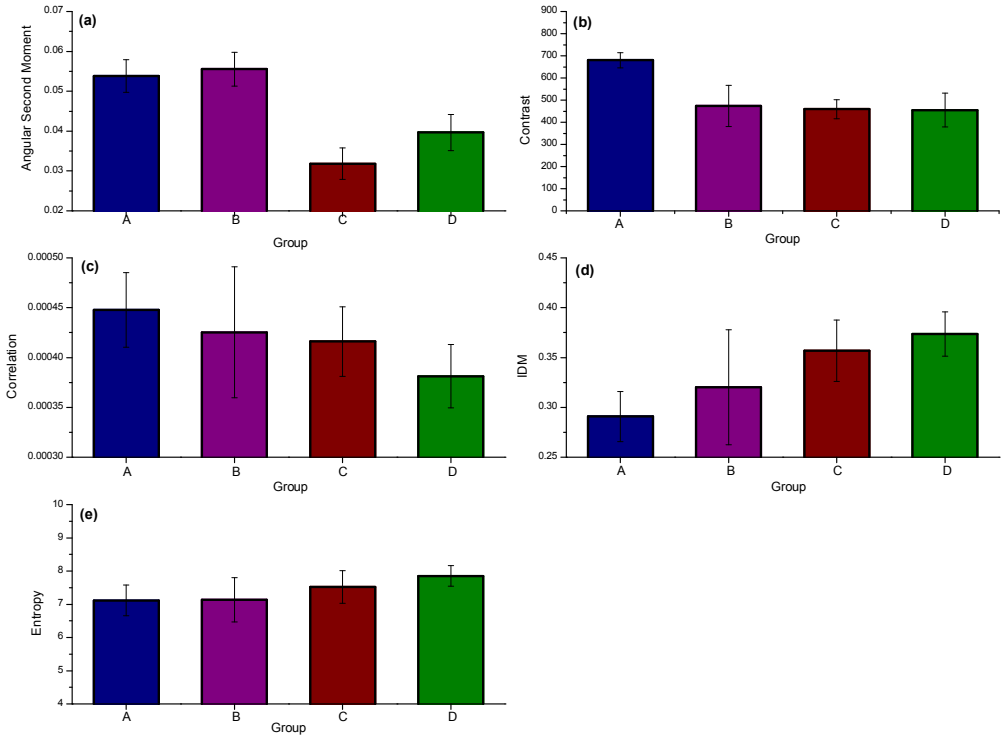


**Figure 8.3:** Values of GLCM texture parameters calculated from each group. Group A: 2-4month-old; group B: 6-12 month-old; group C: 14-16 month-old; group D: 18-27 month-old. *(© L.Mostaço-Guidolin, 2014)*

In order to improve the classification accuracy, besides texture analysis, all **CARS** images were also subjected to additional particle-features analyses to extract information more specific to the round-shaped observed structures.

Figure 8.4a shows the average values of the number of objects identified per group of images. Figure 8.4b and Fig. 8.4c show the average Feret diameter and aspect ratio of the identified particles in all images for each group.

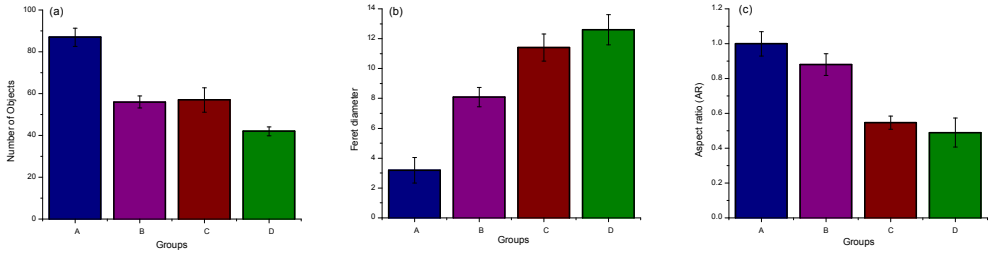


**Figure 8.4:** Average (a) number of objects identified per group; (b) Feret diameter of particles; (c) Average aspect ratio (AR) for each age group. Group A: 2-4month-old; group B: 6-12 month-old; group C: 14-16 month-old; group D: 18-27 month-old. *(© L.Mostaço-Guidolin, 2014)*

By different sets of features, a nonlinear **SVM** classification was performed on all **CARS** images. As expected, when combining all available features (texture parameters and particle-specific information) the overall accuracy is the highest, at over 80% in all cases. When comparing the performance of the classification by using only particle-specific features with that by using textural features, it is noticeable that particle-specific features edge out slightly. This result is probably due to the fact that these particle-related features are capturing information specifically related to the shape of most of the lipid-rich structures.

Although textural features are also able to retrieve information regarding the distribution of certain pixel values and its neighbours; however, as mostly of the **CARS** images are showing the presence of round-shaped structures, the diameter and how circular they are became more important when characterizing such images.

In Table 8.1, classification accuracies were summarized for all tested scenarios. It is interesting to notice that **FOS** features generally present a higher overall accuracy when compared to **GLCM** and even **FOS+GLCM** features.

| Parameters | Group A | Group B | Group C | Group D | Overall |
|---|---|---|---|---|---|
| FOS | 81% | 72% | 70% | 80% | 79% |
| GLCM | 60% | 61% | 67% | 67% | 52% |
| FOS+GLCM | 78% | 58% | 73% | 70% | 69% |
| Particles | 90% | 78% | 81% | 80% | 79% |
| Particles+Texture | 95% | 88% | 81% | 81% | 82% |

**Table 8.1:** Summary of the nonlinear **SVM** classification percentual accuracy for **CARS** images acquired from atherosclerotic arteries based on a 4 group model, based on the age of the rabbits. Group A (young): 2-4month-old; group B (middle I): 6-12 month-old; group C (middle II): 14-16 month-old; group D (old): 18-27 month-old.

Earlier it was demonstrated that **GLCM** features were more accurate for classifying **SHG** images (collagen fibrils) than **FOS** features. However, in this case, **FOS** stands out as the best or even when compared to combined **FOS** and **GLCM**.

After analyzing the distribution of all textural features measured from **CARS** images, it is noticeable that they follow a Gaussian distribution. The distributions previously observed for **SHG** images were characterized by the lack of symmetry and did not present a normal behaviour, making the distinction between groups easier than when a Gaussian distribution is used. In the case of **CARS** images, the values are approximately equally distributed around the mean when using **GLCM** parameters or a combination of **GLCM** with **FOS** to classify **CARS** images, they are therefore contributing to increasing the errors instead of improving the accuracy.

The ineffective classification for particle-like objects provided by glsFOS+**GLCM** texture suggests that this type of texture analysis maybe more efficient in evaluating fiber-like dimensions, such as the case in collagen imaging.

## 8.2 Lipid morphology

Besides classification based on age (lesion severity), we are also interested in how well the classification performs primarily based on lipid morphology only. In Fig. 8.5, examples show how these **CARS** images were ensembled in to three different groups, with specific morphological features associated with each group.

For this analysis, the groups were defined exclusively based on morphological charac-

teristics, not the age of the rabbits. Group A is characterized by the presence of primarily small lipids droplets, characteristic of young plaque developments. Group B include images acquired from more advanced lesions, showing larger lipid-rich structures. Group C is composed of images lacking well-defined structures, and with mixed advanced/early lesions.

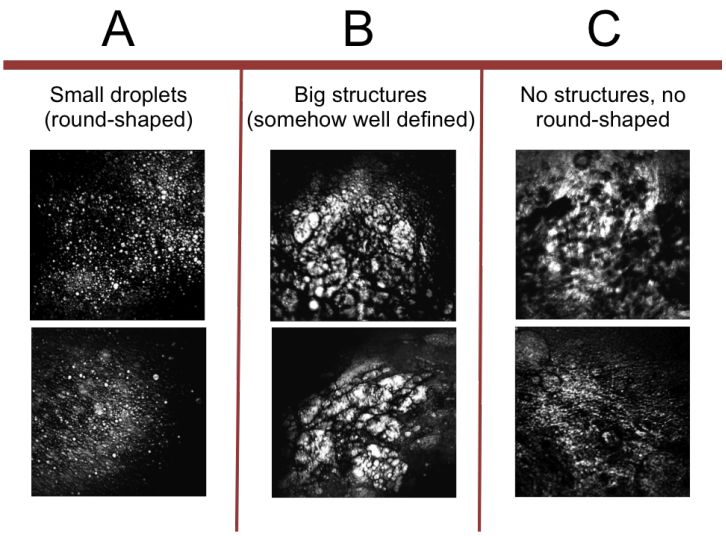


**Figure 8.5:** CARS images, grouped according to morphological characteristics of lipid-rich structures deposited on the arterial wall. *(© L.Mostaço-Guidolin, 2014)*

In this test, the classification was also carried out with texture parameters, particle-specific features and the combination of both. Results are shown in Table 8.2 shows the classification results using only textural parameters, particle features and a combined approach. When information regarding the particles dimensions, density, diameter, and circularity were added, a higher classification accuracy, sensitivity and specificity was achieved.

Similar to previously reported, lipid morphology classification performed the best when a combined texture + particles matrix is used.

| Parameters | Accuracy | Sensitivity | Specificity |
|---|---|---|---|
| FOS | 70% | 73% | 77% |
| GLCM | 56% | 54% | 55% |
| FOS+GLCM | 77% | 76% | 73% |
| Particles | 82% | 79% | 83% |
| Particles+Texture | 93% | 95% | 95% |

**Table 8.2:** Overall classification results obtained for **CARS** images separated considering exclusively the morphology of the lipid-rich structures. The age factor was not included in this analysis. Group A (young): 2-4month-old; group B (middle I): 6-12 month-old; group C (middle II): 14-16 month-old; group D (old): 18-27 month-old.

Considering these results, we believe that similar analysis can enable better objective extraction, quantification and classification of structural and biochemical changes associated with different pathological conditions.

# Chapter 9

# TPEF images: the challenge of analyzing the elastic layer disruption

Fluorescence microscopy has been widely used in the characterization of many biological compounds. It is a popular tool for live-cell imaging, tissue characterization and *in-vivo* studies.

In recent years, as the trend in biology has moved more and more towards high-throughput applications, there has been an explosion in the amount of data being acquired and analyzed using this technique. There is, however, a bottleneck: in most cases, the analysis is still based on visual inspection. It is time-consuming, subjective, and not reproducible.

Elastin as a member of the extra-cellular matrix (**ECM**) protein family is the major source of elasticity in the vasculature. Elastin has been found in many tissues, such as the aorta and carotid arteries, lungs, tendons, skin, and microvessels. The quantities of elastin vary greatly between tissues such as more than 50% in large arteries or as little as 2-4% of the dry weight of skin [177].

In arteries, elastin contributes to the overall vessel composition and arteriolar distensibility. After longitudinal vessel lengthening, elastin is primarily responsible for bringing the vessel back to its resting state [178]. Being a highly cross-linked structure, the protein is insoluble, extremely hydrophobic, long lived, and resilient to stretch.

While elastin and elastic fibers are not the same, elastin composes 90% of the elastic fiber with the remaining constituents being fibrillins and microfibrillar-associated glycoproteins [179]. An important property of stretch, the elasticity allows for significant deformation followed by recoil without requiring energy input for recoil.

In healthy individuals, elastin is a stable, insoluble, and resilient protein. However, there are many pathological states that cause ECM remodeling and degradation of elastin, such as aging, hypertension, and plaque development [180].

As previously discussed in section 2.1, the wall of blood vessels consists of three layers: the intima, the media, and the adventitia. Capillaries, which have only an intimal layer of endothelial cells resting on a basal lamina, are the exception. Regardless of the organization of layers, one can distinguish four building blocks that make up the vascular wall: endothelial cells, elastic fibers, collagen fibers, and smooth muscle cells.

Elastic fibers are a rubber-like material that accounts for most of the stretch of vessels at normal pressures as well as the stretch of other tissues (e.g., lungs). Elastic fibers have two components: a core of elastin and a covering of microfibrils. The elastin core consists of a highly insoluble polymer of elastin, a protein rich in non-polar amino acids (i.e., glycine, alanine, valine, proline).

After being secreted into the extracellular space, the elastin molecules remain in a random-coil configuration. They covalently cross-link and assemble into a highly elastic network of fibers, capable of stretching more than 100% under physiological conditions.

The microfibrils, which are composed of glycoproteins and have a diameter of approximately $10nm$, are similar to those found in the extracellular matrix in other tissues. In arteries, elastic fibers are arranged as concentric, cylindrical lamellae. A network of elastic fibers is abundant everywhere except in the true capillaries, in the venules, and in the aforementioned arteriovenous anastomoses.

A healthy artery or very early lesion has a thin intima composed mainly of a single layer of endothelial cells. Beneath this, the media is composed mostly of elastin, which has a broad emission band between 450 and $600nm$ with a peak around $490nm$. As age increases, this layer becomes thicker and the vessel starts to loose its contractile

properties.

In this section, we tested the tools developed earlier to analyze the **TPEF** images acquired from arterial tissue. The objective here is to investigate the potential of fractal and directional analysis to track changes observed during atherosclerosis development.

## 9.1 Fractal dimension: quantifying elastic fibers disruption

Characterization of elastic fibers is a more complex problem, compared to collagen, due to such irregular surfaces observed in the images. Considering such a challenge, the fractal dimension turns out to be an interesting alternative to extract objective parameters from such images.

Different from the topological dimension, the fractal dimension is a fractionary number that describes how irregular an object is and how much of the space it occupies. It is a measure of how fragmented an object is, and it may be understood as a characterization of its self-similarity.

Before extracting the fractal dimension of each image, the segmentation of fiber-like structures from **TPEF** images was performed, using a Hessian-based *tubeness* filter [26].

This filter determines how "tube-like" a pixel is by convolving the image with a spherical Gaussian kernel with standard deviation $\alpha$, computing the Hessian matrix at each pixel, and computing a "tubeness" metric from the Hessian eigenvalues The sensitivity of the "tubeness" filter to tubular structures of varying radii can be tuned by varying $\alpha$. The effect of the tubeness filter on **TPEF** images is shown in Fig. 9.1.

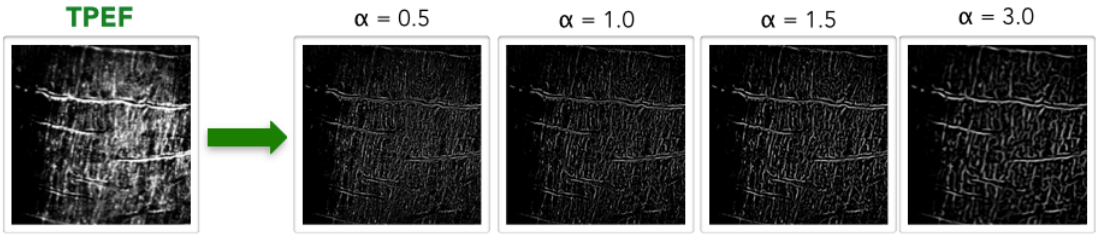


**Figure 9.1:** Effect of the tubeness filter on the processed **TPEF** image of elastic layer on artery. As the value of $\alpha$ increases, only thicker tubes are detected. *(© L.Mostaço-Guidolin, 2014)*

The choice of $\alpha$ is important and must be tailored accordingly to the application in question. Some qualitative tests were performed and $\alpha$=1.0 seems to be the best for analyzing elastic fibers in the arteries. Using higher values, result in loss of information, as some minor structures are ignored. On the other hand, smaller values of $\alpha$, leads to over-definition. More details about the theory behind this filter can be found in Appendix B.

## 9.2 Aging and its effect on elastic properties of blood vessels

In Fig. 9.2, examples of **TPEF** images are presented showing the aorta internal elastic layer (**IEL**) and some smooth muscle cells of rabbits with different ages. They were taken from the luminal surface all the way down to the **IEL**, around 40-45$\mu$m).

In total, 115 images were analyzed; 38 from group A, 36 from group B, 23 from group D, and 18 from group D. Images acquired from a newborn show very thin fiber-like structures, somehow disorganized. As the rabbit's age increases, the elastic layer develops as shown in Fig. 9.2[B1-B5]. The fibers become clearly defined, and thicker than those at younger ages.

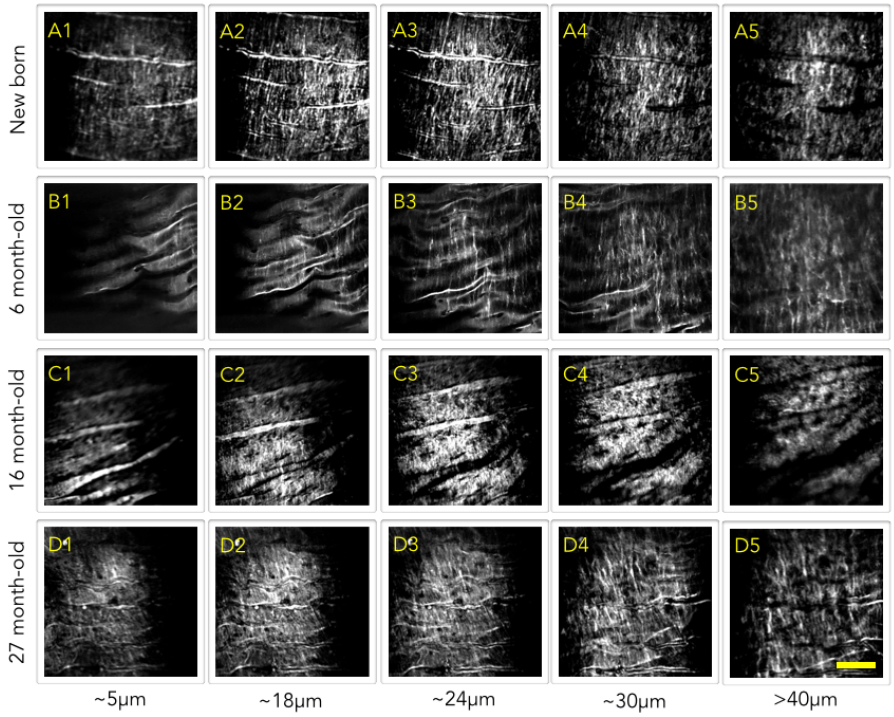


**Figure 9.2:** Examples of **TPEF** images acquired from the healthy lumen along the aorta of WHHL rabbits. Images were classified into four groups A–D, according to the rabbits' age. Each group of the images has its own characteristic morphological features such as shape, density and organization. Images are showing the external elastic layer. *Scale bar: 50µm (© L.Mostaço-Guidolin, 2014)*

With aging, important changes occur in the elastic properties of blood vessels, primarily arteries. The compliance of the aorta first rises during the growth and development to early adulthood and then falls during a later life. After early adulthood, unfavorable changes occur. For example, atherosclerotic changes reduce the vessel's compliance, because of the progressive, diffuse fibrosis of vessel walls with age, and because of an increase in the amount of collagen [181]. Some of these changes can be noticed by comparing images shown in Fig. 9.2B1-B5 with those shown in C1-C5.

Finally, denser accumulation of structures aligned with the loss of fiber organization can be noticed in Fig. 9.2D1-D5, where images represent a 27 month-old rabbit.

Changes related to aging can be tracked by fractal dimension analysis of **TPEF** images. In the case of healthy artery, the fractal dimension changes as the elastic fibers start to degrade due to aging. It potentially is also due to the development of atherosclerotic lesions along the aorta. The results are shown in Fig. 9.3.

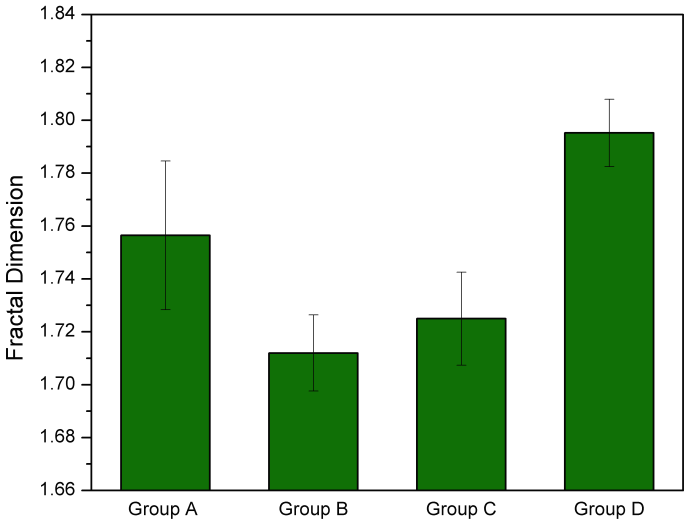


**Figure 9.3:** Fractal dimension for **TPEF** images acquired in healthy regions along the aorta artery. Each bar represents the average fractal dimension value (and its standard deviation) for rabbits within certain age groups. Group A: 0-4 month-old; group B: 6-12 month-old; group C: 14-16 month-old; group D: 18-27 month-old. *(© L.Mostaço-Guidolin, 2014)*

Group A, in which images are from the young animals (ages ranging from 0 to 4 month-old), was characterized by a fractal dimension higher than that obtained for group B. Group B (composed by animals aged between 6 and 12 month-old) has shown the lowest values among all groups.

As shown in Fig. 9.2, images from group B can be associated with regions where the elastic fbers are fully developed and not affected yet by serious plaque development nearby. Groups C and D (animals with ages between 14-to 16 month-old and 18 to 27 month-old, respectively) show higher fractal dimensions than group B. This fact might be correlated with the disruption of elastin as well with more aggressive accumulation of fibers.

Interestingly, group A presents fractal dimensions almost as high as the ones obtained for group D, considering the significant age difference. Before getting to the stage where the **IEL** is mature and presenting well defined fibers, elastin seems to be more accumulated following a similar pattern to that is observed from older animals.

## 9.3 Vascular remodeling and blood flow

Vascular remodeling of elastin content throughout the vessel wall has been shown in both healthy physiological and pathological states [182]. As flow is gradually increased in normal, adult rabbit carotid arteries, the lumen diameter increases as well as **IEL** fenestra size [180, 182].

Examination of the **IEL** has shown that although the thickness and fenestra density do not change, fenestra area decreases significantly [183]. Both **IEL** thickness and fenestra area variations could be attributed to changes in the mechanical environment and cellular function. Decreases in **IEL** thickness and fenestra area are often associated with elastin reorganization and elastin degradation.

As discussed previously in section 2.1.2, certain locations along the aorta are more prone to plaque development than others. At these locations the rate and pattern of blood flow are altered thus affecting local hemodymanics. As a result, changes in plaque development were observed. As presented in Fig. 9.4, the elastic layer suffers from changes in blood flow.

When combining **TPEF** and fractal dimension analysis, it is possible to track the **IEL** differences along the aorta. As shown in Fig. 9.4, images acquired along the aorta arch (**AA**) region show that vessel is elastic layer presents distinct pattern. This observation was also reveled by earlier analysis (section 4.2).

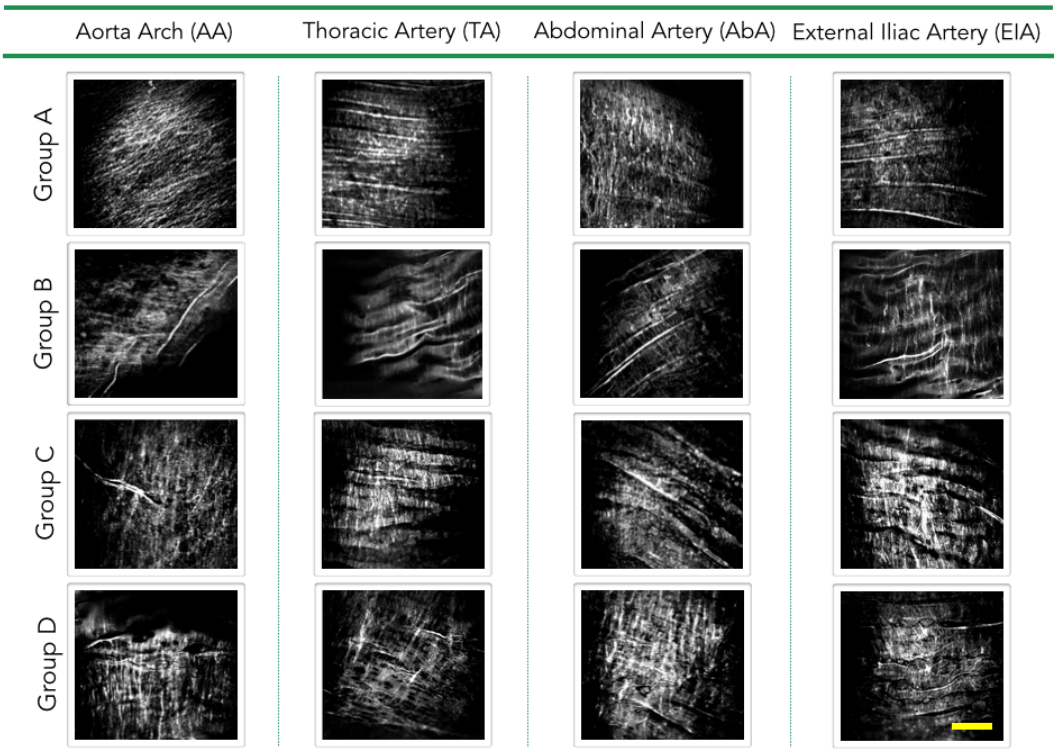


**Figure 9.4:** Examples of **TPEF** images from different locations along the aorta. The corresponding aorta segment is illustrated on top of each column. Images from different age groups show degradation of the vessel's elastic layer. Group A: 0-4 month-old; group B: 6-12 month-old; group C: 14-16 month-old; group D: 18-27 month-old. *Scale bar: 50µm (© L.Mostaço-Guidolin, 2014)*

From Fig. 9.5 we can see that fractal dimension values were the highest in **AA**, followed by the abdominal artery region (**AbA**). This region has also been targeted as critical location regarding plaque development (section 4.2).

The thoracic and external iliac arteries (**TA** and **EIA**, respectively) have shown lower fractal dimensions. Such difference in fractal dimension can be explained by the fact that these regions present less turbulent blood flow, even when plaque starts to develop. The original shape of the elastic layer present less alteration in these regions than in the **AA** and **AbA** locations.

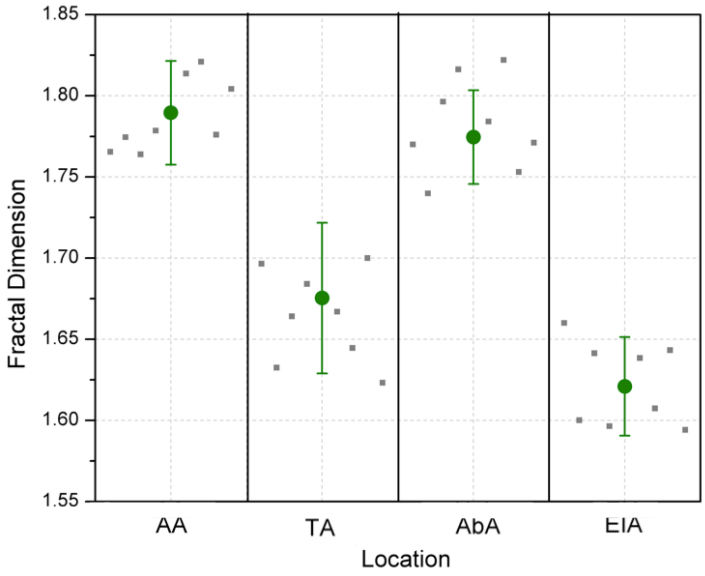


**Figure 9.5:** Fractal dimension values obtained from **TPEF** images acquired from different locations along the aorta. The big green circles represent the overall average value (and its standard deviation) for each region. The smaller gray squares represent the average fractal dimension values obtained for each individual rabbit. The standard deviation for individual values were omitted to enhance the graphic clarity. **AA**: aorta arch; **TA**: thoracic artery; **AbA**: abdominal artery; **EIA**: external iliac artery. *(© L.Mostaço-Guidolin, 2014)*

From these results we can conclude that fractal dimension analysis is good at tracking disruptions observed along the aorta **IEL**. Even more importantly, it might also be a good image parameter to track changes in collagen fibers.

## 9.4 Fibers directionality

Another aspect of fibers that can be evaluated is its orientation. Oriented linear patterns are common phenomena in nature and are an important class in image analysis.

The method used in this section to analyze **TPEF** images aimed to infer the preferred orientation of structures present in the input image. It computes a histogram indicating the amount of structures in a given direction. Images with completely isotropic content are expected to give a flat histogram, whereas images in which there is a preferred orientation are expected to give a histogram with a peak for that orientation.

For example, in the Fig. 9.6 two images containing different arrangements are shown. In Fig. 9.6(a), the structures observed in a banana leaf closeup are very well oriented

and the vast majority of structures are concentrated at about 50 degrees (depending on imaging orientation).

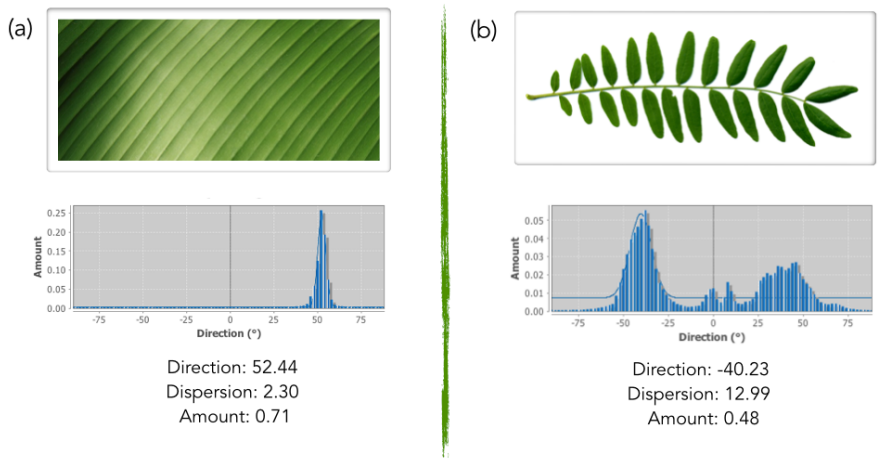


**Figure 9.6:** (a) Closeup showing details of a banana tree leaf. Very well oriented structures can be seen; (b) Multiple and well oriented leaves are characterized by the presence of two peaks, as shown in the histogram. The statistics generated is based on the highest peak found.

On the other hand, the leaf shown in Fig. 9.6(b), demonstrates 2 major orientation populations, one with a preferred orientation at about 40 degrees, and another one with preferred orientation at around -40 degrees. This is well detected by the method, which reports two main peaks in directionality histogram. In addition, a minor peak can also be seen around 0 degrees, reporting the orientation of the main branch.

Angles are reported in their common mathematical sense. That is: 0 degree is the East direction, and the orientation is counterclockwise.

In Fig. 9.7 some of the **TPEF** images are shown along with their directionality histograms. One can notice that as the fiber structure changes, the orientation of the fibers also changes.

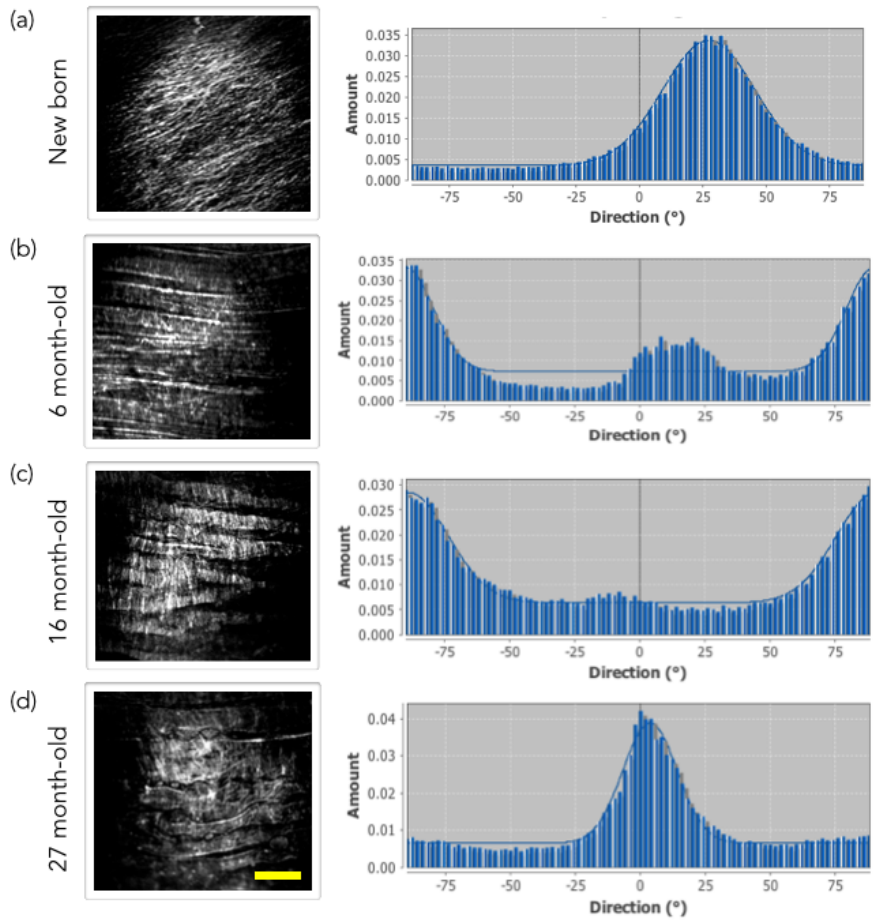


**Figure 9.7: TPEF** images of healthy arterial regions from rabbits. Image (a) is from a newborn rabbit; (b) from a 6 month-old; (c) from a 16 month-old; and (d) from a 27 month old. As the fibers are remodeled, their orientation changes. *Scale bar: 50µm*

Table 9.1 shows the average directionality values obtained for all **TPEF** images assembled according to rabbit's age.

Young healthy arteries are characterized by the presence of fibers which still under development and maturation. The distribution of elastic fibers is centered around 25 degrees, with approximately 13 degrees of dispersion. Almost 90% of the total amount of elastic fibers identifies in **TPEF** images are oriented in that direction.

| | Group A | Group B | Group C | Group D |
|---|---|---|---|---|
| Direction (°) | 25.64 | 80.91 | 78.01 | 6.54 |
| Dispersion (°) | 13.26 | 7.83 | 16.67 | 4.40 |
| Amount (%) | 89.92 | 39.67 | 48.93 | 87.33 |

**Table 9.1:** Overall directional distribution of fibers, according to the rabbit's age. Groups A and D were characterized by the presence of one central peak; groups B and C show the presence of two main peaks, with almost 50% of all fibers oriented in certain angles.

As the rabbits' age increases, significant change in the fiber orientation was detected. When more prominent horizontal structures appear, a delimiting of the fibre also begins to appear. Vertical small fibrils can be found filling the spaces in between the horizontal main fibers. The distribution of these small fibrils is detected and shown as two main peaks located closer to the extremities of the histogram scale. This is shown, for example, in Fig. 9.7(b) and (c). One interesting observation is that older animals present segments with a narrower and well centered directional distribution when compared to younger groups.

This section of analysis suggests that the directional analysis of fiber distribution can bring another aspect of information to the task of characterizing biological samples. In same cases, it can be a simple approach, but enough to reveal significant changes. When it is combined with other methods, directional analysis can be a powerful tool to classify images from different sources.

# Chapter 10

# Conclusions & future work

The studies of this research thesis have involved a novel biomedical application of nonlinear optical microscopy, as well as the development of a novel set of tools to interpret captured information. Multimodal NLO microscopy is a powerful imaging technique that can be used to visualize extracellular components such as collagen, elastin, and lipids; all of which are the major biochemical constituents in atherosclerotic plaque development.

Atherosclerotic plaques are complex systems, and the composition and structure of them vary greatly with respect to age, location along and within the vessel. Rapid determination of the spatial distribution of these components and in a manner that is consistent with conventional microscopy makes **NLO** microscopy a potential adjunct or even a substitute to routine histopathology.

One, among several other attractive features of **NLO** microscopy, is the ability to use optical sectioning to examine bulk tissue without the need for sectioning and staining of the tissue.

We have shown that by using the wealth of knowledge gained from important empirical image-based studies, we can use multimodal **NLO** microscopy to characterize complex tissue assemblies such as regions stricken by atherosclerotic plaques. We have observed that healthy and plaque regions can be easily distinguished by **NLO** microscopy, as they are marked by different features arising from the accumulation and reassembling of specific biological compounds.

The challenge of this thesis' research was to determine whether **NLO** microscopy can be used to distinguish among plaque's severity levels. In addition, key aspects of this study were the development, application, and testing of quantitative tools able to extract unique features from **NLO** images. As a result, this research helped to extend **NLO** microscopy beyond the use only as a qualitative tool for simple visualization of biological tissue and cells.

In this thesis I have presented my *in-house* developed intensity-based parameter for plaque burden. This new optical index for plaque burden (**NLO** OIPB) was defined using **NLO** images acquired from *ex-vivo* samples of un-sectioned bulk rabbit arterial tissue. The OIPB index showed a strong correlation with the age of the studied **WHHLMI** rabbits and the severity of the atherosclerotic lesions in the rabbits. Through this index I could also confirm critical locations for plaque accumulation along the vessel.

In order to validate the results obtained by the OIPB, experiments based on immunohistochemistry (**IHC**) were also performed. As the atherosclerosis development can be accurately associated to the increasing inflammatory receptors. A specific antibody type (**ICAM-1**) was used as a marker to track regions where plaques accumulated along the aorta.

Results from **OIPB** and **IHC** showed a good correlation, validating the **OIPB**'s strength for tracking plaque development solely based on **NLO** images.

Besides the **OIPB**, results based on the analysis of textural parameters extracted from the **NLO** images were also presented. Texture parameters provided quantitative descriptors that could be linked to specific structural and compositional motifs that characterize different stages of atherosclerotic plaques.

Up to this point, the use of objective and quantitative tools to extract information from **NLO** images was still in its early stages, and our work was one of the pioneers in exploring this new avenue.

As a conclusion of the first part of this thesis, promising results related to the potential of using the **OIPB** and texture analysis for plaque classification were presented. These results suggest that the methods developed in this study could be very valuable for

assessing the disease progression, once **NLO** microscopy becomes available for *in-vivo* applications.

Considering that the success of plaque burden assessment achieved by using the **OIPB** and texture analysis, some other questions may arise from this study. For example, can we develop a set of parameters which are able to extract reliable quantitative information from images acquired by each **NLO** technique? Are these methods robust enough to be used in applications other than the characterization of atherosclerotic plaques?

We tried to answer these questions in the second half of this thesis. Keeping in mind that changes collagen distribution, elastin disruption and lipid accumulation are very important aspects to be analyzed in several biomedical studies, the idea of extracting specific information from **TPEF**, **CARS** and **SHG** images represented a challenge worth of trying.

The second part of this thesis was dedicated to discussion of methods that were applied for the first time to the characterization of the **NLO** images.

Sets of images acquired from arterial samples were used once again for evaluation of these methods; however, the main focus of each chapter presented in the second pat of this thesis was to test the capability of each method for classifying **NLO** images, based on several pre-defined objective parameters.

Changes in collagen fiber orientation and lipid accumulation in the aorta wall, as well as changes in their spatial distribution and patterning were quantified by textural features. Most notably, many of the first and second order tonal-texture parameters showed distinctly different depth profiles between the images from young and older specimens that can be rationalized in terms of the differences in the composition and structure of the lesions along their developmental path.

These results show that tonal-texture parameters offer objective and useful metrics to quantify vessel wall pathology associated with plaque development. Texture parameters were shown to be particularly powerful for classifying **SHG** images, or collagen changes.

In addition to texture parameters, several other features were extracted from **CARS**

images. Most of the lipid-rich structures found in arteries are round-shaped objects. Parameters such as the Feret diameter, density of objects found in each image and the aspect ratio of each structure were quantified and used as additional features in the classification of **CARS** images.

Finally, **TPEF** images - or elastin changes from healthy arterial regions - were successfully characterized by texture analysis and some other parameters. Fractal analysis and the directionality of the elastic fibers were shown to be very useful in characterizing elastin layer degradation. These two parameters might also be useful in evaluating collagen as they can successful track changes related to fiber-like structures.

In conclusion, we have presented a multidisciplinary approach to tissue characterization and a new perspective of the multimodal nonlinear optical microscopy to investigate pathological conditions. With a better understanding of the specific signatures imaged by each **NLO** technique, we proposed several imaging analysis tools to extract objective image parameters that have high potential for disease diagnosis. These studies are the dawning of a new era for the applications of **NLO** microscopy, and more importantly, the bridging of the wealth of knowledge in the various disciplines of optics, imaging processing, biochemistry and medicine.

## 10.1 Future work

**NLO** microscopy is already established as a powerful tool for rapid imaging of biological tissue. The main outcome of this study was a sound methodology to accurately extract diagnostically relevant information from those images. Progress to that end has helped to propel this technique toward future clinical adoption in critical care, by correlating the disease burden to image features. This thesis research is also a stepping stone toward broader applications of **NLO** microscopy in the clinical environment.

However, **NLO** microscopy is still a bit far from becoming a *"viable tool"* for biomedical applications. Several aspects can be improved in order to achieve more specific and even more complete results. Some suggestions of possible future work are presented in the

following sections: hardware & instrumentation, data analysis, and biomedical-specific aspects.

### 10.1.1 Hardware & instrumentation

Three-dimensional volume imaging is now an essential tool in biological and other areas. Multiphoton scanning microscopy accomplishes this by scanning a point source through the sample volume, collecting the resulting signal, and re-creating the image. The resolution has a high dependence on the point-spread function (**PSF**) of the scanned point source.

Refractive-index mismatches between the immersion media of high-NA objectives and the sample, the usually non-uniform samples themselves, off-axis transmission through optical component, such as the objective and scan lenses while scanning, and imperfections in the optical elements throughout the optical path impart aberrations to the wavefront and contribute to a deterioration of the **PSF**.

Incorporation and testing of an adaptive optics system is a very important improvement that can be performed, aiming to increase the image quality, and consequently, the power in tracking smaller and earlier changes in biological samples.

Another important improvement that could be considered, more specifically in **CARS**, is the addition of pulse chirping to the current system. In order to achieve variable pulse length, it is necessary to make use of a technique known as spectral focussing. Starting with short femtosecond (fs) pulses, the pulses are streched in time (or, in other words, chirp the pulses).

By carefully choosing the dispersion in both the pump and Stokes beams, the combined beams behave like transform-limited (i.e. unchirped) pulses with a different effective pulse length.

Chirped fs pulses are spread out in time which leads to a change of frequency as a function of time. If the pump and Stokes are chirped the same way (i.e. they have the same slope), the difference between them is a constant as a function of time and hence the **CARS** resonance is a constant (**CARS** depends on $\omega_P$ - $\omega_S = \omega_R$).

By varying the slope of pump and Stokes, the effective pulse length is changed and allows us to easily tune for optimal performance. An advantage of this approach is that by changing the temporal overlap between the pump and Stokes pulses, we can change the frequency difference (i.e. we change from $\Omega_1$ to $\Omega_2$). This would allow us to tune to the different Raman resonances and probe different molecules. For the specific case of cardiovascular diseases, it would become possible to identify different types of lipids within the vessel wall.

### 10.1.2 Data analysis

The methods presented in this thesis represent a big step towards making **NLO** microscopy a quantitative tool for a broad number of applications in biomedical sciences. However, many more aspects can be explored.

As previously discussed, texture analysis refers to the branch of imaging science that is concerned with the description of characteristic image properties by textural features. There is no universally agreed-upon definition of what image texture is and in general different researchers use different definitions depending upon the particular area of application. In this thesis, first order statistics (**FOS**) and features extracted from gray level co-occurence matrix (**GLCM**) were tested and proved to be useful. However, many other textural-based features can be extracted from images. Future plans regarding image analysis must include exploring new methods, striving to expand the ensemble of features that can be effectively extracted from **NLO** images.

For example, the grey-level run length method (**GLRLM**) which is based on the analysis of higher-order statistical information is on the top of my list for future testing. GLRLMs contain information on the run of a particular grey-level, or grey-level range, in a particular direction. The number of pixels contained within the run is the run-length. A coarse texture will therefore be dominated by relatively long runs whereas a fine texture will be populated by much shorter runs. Especially when dealing with fiber-like structures, the specific information that can be obtained through **GLRLM** is a useful set for classifying several conditions.

Another possible path to be followed in future works is related to fractal texture analysis. The application of fractal dimension from box-counting was discussed and presented in this thesis research, showing promising results. As previously discussed, the box-counting dimension is closely related to the concept of self-similarity where a structure is sub-divided into smaller elements, each a smaller replica of the original structure. This sub-division characterizes the structure by a self-similarity, or fractal, dimension and is a useful tool for characterizing apparently random structures.

Extracting textural features based on fractal analysis seems to be very promising objective analysis of **NLO** images obtained from several applications. The fractal dimension describes the disorder of an object numerically, which can be an important information for studying with biological tissues, macromolecules and its composition.

### 10.1.3 Bio-specific aspects

As extensively discussed in this thesis research, collagen is one of the main biological compounds of many biological systems. Detection and characterization of changes in collagen play a key role in the diagnosis of several conditions, and these changes can also be linked to the severity and type of lesions. We have developed and tested methods that are able to track general changes in collagen deposition; however, another important aspect must be addressed: the differentiation between collagen types.

Collagen is a structural protein which provides the extracellular framework for all multi-cellular organisms. The most commonly present fibrillar collagen subtypes are collagen type I and III with specific physiological and structural functions. For instance, the collagen type I plays a key role as supporting elements for high tensile strength and the modulus, while collagen type III forms unique highly elastic network storing kinetic energy. Therefore, an unbalanced production of collagen subtypes is expected to result in altered physical and biomechanical properties of tissues.

In general, providing label-free, highly specific discrimination between differing collagen isoforms could be a powerful means to study the underlying biological changes in several conditions, as well as provide a new diagnostic tool.

By studying changes regarding the signal polarization, the ratio between forward and backward detected **SHG** signal as well as developing new specific tools to differentiate signal coming from different structures, can represent the first steps towards the differentiation of collagen fibers.

# Appendix A

# Some sources of NLO signal in biological samples

| **Two-photon fluorophore** | **Excitation wavelength** $[nm]$ | **Cross-section** $[GM]$ |
|---|---|---|
| NAD(P)H | $690 - 730$ | $9 \times 10^{-2}$ |
| Flavoproteins (flavins) | $700 - 730$ | $0.1 - 0.8$ |
| Lipofuscin | $700 - 850$ | $High$ |
| Retinol | $700 - 830$ | $7 \times 10^{-2}$ |
| Pyridoxine (vitamin B6) | $690 - 710$ | $8 \times 10^{-3}$ |
| Folic Acid | $700 - 770$ | $7 \times 10^{-3}$ |
| Cholecalciferol | $\leq 700$ | $6 \times 10^{-4}$ |
| NFT (neurofibrillary tangles) | $700 - 780$ | $Unknown$ |
| Collagen | $\leq 750$ | $Unknown$ |
| Keratin | $\approx 720$ | $2.5 \times 10^{-3}$ |
| Elastin | $700 - 740$ | $Unknown$ |
| Fluorescein (dye) | 780 | 38 (at $780nm$) |

**Table A.1:** Some examples of two-photon fluorophores detected in biological samples [2–4].

| **SHG source** | **Structure description** | **Biological compound** |
|---|---|---|
| Fibrillae collagen | Protein molecules (triple helix structure) | Extracellular matrix |
| Tubulin | Rod shaped protein molecules | Cytoskeleton |
| Microtubules | Rod shaped protein molecules | Cytoskeleton |
| Actin/myosin | Rod shaped protein molecules | Muscle fibers |
| Starch | Strings of polysaccharides chiral structure | Food store in plants |

**Table A.2:** Sources that can be used for SHG in biological samples [5–10].

| **Bond vibration** | $(\omega_p - \omega_s)$ $[cm^{-1}]$ | **Provides contrast for:** |
|---|---|---|
| $CH_2$ $\nu_{sym.}$ | 2845 and 2840 | Lipids, polystyrene beads, starch grains |
| Aliphatic $CH$ $\nu_{sym.}$ | 2870 | Lipids (lysomes, mitochondria, nucleus) |
| $PO_2$ $\nu_{sym.}$ | 1090 | DNA (chromosomes) |
| Amide I | 1650 | Proteins |
| $H_2O$ $\nu_{sym.}$ | 3200 | Water |

**Table A.3:** Vibrational modes used for CARS microscopy in biological tissues. $\nu_{sym.}$: *symmetric stretching vibration.* [11–15].

# Appendix B

# Tubeness

*This appendix contains text excerpts from Sato, Yoshinobu, Shin Nakajima, Nobuyuki Shiraga, Hideki Atsumi, Shigeyuki Yoshida, Thomas Koller, Guido Gerig, and Ron Kikinis. "Three-dimensional multi-scale line filter for segmentation and visualization of curvilinear structures in medical images." Medical image analysis 2, no. 2 (1998): 143-168. Reproduced with permission from Elsevier.*

The tubeness filter is nothing more than a method for the enhancement of curvilinear structures such as vessels and bronchi in three-dimensional (3-D) medical images. A 3-D line enhancement filter is developed with the aim of discriminating line structures from other structures and recovering line structures of various widths.

The 3-D line filter is based on a combination of the eigenvalues of the 3-D Hessian matrix. Multi-scale integration is formulated by taking the maximum among single-scale filter responses, and its characteristics are examined to derive criteria for the selection of parameters in the formulation.

The resultant multi-scale line-filtered images provide significantly improved segmentation and visualization of curvilinear structures. In this way, Sato, Yoshinobu, et al. has developed a practical and general-purpose approach to 3-D line enhancement filtering, by accomplish the following:

1. recovery of line structures of various widths (especially thin structures);

2. removal of the effects of structures other than line structures;
3. removal of the effects of nonuniformity of contrast material; and
4. removal of noise and artifacts.

## B.1 3-D line filter based on Hessian Matrix

The second derivative has typically been used for line enhancement filtering. The Gaussian convolution is combined with the second derivative in order to tune the filter response to the specific widths of lines as well as to reduce the effect of noise. In the one-dimensional (1-D) case, the response of the line filter is given by

$$R(x;\sigma_f) = \left\{ -\frac{d^2}{dx^2} G(x;\sigma_f) \right\} * I(x) \tag{B.1}$$

where * denotes the convolution, I(x) is an input profile function, and $G(x;\sigma_f)$ is the Gaussian function with the standard deviation $\sigma_f$, defined as $(1/\sqrt{2\pi\sigma_f})exp(-x^2/2{\sigma_f}^2)$. The sign of the Gaussian derivative has been inverted so the responses have positive values for the bright line. The profile was considered having the Gaussian shape given by

$$L(x;\sigma_f) = exp\left(-\frac{x^2}{2\sigma_x^2}\right), \tag{B.2}$$

where $\sigma_x$ is the standard deviation of the profile. The height of the profile is constant for any $\sigma_x$. Let the filter response to $L(x;\sigma_x)$ be $R_L(x;\sigma_f,\sigma_x)$, that is,

$$R_L(x;\sigma_f,\sigma_x) = \left\{ -\frac{d^2}{dx^2} G(x;\sigma_f) \right\} * L(x;\sigma_x) \tag{B.3}$$

$R_L(x;\sigma_f,\sigma_x)$ is maximum at $\sigma_x = \sigma_f/\sqrt{2}$ and $x = 0$ when $\sigma_f$ is fixed. The filter with standard deviation $\sigma$ is considered to be tuned to the Gaussian profile with $\sigma_x = \sigma_f/\sqrt{2}$. The above discussion can also be applied to other line-like profiles such as a box shape.

The 1-D line filter can be extended to multi-dimensional line filters using the Hessian matrix, which describes the second-order structures of local intensity variations around

each point of a multi-dimensional image [184–186]. The Hessian matrix of a 3-D image I(x) (where $x = (x, y, z)$) is given by

$$\nabla^2 I(x) = \begin{bmatrix} I_{xx}(x) & I_{xy}(x) & I_{xz}(x) \\ I_{yx}(x) & I_{yy}(x) & I_{yz}(x) \\ I_{zx}(x) & I_{zy}(x) & I_{zz}(x) \end{bmatrix} \tag{B.4}$$

where partial second derivatives of the image $I(x)$ are represented by expressions like $I_{xx}(x) = \frac{\partial^2}{\partial x^2} I(x)$, $I_{yz}(x) = \frac{\partial^2}{\partial y \partial z} I(x)$, and so on.

Let the eigenvalues of $\nabla^2 I(x)$ be $\lambda_1(x)$, $\lambda_2(x)$ and $\lambda_3(x)$ as$(\lambda_1(x) > \lambda_2(x) > \lambda_1(x)$, and their corresponding eigenvectors be $e_1(x)$, $e_2(x)$ and $e_3(x)$ respectively. The eigenvector $e_1(x)$, corresponding to the largest eigenvalue $\lambda_1(x)$, represents the direction along which the second derivative is maximum, and $\lambda_1(x)$ gives the maximum second derivative value. The partial second derivatives of $I(x)$ in Equation B.4 can be replaced by the partial second derivatives of Gaussian, for example,

$$I_{xx}(x; \sigma_f) = \left\{ -\frac{\partial^2}{\partial x^2} G(x; \sigma_f) \right\} * I(x) \tag{B.5}$$

where $G(x; \sigma_f)$ is an isotropic Gaussian function with standard deviation $\sigma$. Using the Hessian matrix $\nabla^2 I(x; \sigma_f)$ based on the second derivatives of Gaussian with $\sigma_f$, the eigenvalues $\lambda_1(x; \sigma_f)$, $\lambda_2(x; \sigma_f)$ and $\lambda_3(x; \sigma_f)$ as filter responses can be tuned to a specific width of 3-D line.

Let us consider an ideal bright 3-D line image with Gaussian cross-sectional images given by

$$L(x; \sigma_r) = exp\left( -\frac{x^2 + y^2}{2\sigma_r^2} \right), \tag{B.6}$$

where $\sigma_r$ is the standard deviation that controls the width of the line, and the height is constant for any $\sigma_r$. Let $\nabla^2 L(x; \sigma_r, \sigma_f)$ be the Hessian matrix combined with the Gaussian convolution with $\sigma_f$ for the ideal line $L(x; \sigma_r)$. Among the eigenvalues of $\nabla^2 L(x; \sigma_r, \sigma_f)$, both $\lambda_2(x)$ and $\lambda_3(x)$ have the same minimum at $x = y = 0$ (the center

of the line) and $\sigma_r = \sigma_f$ when $\sigma_f$ is fixed. When $\lambda_2(x)$ and $\lambda_3(x)$ are minimum, $\lambda_1(x)$ is zero. Therefore, the conditions of a bright line can be regarded as

$$\lambda_1 \approx 0 \text{ and } \lambda_2 \approx \lambda_3 \ll 0 \tag{B.7}$$

Based on the condition $\lambda_2 \approx \lambda_3 \ll 0$, the following has been suggested as similarity measures to a line structure [185, 186]:

$$\lambda_{min_{23}} = \begin{cases} min(-\lambda_2, -\lambda_3) = -\lambda_2, & \lambda_3 < \lambda_2 < 0; \\ 0, & \text{otherwise} \end{cases}$$

and

$$\lambda_{g-mean_{23}} = \begin{cases} \sqrt{\lambda_2 \lambda_3}, & \lambda_3 < \lambda_2 < 0; \\ 0, & \text{otherwise} \end{cases}$$

For the cases $\lambda_2 \ll 0$ and $\lambda_3 \leq 0$, $\lambda_{min_{23}}$ can be rewritten as

$$\lambda_{min_{23}} = -\lambda_2 = |\lambda_3| \left( \frac{\lambda_2}{\lambda_3} \right) \tag{B.8}$$

and $\lambda_{g-mean23}$ as

$$\lambda_{g-mean_{23}} = \sqrt{\lambda_2 \lambda_3} = |\lambda_3| \left( \frac{\lambda_2}{\lambda_3} \right)^{0.5} \tag{B.9}$$

Now, we generalize these two measures and introduce a new measure defined as

$$\lambda_{23} = \begin{cases} |\lambda_3| w_{23}(\lambda_2, \lambda_3;), & \lambda_3 < \lambda_2 < 0; \\ 0, & \text{otherwise} \end{cases}$$

in which

$$w_{23}(\lambda_2, \lambda_3;) = \left( \frac{\lambda_2}{\lambda_3} \right)^{\gamma_{23}}, \tag{B.10}$$

where $\gamma_{23}$ ($\gamma_{23} \leq 0$) controls the sharpness of the selectivity for the cross-section isotropy. In the definition of $\lambda_{23}$, $|\lambda_{23}|$ is multiplied by the weight function $w_{23}$ ($\lambda_2; \lambda_3$ ) which decreases with the deviation from the condition $\lambda_3 = \lambda_2$.

$\lambda_{23}$ is equivalent to $\lambda_{min_{23}}$ and $\lambda_{g-mean_{23}}$ when $\gamma_{23} = 1$ and $\gamma_{23} = 0.5$ respectively. When $|\lambda_3| \gg |\lambda_2| \approx 0$, the structure should be regarded as sheet-like rather than line-like and $|\lambda_{23}|$ should not be large.

It is important to be able to discriminate line structures from sheet-like structures because 3-D medical images often contain strong sheet-like structures such as the skin or the skull.

The condition $\lambda_1 \approx 0$ should be combined with the similarity measure to a line. As in the definition of $\lambda_{23}$ , we introduce a weight function that decreases with the deviation from the condition $\lambda_1 = 0$. The line measure is defined as

$$\lambda_{123} = \begin{cases} \lambda_{23} w_{12}(\lambda_1; \lambda_2), & \lambda_3 < \lambda_2 < 0; \\ \\ 0, & \text{otherwise} \end{cases}$$

in which $w_{12}(\lambda_1; \lambda_2)$ is a weight function written as

$$w_{12}(\lambda_1; \lambda_2) = \begin{cases} \left(1 + \frac{\lambda_1}{|\lambda_2|}\right)^{\gamma_{12}} & \lambda_1 \leq 0; \\ 0, & \text{otherwise} \end{cases}$$

where $\gamma_{12} \geq 0$ and $0 < \alpha \leq 1.0$. $\alpha$ is introduced in order to give $w_{12}(\lambda_1; \lambda_2)$ an asymmetrical characteristic in the negative and the positive regions of $\lambda_1$. When $\lambda_1$ is negative and $|\lambda_1| \approx |\lambda_2| \gg 0$, the structure should be regarded as blob-like rather than line-like. Because noise components typically have blob-like shapes, it is important that the system possesses the ability to discriminate between lines and blobs. Thus, for negative $\lambda_1$, the weight function should decrease with deviation from $\lambda_1 = 0$ in the same manner as in the case of the discrimination between sheets and lines. When $\lambda_1$ is positive, the structure involves concavity in the estimated line direction.

# Appendix C

# Support Vector Machine classifiers

Kernel Functions are used in many applications to provide a simple bridge between linearity and non-linearity for algorithms. In pattern recognition, we want our algorithms to analyze and classify data efficiently. If the boundary between two sets of points is too crooked, the algorithm will require a long processing times to converge. Even when it converges, it might not be the most optimal boundary.

The main characteristic of Kernel Functions in machine learning is their distinct approach: instead of classifying the data in lower dimension by putting a really curvy line, Kernel Functions map the data into higher dimensional spaces in the hope that the data is more easily separated there. There are also no constraints on the form of this mapping, which could even lead to infinite-dimensional spaces. The advantage about this mapping function is that it hardly needs to be computed because of a tool called the Kernel Trick.

The original optimal hyperplane algorithm proposed by Vladimir Vapnik in 1963 was a linear classifier [119]. However, in 1992, Bernhard Boser, Isabelle Guyon and Vapnik suggested a way to create non-linear classifiers by applying the kernel trick to maximum-margin hyperplanes [187].

The kernel trick is a mathematical tool which can be applied to any algorithm which solely depends on the dot product between two vectors. There is a need to transform data into higher dimensions, but it cannot be just randomly projected. It is not practical

to compute the mapping explicitly either. Hence, only those algorithms which use dot products of vectors in the higher dimension are used to determine the boundary.

This dot product corresponds to the mathematical processing step. To compute the dot products of vectors in the higher dimension, there is no need to project the data into higher dimensions. A kernel function can be used to compute the dot product directly using the lower dimension vectors.

Choosing the most appropriate kernel highly depends on the problem at hand. Most of the times, fine tuning its parameters becomes a crucial task. For example, a polynomial kernel allows us to model feature conjunctions up to the order of the polynomial. Feature conjunction refers to the process of fusing two or more features together. Radial basis functions allows to put circular boundaries (or hyperspheres in higher dimensions). This is useful where the data is distributed in a loop-like shape. This is in contrast with the Linear kernel, which allows only to put linear boundaries (or hyperplanes in higher dimensions). The motivation behind the choice of a particular kernel can be very intuitive and straightforward depending on what kind of information we are expecting to extract about the data.

Some popular kernels:

- **Linear Kernel:** it is one of the simplest kernel functions. It is just the inner product ¡x,y¿ plus a constant c.
- **Polynomial Kernel:** these kernels are useful for problems where all the training data is normalized. It is possible to use polynomial of any order depending on the case at hand.
- **Gaussian Kernel:** this comes in the category of radial basis functions. Fine-tuning of the $\gamma$ parameter plays a major role in the performance of this kernel. If it is overestimated, the exponential will behave almost linearly and the higher-dimensional projection will start to lose its non-linear power. On the other hand, if it is underestimated, the decision boundary will be highly sensitive to noise in training data. There are a few more radial basis functions like Exponential, Laplacian, ANOVA etc.

There are many more kernel functions such as Spherical, Wavelet, Bayesian, Cauchy, Bessel. Depending on the problem at hand, the appropriate kernel function must be defined. Different kernels have different advantages and disadvantages.

# Appendix D

# Peer-reviewed Journal Papers & Conference Proceedings

Parts of this thesis have appeared in peer reviewed conferences and papers. These parts have involved collaborations between myself, and members of the spectroscopy group based at the National Research Council Canada, in Winnipeg-MB.

Most of the published papers explicitly contain the contribution of each author; however, in general lines, I conceived all methods presented in this thesis (and published works), performed imaging measurements and all data analyses.

Other authors contributed by establishing the rabbit colony, co-ordinating animal service and imaging works, providing expertise on setting up and maintaining NLO imaging microscope as well as providing some guidance during the process of image classification.

## Peer-reviewed Journal Papers

1. **Mostaço-Guidolin L.B.**, Ko A.C-T., A. Ridsdale, Pegoraro A. F., Smith M.S.D., Hewko M.D., Kohlenberg E.K., Schattka B.J., Shiomi M., Stolow A., Sowa M.G., *Differentiating atherosclerotic plaque burden in arterial tissues using femtosecond CARS-based multimodal nonlinear optical imaging*, Biomedical Optics Express, Vol. 1, Issue 1, pp. 59 (2010)

2. Ko A.C-T, Ridsdale A., Smith M.S.D., **Mostaço-Guidolin L.B.**, Hewko M.D., Pegoraro A.F., Kohlenberg E.M., Schattka B., Shiomi M., Stolow A., and Sowa M.G., *Multimodal nonlinear optical imaging of atherosclerotic plaque development in myocardial infarction-prone rabbits*, Journal of Biomedical Optics, 15, 020501 (2010)

3. **Mostaço-Guidolin L.B.**, Ko A.C-T, Popescu D.P., Smith M.S.D., Kohlenberg E.K., Shiomi M., Major A., and Sowa M.G., *Evaluation of texture parameters for the quantitative description of multimodal nonlinear optical images from atherosclerotic rabbit arteries*, Journal of Physics in Medicine and Biology, 56, pp. 5319 (2011)

4. Ko A.C-T, **Mostaço-Guidolin L.B.**, Ridsale A., Major A., Stolow A., and Sowa M.G., *Nonlinear optical microscopy in decoding arterial diseases*, Biophysical Reviews, DOI:10.1007/s12551-012-0077-8 (2012)

5. **Mostaço-Guidolin L.B.**, Ko A.C-T, Wang F., Xing B., Smith M.S.D., Kohlenberg E.K., Tian G., Major A., and Sowa M.G., *Collagen morphology and Texture analysis: from statistics to classification*, Scientific Reports, 3, 2190 (2013) - *highlighted in Extracellular Matrix News 4.28*

6. **Mostaço-Guidolin L.B.**, Kohlenberg E.K., Smith M.S.D., Hewko M, Major A., Sowa M.G., and Ko A.C-T, *Optical Index for Plaque Burden: tracking atherosclerotic plaque development through multimodal nonlinear optical microscopy*, DOI: 10.1021/ac5005635, Analytical Chemistry (2014)

## Peer-reviewed Journal Papers - submitted and in preparation

1. **Mostaço-Guidolin L.B.**, Ko A.C-T., Smith M.S.D., Hewko M.D., Kohlenberg

E.K., Shiomi M., Major A., Sowa M.G., *Femtosecond CARS-based multimodal nonlinear optical images: statistical, textural and structural analysis to classify lipid-rich cells in atherosclerosis*, in preparation

2. **Mostaço-Guidolin L.B.**, Ko A.C-T., Smith M.S.D., Hewko M.D., Kohlenberg E.K., Shiomi M., Major A., Sowa M.G., *Multiphoton spectroscopical analysis of atherosclerotic lesions*, in preparation

3. **Mostaço-Guidolin L.B.**, Ko A.C-T., Smith M.S.D., Hewko M.D., Kohlenberg E.K., Shiomi M., Major A., Sowa M.G., *Fractal dimension and fiber directionality: characterizing elastin disruption imaged by two-photon emission fluorescence*, in preparation

4. **Mostaço-Guidolin L.B.**, Guidolin L.C., Ko A.C-T, Major A., and Sowa M.G., *Second harmonic generation image analysis: classification of collagen fibrils based on textural features*, in preparation

5. **Mostaço-Guidolin L.B.**, Ko A.C-T., Smith M.S.D., Hewko M.D., Kohlenberg E.K., Shiomi M., Major A., Sowa M.G., *Shining light on arteries: optical techniques to evaluate atherosclerotic plaques*, in preparation

## Conference Proceedings - oral presentations

1. Ko A.C-T., **Mostaço-Guidolin L.B.**, Ridsdale A., Pegoraro A.F., Smith M.S.D., Slepkov A., Hewko M.D., Kohlenberg E.K., Schattka B.J., Masashi Shiomi, Stolow A., and Sowa M.G. *Imaging luminal atherosclerosis by femtosecond multimodal CARS (MM-CARS) to determine plaque burden*, in Biomedical Sciences XI, Proc. SPIE Vol. 7903 (2011).

2. Ko A.C-T., **Mostaço-Guidolin, L.B.**, Ridsdale, A., Hewko, M.D., Kohlenberg, E.M., Schattka, B.J., Smith, M.S.D., Shiomi, M., Stolow, A., Pegoraro, A.F., Sowa, M.G., *Diagnostic imaging for interrogating atherosclerotic plaque burden using multi-modal CARS*, in Microscopy, Proc. SPIE Vol. 7903 (2011).

3. Ko AC-T, **Mostaço-Guidolin L.B.**, Wang F., Xing B., Smith M.S.D., Major A., Tian G., Sowa M.G., *Comparison and Quantification of type-I collagen fibrils in infarcted and adipose- derived stem-cell therapied myocardium tissues using label-free nonlinear optical microscopy*, Photonics West – SPIE 2012.

4. **Mostaço-Guidolin L.B.**, Ko A.C-T, Popescu D.P., Smith M.S.D., Kohlenberg E.K., Shiomi M., Major A. and Sowa M.G., *Evaluation of Atherosclerotic Plaque Development by Texture Analysis of Multimodal CARS Images of Rabbit Arteries*, Photonics West – SPIE 2012.
5. **Mostaço-Guidolin L.B.**, Ko A.C-T, Wang F., Tian H., Hewko M.,Shiomi M., Major A. and Sowa M.G., *A new approach to evaluate collagen morphology and lipid deposition using multiphoton image statistics*, to Photonics West – SPIE 2014.

## Conference Proceedings - poster presentations

1. **Mostaço-Guidolin L.B.**, Ko A.C-T., Major A., Smith M.S.D., Hewko M., Kohlenberg E.K., Schattka B., Shiomi M., and Sowa M.G. *Shedding light into atherosclerosis: a quantitative study of nonlinear optical imaging in tracking plaque development*, in CIHR Manitoba Student Research Poster Competition (2014).

2. **Mostaço-Guidolin L.B.**, Ko A.C-T, Major A., Smith M.S.D., Hewko M., Kohlenberg E.K., Schattka B., Shiomi M., and Sowa M.G., *Quantitative study of nonlinear optical imaging in tracking plaque development*, to Photonics North – SPIE

2014.

3. **Mostaço-Guidolin L.B.**, Ko A.C-T, Major A., Smith M.S.D., Hewko M., Kohlenberg E.K., Schattka B., Shiomi M., and Sowa M.G., *Shedding light into atherosclerosis: a quantitative study of nonlinear optical imaging in tracking plaque development*, to Photonics West – SPIE 2014.

4. **Mostaço-Guidolin L.B.**, Ko A.C-T, Major A., Hewko M.,Shiomi M., and Sowa M.G., *Classifying collagen remodeling and pathological lipid deposition by multimodal label-free microscopy and image statistics*, to Photonics West – SPIE 2014.

5. **Mostaço-Guidolin L.B.**, Ko A.C-T., Major A., Smith M.S.D., Hewko M., Kohlenberg E.K., Schattka B., Shiomi M., and Sowa M.G. *Emerging optical imaging modalities enable characterization of arterial plaque burden*, in CIHR Manitoba Student Research Poster Competition (2012).

# Appendix E

# Awards, Fellowships & Scholarships

- **2014** Award, *CIHR Honourable Mention*, CIHR Manitoba Student Research Poster Competition
- **2014** Award, *Dean of Faculty of Graduate Studies Poster Award*, CIHR Manitoba Student Research Poster Competition
- **2014** Award, *Best Poster presentation*, Photonics North - SPIE
- **2014** Award, *Best Poster presentation*, Photonics West - SPIE
- **2014** Award, *Research Excellence*, Photonics West - SPIE
- **2014** Award, *Edward R. Toporeck Graduate Fellowship in Engineering*
- **2013** Award, *Edward R. Toporeck Graduate Fellowship in Engineering*
- **2012** Award, *Berdie and Irvin Cohen Fellowship*
- **2012** Award, *Elizabeth Anne Hogan Memorial Scholarship*
- **2012** Award, *Edward R. Toporeck Graduate Fellowship in Engineering*
- **2012** Scholarship, *International Graduate Student Scholarship*
- **2011** Scholarship, *Internaional Graduate Student Entrance Scholarship*
- **2011-2014** Fellowship, *University of Manitoba Graduate Fellowship (UMGF)*

# Bibliography


1. Wang H, Langohr I, Sturek M, Cheng J: **Imaging and quantitative analysis of atherosclerotic lesions by CARS-based multimodal nonlinear optical microscopy**. *Arteriosclerosis, thrombosis, and vascular biology* 2009, **29**(9):1342.

2. Zoumi A, Yeh A, Tromberg B: **Imaging cells and extracellular matrix in vivo by using second-harmonic generation and two-photon excited fluorescence**. *Proceedings of the National Academy of Sciences* 2002, **99**(17):11014.

3. Zipfel W, Williams R, Christie R, Nikitin A, Hyman B, Webb W: **Live tissue intrinsic emission microscopy using multiphoton-excited native fluorescence and second harmonic generation**. *Proceedings of the national academy of sciences of the United States of America* 2003, **100**(12):7075.

4. Pena A, Strupler M, Boulesteix T, Schanne-Klein M: **Spectroscopic analysis of keratin endogenous signal for skin multiphoton microscopy**. *Optics express* 2005, **13**(16):6268–6274.

5. Campagnola P, Millard A, Terasaki M, Hoppe P, Malone C, Mohler W: **Three-dimensional high-resolution second-harmonic generation imaging of endogenous structural proteins in biological tissues**. *Biophysical journal* 2002, **82**:493–508.

6. Freund I, Deutsch M, Sprecher A: **Connective tissue polarity. Optical second-harmonic microscopy, crossed-beam summation, and small-angle scattering in rat-tail tendon**. *Biophysical journal* 1986, **50**(4):693–712.

7. Dombeck D, Kasischke K, Vishwasrao H, Ingelsson M, Hyman B, Webb W: **Uniform polarity microtubule assemblies imaged in native brain tissue by second-**

**harmonic generation microscopy**. *Proceedings of the National Academy of Sciences of the United States of America* 2003, **100**(12):7081.

8. Chu S, Chen S, Chern G, Tsai T, Chen Y, Lin B, Sun C: **Studies of [chi](2)/[chi](3) tensors in submicron-scaled bio-tissues by polarization harmonics optical microscopy**. *Biophysical journal* 2004, **86**(6):3914–3922.

9. Plotnikov S, Millard A, Campagnola P, Mohler W: **Characterization of the myosin-based source for second-harmonic generation from muscle sarcomeres**. *Biophysical journal* 2006, **90**(2):693–703.

10. Amat-Roldán I, Cormack I, Loza-Alvarez P, Artigas D: **Starch-based second-harmonic-generated collinear frequency-resolved optical gating pulse characterization at the focal plane of a high-numerical-aperture lens**. *Optics letters* 2004, **29**(19):2282–2284.

11. Evans C, Xie X: **Coherent anti-Stokes Raman scattering microscopy: chemical imaging for biology and medicine**. *Annu. Rev. Anal. Chem.* 2008, **1**:883–909.

12. Wang H, Fu Y, Zickmund P, Shi R, Cheng J: **Coherent anti-Stokes Raman scattering imaging of axonal myelin in live spinal tissues**. *Biophysical Journal* 2005, **89**:581–591.

13. Volkmer A, Cheng J, Sunney Xie X: **Vibrational imaging with high sensitivity via epidetected coherent anti-Stokes Raman scattering microscopy**. *Physical Review Letters* 2001, **87**(2):23901.

14. Cheng J, Jia Y, Zheng G, Xie X: **Laser-scanning coherent anti-Stokes Raman scattering microscopy and applications to cell biology**. *Biophysical journal* 2002, **83**:502–509.

15. Cheng J, Book L, Xie X: **Polarization coherent anti-Stokes Raman scattering microscopy**. *Optics Letters* 2001, **26**(17):1341–1343.

16. Mostaço-Guidolin L, Ko A, Popescu D, Smith M, Kohlenberg E, Shiomi M, Major A, Sowa M: **Evaluation of texture parameters for the quantitative description of mul-**

**timodal nonlinear optical images from atherosclerotic rabbit arteries**. *Physics in Medicine and Biology* 2011, **56**:5319.

17. Mostaço-Guidolin LB, Sowa MG, Kohlenberg EK, Smith M, Hewko M, Major A, Ko ACT: **Quantitative nonlinear optical assessment of atherosclerosis progression in rabbits**. *Analytical Chemistry* 2014.

18. Mostaço-Guidolin L, Sowa M, Ridsdale A, Pegoraro A, Smith M, Hewko M, Kohlenberg E, Schattka B, Shiomi M, Stolow A, et al.: **Differentiating atherosclerotic plaque burden in arterial tissues using femtosecond CARS-based multimodal nonlinear optical imaging**. *Biomedical Optics Express* 2010, **1**:59–73.

19. Buja L, Kita T, Goldstein J, Watanabe Y, Brown M: **Cellular pathology of progressive atherosclerosis in the WHHL rabbit. An animal model of familial hypercholesterolemia**. *Arteriosclerosis, Thrombosis, and Vascular Biology* 1983, **3**:87.

20. Mostaço-Guidolin LB, Ko ACT, Wang F, Xiang B, Hewko M, Tian G, Major A, Shiomi M, Sowa MG: **Collagen morphology and texture analysis: from statistics to classification**. *Scientific reports* 2013, **3**.

21. Ko AC, Ridsdale A, Pegoraro AF, Smith MS, Mostaço-Guidolin LB, Hewko MD, Kohlenberg EM, Schattka BJ, Shiomi M, Stolow A, et al.: **Label-free imaging of arterial tissues using photonic crystal fiber (PCF) based nonlinear optical microscopic system**. In *SPIE BiOS: Biomedical Optics*, International Society for Optics and Photonics 2009:718204–718204.

22. Mostaço-Guidolin LB, Sowa MG, Ridsdale A, Pegoraro AF, Smith MS, Hewko MD, Kohlenberg EK, Schattka B, Shiomi M, Stolow A, et al.: **Differentiating atherosclerotic plaque burden in arterial tissues using femtosecond CARS-based multimodal nonlinear optical imaging**. *Biomedical optics express* 2010, **1**:59–73.

23. Ko AC, Mostaço-Guidolin LB, Ridsdale A, Pegoraro AF, Smith MS, Slepkov A, Hewko MD, Kohlenberg EK, Schattka B, Stolow A, et al.: **Using multimodal femtosecond CARS imaging to determine plaque burden in luminal atherosclerosis**. In *SPIE BiOS*, International Society for Optics and Photonics 2011:790318–790318.

24. Ko ACT, Ridsdale A, Mostaço-Guidolin LB, Major A, Stolow A, Sowa MG: **Nonlinear optical microscopy in decoding arterial diseases**. *Biophysical Reviews* 2012, **4**(4):323–334.

25. Mostaço-Guidolin LB, Ko ACT, Wang F, Tian H, Hewko M, Shiomi M, Major A, Sowa MG: **Evaluating collagen morphology and pathological lipid deposition using multiphoton image statistics**. In *SPIE BiOS*, International Society for Optics and Photonics 2014:89482A–89482A.

26. Sato Y, Nakajima S, Shiraga N, Atsumi H, Yoshida S, Koller T, Gerig G, Kikinis R: **Three-dimensional multi-scale line filter for segmentation and visualization of curvilinear structures in medical images**. *Medical image analysis* 1998, **2**(2):143–168.

27. Mertz J: **Nonlinear microscopy: new techniques and applications**. *Current opinion in neurobiology* 2004, **14**(5):610–616.

28. Yue S, Slipchenko M, Cheng J: **Multimodal nonlinear optical microscopy**. *Laser & Photonics Reviews* 2011.

29. Williams R, Zipfel W, Webb W: **Multiphoton microscopy in biological research**. *Current opinion in chemical biology* 2001, **5**(5):603–608.

30. Zipfel W, Williams R, Webb W: **Nonlinear magic: multiphoton microscopy in the biosciences**. *Nature Biotechnology* 2003, **21**(11):1369–1377.

31. Pfeffer C, Olsen B, Ganikhanov F, Légaré F: **Multimodal nonlinear optical imaging of collagen arrays**. *Journal of structural biology* 2008, **164**:140–145.

32. Evans C, Xie X: **Coherent anti-Stokes Raman scattering microscopy: chemical imaging for biology and medicine**. *Annu. Rev. Anal. Chem.* 2008, **1**:883–909.

33. Masihzadeh O, Schlup P, Bartels R: **Label-free second harmonic generation holographic microscopy of biological specimens**. *Optics Express* 2010, **18**(10):9840–9851.

34. Pawley J: *Handbook of biological confocal microscopy*. Springer Verlag 2006.

35. Le T, Langohr I, Locker M, Sturek M, Cheng J: **Label-free molecular imaging of atherosclerotic lesions using multimodal nonlinear optical microscopy**. *Journal of biomedical optics* 2007, **12**:054007.

36. Zoumi A, Lu X, Kassab G, Tromberg B: **Imaging coronary artery microstructure using second-harmonic and two-photon fluorescence microscopy**. *Biophysical journal* 2004, **87**(4):2778–2786.

37. Wang H, Le T, Cheng J: **Label-free imaging of arterial cells and extracellular matrix using a multimodal CARS microscope**. *Optics communications* 2008, **281**(7):1813–1822.

38. Ko A, Ridsdale A, Smith M, Mostaço-Guidolin L, Hewko M, Pegoraro A, Kohlenberg E, Schattka B, Shiomi M, Stolow A, et al.: **Multimodal nonlinear optical imaging of atherosclerotic plaque development in myocardial infarction-prone rabbits**. *Journal of Biomedical Optics* 2010, **15**:020501.

39. Wang H, Simianu V, Locker M, Cheng J, Sturek M: **Stent-induced coronary artery stenosis characterized by multimodal nonlinear optical microscopy**. *Journal of Biomedical Optics* 2011, **16**(2):021110.

40. Lilledahl M, Pierce D, Ricken T, Holzapfel G, de Lange Davies C: **Structural Analysis of Articular Cartilage Using Multiphoton Microscopy: Input for Biomechanical Modeling**. *IEEE transactions on medical imaging* 2011.

41. Megens R, oude Egbrink M, Merkx M, Slaaf D, van Zandvoort M: **Imaging Collagen and Inflammatory Cells in Atherosclerotic Plaques in Vital Carotid Arteries using Two-Photon Microscopy**. *Vital Imaging of Large Arteries using Two-Photon Laser Scanning Microscopy: Focus on the Arterial Wall* 2008, :87.

42. Doras C, Taupier G, Barsella A, Mager L, Boeglin A, Bulou H, Bousquet P, Dorkenoo K: **Polarization state studies in second harmonic generation signals to trace atherosclerosis lesions**. *Optics Express* 2011, **19**(16):15062–15068.

43. Ross R, et al.: **Atherosclerosis is an inflammatory disease**. *American Heart Journal* 1999, **138**:419–420.

44. Furchgott R: **Role of endothelium in responses of vascular smooth muscle**. *Circulation Research* 1983, **53**(5):557–573.

45. Conway E, Collen D, Carmeliet P: **Molecular mechanisms of blood vessel growth**. *Cardiovascular research* 2001, **49**(3):507.

46. Smith E: **Transport, interactions and retention of plasma proteins in the intima: the barrier function of the internal elastic lamina**. *European Heart Journal* 1990, **11**(suppl E):72.

47. Cliff W: *Blood vessels*. 6, CUP Archive 1976.

48. Virchow R: *Virchow (1998) Thrombosis and emboli (1846-1856)*. Science History Publications (Canton, Mass) 1998.

49. Ross R, Glomset J, Harker L: **Response to injury and atherogenesis.** *The American journal of pathology* 1977, **86**(3):675.

50. Stary H, Chandler A, Glagov S, Guyton J, Insull Jr W, Rosenfeld M, Schaffer S, Schwartz C, Wagner W, Wissler R: **A definition of initial, fatty streak, and intermediate lesions of atherosclerosis. A report from the Committee on Vascular Lesions of the Council on Arteriosclerosis, American Heart Association**. *Arteriosclerosis, Thrombosis, and Vascular Biology* 1994, **14**(5):840.

51. Raines E, Ross R: **Smooth muscle cells and the pathogenesis of the lesions of atherosclerosis**. *British heart journal* 1993, **69**(1 Suppl):S30.

52. Andreeva E, Pugach I, Orekhov A: **Collagen-synthesizing cells in initial and advanced atherosclerotic lesions of human aorta**. *Atherosclerosis* 1997, **130**(1-2):133–142.

53. MacLeod D, Strauss B, de Jong M, Escaned J, Umans V, van Suylen R, Verkerk A, de Feyter P, Serruys P: **Proliferation and extracellular matrix synthesis of smooth muscle cells cultured from human coronary atherosclerotic and restenotic lesions**. *Journal of the American College of Cardiology* 1994, **23**:59–65.

54. Littlewood T, Bennett M: **Apoptotic cell death in atherosclerosis**. *Current opinion in lipidology* 2003, **14**(5):469.

55. Shiomi M, Ito T, Hirouchi Y, Enomoto M: **Fibromuscular cap composition is important for the stability of established atherosclerotic plaques in mature WHHL rabbits treated with statins**. *Atherosclerosis* 2001, **157**:75–84.

56. Virmani R, Burke A, Farb A: **Plaque rupture and plaque erosion.** *Thrombosis and haemostasis* 1999, **82**:1.

57. Cerne A, Kranjec I: **Atherosclerotic burden in coronary and peripheral arteries in patients with first clinical manifestation of coronary artery disease**. *Heart and vessels* 2002, **16**(6):217–226.

58. Caro C, Fitz-Gerald J, Schroter R: **Arterial wall shear and distribution of early atheroma in man**. *Letters to Nature* 1969.

59. Ku D, Giddens D, Zarins C, Glagov S: **Pulsatile flow and atherosclerosis in the human carotid bifurcation. Positive correlation between plaque location and low oscillating shear stress**. *Arteriosclerosis, Thrombosis, and Vascular Biology* 1985, **5**(3):293–302.

60. Ohura N, Yamamoto K, Ichioka S, Sokabe T, Nakatsuka H, Baba A, Shibata M, Nakatsuka T, Harii K, Wada Y, et al.: **Global analysis of shear stress-responsive genes in vascular endothelial cells**. *Journal of atherosclerosis and thrombosis* 2003, **10**(5):304–313.

61. Nagel T, Resnick N, Dewey Jr C, Gimbrone Jr M: **Vascular endothelial cells respond to spatial gradients in fluid shear stress by enhanced activation of transcription factors**. *Arteriosclerosis, thrombosis, and vascular biology* 1999, **19**(8):1825.

62. Yamawaki H, Pan S, Lee R, Berk B: **Fluid shear stress inhibits vascular inflammation by decreasing thioredoxin-interacting protein in endothelial cells**. *Journal of Clinical Investigation* 2005, **115**(3):733–738.

63. Lum R, Wiley L, Barakat A: **Influence of different forms of fluid shear stress on vascular endothelial TGF-beta1 mRNA expression.** *International journal of molecular medicine* 2000, **5**(6):635.

64. Chappell D, Varner S, Nerem R, Medford R, Alexander R: **Oscillatory shear stress stimulates adhesion molecule expression in cultured human endothelium**. *Circulation research* 1998, **82**(5):532.

65. Walpola P, Gotlieb A, Cybulsky M, Langille B: **Expression of ICAM-1 and VCAM-1 and monocyte adherence in arteries exposed to altered shear stress**. *Arteriosclerosis, thrombosis, and vascular biology* 1995, **15**:2.

66. Urbich C, Fritzenwanger M, Zeiher A, Dimmeler S: **Laminar shear stress upregulates the complement-inhibitory protein clusterin: a novel potent defense mechanism against complement-induced endothelial cell activation**. *Circulation* 2000, **101**(4):352.

67. Khachigian L, Resnick N, Gimbrone Jr M, Collins T: **Nuclear factor-kappa B interacts functionally with the platelet-derived growth factor B-chain shear-stress response element in vascular endothelial cells exposed to fluid shear stress.** *Journal of Clinical Investigation* 1995, **96**(2):1169.

68. De Keulenaer G, Chappell D, Ishizaka N, Nerem R, Alexander R, Griendling K: **Oscillatory and steady laminar shear stress differentially affect human endothelial redox state: role of a superoxide-producing NADH oxidase**. *Circulation research* 1998, **82**(10):1094–1101.

69. Stary H, Chandler A, Dinsmore R, Fuster V, Glagov S, Insull Jr W, Rosenfeld M, Schwartz C, Wagner W, Wissler R: **A definition of advanced types of atherosclerotic lesions and a histological classification of atherosclerosis: a report from the Committee on Vascular Lesions of the Council on Arteriosclerosis, American Heart Association**. *Circulation* 1995, **92**(5):1355.

70. Kolodgie F, Burke A, Farb A, Gold H, Yuan J, Narula J, Finn A, Virmani R: **The thin-cap fibroatheroma: a type of vulnerable plaque: the major precursor lesion to acute coronary syndromes**. *Current opinion in cardiology* 2001, **16**(5):285.

71. Libby P: **Changing concepts of atherogenesis**. *Journal of internal medicine* 2000, **247**(3):349–358.

72. Shiomi M, Ito T, Yamada S, Kawashima S, Fan J: **Development of an animal model for spontaneous myocardial infarction (WHHLMI rabbit)**. *Arteriosclerosis, thrombosis, and vascular biology* 2003, **23**(7):1239–1244.

73. Shiomi M, Ito T, Yamada S, Kawashima S, Fan J: **Correlation of Vulnerable Coronary Plaques to Sudden Cardiac Events Lessons from a Myocardial Infarction-prone Animal Model (the WHHLMI Rabbit)**. *Journal of atherosclerosis and thrombosis* 2004, **11**(4):184–189.

74. Kita T, Brown M, Watanabe Y, Goldstein J: **Deficiency of low density lipoprotein receptors in liver and adrenal gland of the WHHL rabbit, an animal model of familial hypercholesterolemia**. *Proceedings of the National Academy of Sciences* 1981, **78**(4):2268.

75. SHIMADA Y, TANZAWA K, KURODA M, TSUJITA Y, ARAI M, WATANABE Y: **Biochemical Characterization of Skin Fibroblasts Derived from WHHL-Rabbit, a Notable Animal Model for Familial Hypercholesterolemia**. *European Journal of Biochemistry* 1981, **118**(3):557–564.

76. Aliev G, Burnstock G: **Watanabe rabbits with heritable hypercholesterolaemia: a model of atherosclerosis.** *Histology and histopathology* 1998, **13**(3):797.

77. Shiomi M, Ito T, Tsukada T, Yata T, Ueda M: **Cell compositions of coronary and aortic atherosclerotic lesions in WHHL rabbits differ. An immunohistochemical study**. *Arteriosclerosis, Thrombosis, and Vascular Biology* 1994, **14**(6):931.

78. Bhawalkar J, Shih A, Pan S, Liou W, Swiatkiewicz J, Reinhardt B, Prasad P, Cheng P: **Two-photon laser scanning fluorescence microscopy-from a fluorophore and specimen perspective**. *Bioimaging* 1996, **4**(3):168–178.

79. Gerritsen H, De Grauw C: **Imaging of optically thick specimen using two-photon excitation microscopy**. *Microscopy research and technique* 1999, **47**(3):206–209.

80. Xu C, Zipfel W, Shear J, Williams R, Webb W: **Multiphoton fluorescence excitation: new spectral windows for biological nonlinear microscopy**. *Proceedings of the National Academy of Sciences* 1996, **93**(20):10763.

81. Sako Y, Sekihata A, Yanagisawa Y, Yamamoto M, Shimada Y, Ozaki K, Kusumi A: **Comparison of two-photon excitation laser scanning microscopy with UV-confocal laser scanning microscopy in three-dimensional calcium imaging using the fluorescence indicator Indo-1**. *Journal of microscopy* 1997, **185**:9–20.

82. Levene M, Dombeck D, Kasischke K, Molloy R, Webb W: **In vivo multiphoton microscopy of deep brain tissue**. *Journal of neurophysiology* 2004, **91**(4):1908.

83. Helmchen F, Waters J: **Ca2+ imaging in the mammalian brain in vivo**. *European journal of pharmacology* 2002, **447**(2-3):119–129.

84. Molitoris B, Sandoval R: **Intravital multiphoton microscopy of dynamic renal processes**. *American Journal of Physiology-Renal Physiology* 2005, **288**(6):F1084.

85. Yu W, Sandoval R, Molitoris B: **Quantitative intravital microscopy using a Generalized Polarity concept for kidney studies**. *American Journal of Physiology-Cell Physiology* 2005, **289**(5):C1197.

86. Ashworth S, Tanner G: **Fluorescent labeling of renal cells in vivo**. *Nephron Physiology* 2006, **103**(2):p91–p96.

87. Dunn K, Young P: **Principles of multiphoton microscopy**. *Nephron Experimental Nephrology* 2006, **103**(2):e33–e40.

88. Mempel T, Scimone M, Mora J, von Andrian U: **In vivo imaging of leukocyte trafficking in blood vessels and tissues**. *Current opinion in immunology* 2004, **16**(4):406–417.

89. Tozer G, Ameer-Beg S, Baker J, Barber P, Hill S, Hodgkiss R, Locke R, Prise V, Wilson I, Vojnovic B: **Intravital imaging of tumour vascular networks using multi-photon fluorescence microscopy**. *Advanced drug delivery reviews* 2005, **57**:135–152.

90. Albota M, Xu C, Webb W: **Two-photon fluorescence excitation cross sections of biomolecular probes from 690 to 960 nm**. *Applied optics* 1998, **37**(31):7352–7356.

91. So P, Dong C, Masters B, Berland K: **Two-photon excitation fluorescence microscopy**. *Annual Review of Biomedical Engineering* 2000, **2**:399–429.

92. Konig K: **Multiphoton microscopy in life sciences**. *Journal of Microscopy* 2000, **200**(2):83–104.

93. Hecht E: **Optics 2nd edition**. *Optics 2nd edition by Eugene Hecht Reading, MA: Addison-Wesley Publishing Company, 1987* 1987, **1**.

94. Stoller P, Kim B, Rubenchik A, Reiser K, Da Silva L: **Polarization-dependent optical second-harmonic imaging of a rat-tail tendon**. *Journal of Biomedical Optics* 2002, **7**:205.

95. Williams R, Zipfel W, Webb W: **Interpreting second-harmonic generation images of collagen I fibrils**. *Biophysical journal* 2005, **88**(2):1377–1386.

96. Stoller P, Celliers P, Reiser K, Rubenchik A: **Quantitative second-harmonic generation microscopy in collagen**. *Applied optics* 2003, **42**(25):5209–5219.

97. Yasui T, Tohno Y, Araki T: **Determination of collagen fiber orientation in human tissue by use of polarization measurement of molecular second-harmonic-generation light**. *Applied optics* 2004, **43**(14):2861–2867.

98. Cheng J, Xie X: **Coherent anti-Stokes Raman scattering microscopy: instrumentation, theory, and applications**. *The Journal of Physical Chemistry B* 2004, **108**(3):827–840.

99. Cheng J, Volkmer A, Lewis D, Xie X: **An epi-detected coherent anti-Stokes Raman scattering (E-CARS) microscope with high spectral resolution and high sensitivity**. *The Journal of Physical Chemistry B* 2001, **105**(7):1277–1280.

100. Pegoraro A, Ridsdale A, Moffatt D, Jia Y, Pezacki J, Stolow A: **Optimally chirped multimodal CARS microscopy based on a single Ti: sapphire oscillator**. *Opt. Express* 2009, **17**(4):2984–2996.

101. Pologruto T, Sabatini B, Svoboda K: **ScanImage: flexible software for operating laser scanning microscopes**. *Biomed Eng Online* 2003, **2**:13.

102. Whittaker P, Kloner R, Boughner D, Pickering J: **Quantitative assessment of myocardial collagen with picrosirius red staining and circularly polarized light**. *Basic research in cardiology* 1994, **89**(5):397–410.

103. Hwang SJ, Ballantyne CM, Sharrett AR, Smith LC, Davis CE, Gotto AM, Boerwinkle E: **Circulating adhesion molecules VCAM-1, ICAM-1, and E-selectin in carotid**

**atherosclerosis and incident coronary heart disease cases the Atherosclerosis Risk In Communities (ARIC) study**. *Circulation* 1997, **96**(12):4219–4225.

104. Davies MJ, Gordon J, Gearing A, Pigott R, Woolf N, Katz D, Kyriakopoulos A: **The expression of the adhesion molecules ICAM-1, VCAM-1, PECAM, and E-selectin in human atherosclerosis**. *The Journal of pathology* 1993, **171**(3):223–229.

105. Blann AD, Seigneur M, Steiner M, Miller JP, McCollum CN, et al.: **Circulating ICAM-1 and VCAM-1 in peripheral artery disease and hypercholesterolaemia: relationship to the location of atherosclerotic disease, smoking, and in the prediction of adverse events**. *Thrombosis and haemostasis* 1998, **79**(6):1080–1085.

106. Poston R, Haskard D, Coucher J, Gall N, Johnson-Tidey R: **Expression of intercellular adhesion molecule-1 in atherosclerotic plaques.** *The American journal of pathology* 1992, **140**(3):665.

107. Katz AM, Rosenthal D, Sauder DN: **Cell adhesion molecules**. *International journal of dermatology* 1991, **30**(3):153–160.

108. Albelda S: **Role of integrins and other cell adhesion molecules in tumor progression and metastasis.** *Laboratory investigation; a journal of technical methods and pathology* 1993, **68**:4–17.

109. Haralick R, Shanmugam K, Dinstein I: **Textural features for image classification**. *Systems, Man and Cybernetics, IEEE Transactions on* 1973, **3**(6):610–621.

110. Bolte S, Cordelières FP: **A guided tour into subcellular colocalization analysis in light microscopy**. *Journal of microscopy* 2006, **224**(3):213–232.

111. Eriksson M, Alderborn G, Nyström C, Podczeck F, Newton J: **Comparison between and evaluation of some methods for the assessment of the sphericity of pellets**. *International journal of pharmaceutics* 1997, **148**(2):149–154.

112. Given JA, Mandelbrot BB: **Diffusion on fractal lattices and the fractal Einstein relation**. *Journal of Physics A: Mathematical and General* 1983, **16**(15):L565.

113. Mandelbrot BB: *The fractal geometry of nature*. Macmillan 1983.

114. Gazit Y, Baish JW, Safabakhsh N, Leunig M, Baxter LT, Jain RK: **Fractal characteristics of tumor vascular architecture during tumor growth and regression**. *Microcirculation* 1997, **4**(4):395–402.

115. Nelson T, West B, Goldberger A: **The fractal lung: universal and species-related scaling patterns**. *Experientia* 1990, **46**(3):251–254.

116. Lopes R, Betrouni N: **Fractal and multifractal analysis: a review**. *Medical image analysis* 2009, **13**(4):634–649.

117. Liu ZQ: **Scale space approach to directional analysis of images**. *Applied optics* 1991, **30**(11):1369–1373.

118. Yang ZR: **Biological applications of support vector machines**. *Briefings in bioinformatics* 2004, **5**(4):328–338.

119. Cortes C, Vapnik V: **Support-vector networks**. *Machine learning* 1995, **20**(3):273–297.

120. Burges CJ: **A tutorial on support vector machines for pattern recognition**. *Data mining and knowledge discovery* 1998, **2**(2):121–167.

121. Fukunaga K, Narendra PM: **A branch and bound algorithm for computing k-nearest neighbors**. *Computers, IEEE Transactions on* 1975, **100**(7):750–753.

122. Works G: **Neural network basics.** *AUTOFACT'89* 1989, :29–1.

123. Jakkula V: **Tutorial on support vector machine (svm)**. *School of EECS, Washington State University* 2006.

124. Muller K, Mika S, Ratsch G, Tsuda K, Scholkopf B: **An introduction to kernel-based learning algorithms**. *Neural Networks, IEEE Transactions on* 2001, **12**(2):181–201.

125. Cristianini N, Shawe-Taylor J: *An introduction to support vector machines and other kernel-based learning methods*. Cambridge university press 2000.

126. Skapura DM: *Building neural networks*. Addison-Wesley Professional 1996.

127. Mitchell TM: **Machine learning and data mining**. *Communications of the ACM* 1999, **42**(11):30–36.

128. Lewis J: **Tutorial on SVM**. *CGIT Lab, USC* 2004.

129. Karatzoglou A, Smola A, Hornik K, Zeileis A: **kernlab-an S4 package for kernel methods in R**. *Journal of Statistical Software* 2004.

130. Strupler M, Pena A, Hernest M, Tharaux P, Martin J, Beaurepaire E, Schanne-Klein M: **Second harmonic imaging and scoring of collagen in fibrotic tissues**. *Optics Express* 2007, **15**(7):4054–4065.

131. Kolodgie FD, Virmani R, Rice H, Mergner W: **Vascular reactivity during the progression of atherosclerotic plaque. A study in Watanabe heritable hyperlipidemic rabbits.** *Circulation research* 1990, **66**(4):1112–1126.

132. Di Tullio MR, Russo C, Jin Z, Sacco RL, Mohr J, Homma S, et al.: **Aortic arch plaques and risk of recurrent stroke and death**. *Circulation* 2009, **119**(17):2376–2382.

133. Vincent P, Plata A, Hunt A, Weinberg P, Sherwin S: **Blood flow in the rabbit aortic arch and descending thoracic aorta**. *Journal of The Royal Society Interface* 2011.

134. Caro C: **Discovery of the role of wall shear in atherosclerosis**. *Arteriosclerosis, thrombosis, and vascular biology* 2009, **29**(2):158.

135. Gimbrone MA, Topper JN, Nagel T, Anderson KR, GARCIA-CARDEÑA G: **Endothelial dysfunction, hemodynamic forces, and atherogenesisa**. *Annals of the New York Academy of Sciences* 2000, **902**:230–240.

136. Scharfstein H, Gutstein W, Lewis L: **Changes of boundary layer flow in model systems: Implications for initiation of endothelial injury**. *Circulation research* 1963, **13**(6):580–584.

137. Ferguson G, Roach M: **Flow conditions at bifurcations as determined in glass models, with reference to the focal distribution of vascular lesions**. *Cardiovascular fluid dynamics* 1972, **2**:141–157.

138. Gutstein W, Schneck D, Marks J: **In vitro studies of local blood flow disturbance in a region of separation**. *Journal of Atherosclerosis Research* 1968, **8**(3):381–388.

139. Stehbens W: **Turbulence of blood flow**. *Experimental Physiology* 1959, **44**:110.

140. Shahcheraghi N, Dwyer H, Cheer A, Barakat A, Rutaganira T: **Unsteady and three-dimensional simulation of blood flow in the human aortic arch**. *Journal of biomechanical engineering* 2002, **124**:378.

141. Frangos SG, Gahtan V, Sumpio B: **Localization of atherosclerosis: role of hemodynamics**. *Archives of Surgery* 1999, **134**(10):1142.

142. Ku D: **Blood flow in arteries**. *Annual Review of Fluid Mechanics* 1997, **29**:399–434.

143. Tarbell J: **Mass transport in arteries and the localization of atherosclerosis**. *Annual review of biomedical engineering* 2003, **5**:79–118.

144. Stary H, Blankenhorn D, Chandler A, Glagov S, Insull Jr W, Richardson M, Rosenfeld M, Schaffer S, Schwartz C, Wagner W: **A definition of the intima of human arteries and of its atherosclerosis-prone regions. A report from the Committee on Vascular Lesions of the Council on Arteriosclerosis, American Heart Association**. *Arteriosclerosis, Thrombosis, and Vascular Biology* 1992, **12**:120.

145. Chen S, Gibson C, Kan J, Zhang J, Hu Z, Xu H, Xu T, Ye F, Tian N, Zhang J, et al.: **AS-004 Dynamic Change Of Wall Shear Stress After Stenting Bifurcation Lesions: Subgroup Analysis From DKCRUSH-II Trial**. *The American Journal of Cardiology* 2011, **107**(8):2A–2A.

146. Lilledahl M, Haugen O, de Lange Davies C, Svaasand L: **Characterization of vulnerable plaques by multiphoton microscopy**. *Journal of Biomedical Optics* 2007, **12**:044005.

147. Blankenhorn D, Braunstein H: **Carotenoids in man. III. The microscopic pattern of fluorescence in atheromas, and its relation to their growth**. *Journal of Clinical Investigation* 1958, **37**(2):160.

148. Arakawa K, Isoda K, Ito T, Nakajima K, Shibuya T, Ohsuzu F: **Fluorescence analysis of biochemical constituents identifies atherosclerotic plaque with a thin fibrous cap**. *Arteriosclerosis, thrombosis, and vascular biology* 2002, **22**(6):1002–1007.

149. Virmani R, Kolodgie F, Burke A, Farb A, Schwartz S: **Lessons from sudden coronary death: a comprehensive morphological classification scheme for atherosclerotic lesions**. *Arteriosclerosis, thrombosis, and vascular biology* 2000, **20**(5):1262.

150. Razzaque MS, Taguchi T: **Pulmonary fibrosis: cellular and molecular events**. *Pathology international* 2003, **53**(3):133–145.

151. Friedman SL: **Molecular regulation of hepatic fibrosis, an integrated cellular response to tissue injury**. *Journal of Biological Chemistry* 2000, **275**(4):2247–2250.

152. Barshop N, Sirlin C, Schwimmer J, Lavine J: **Review article: epidemiology, pathogenesis and potential treatments of paediatric non-alcoholic fatty liver disease**. *Alimentary pharmacology & therapeutics* 2008, **28**:13–24.

153. Varga J, Abraham D, et al.: **Systemic sclerosis: a prototypic multisystem fibrotic disorder**. *The Journal of clinical investigation* 2007, **117**(3):557–567.

154. Krieg T, Perlish JS, Mauch C, Fleischmajer R: **Collagen Synthesis by Scleroderma Fibroblastsa**. *Annals of the New York Academy of Sciences* 1985, **460**:375–386.

155. Riley G: **The pathogenesis of tendinopathy. A molecular perspective**. *Rheumatology* 2004, **43**(2):131–142.

156. Nissi M, Töyräs J, Laasanen M, Rieppo J, Saarakkala S, Lappalainen R, Jurvelin J, Nieminen M: **Proteoglycan and collagen sensitive MRI evaluation of normal and degenerated articular cartilage**. *Journal of Orthopaedic Research* 2004, **22**(3):557–564.

157. Mahmoud-Ghoneim D, Amin A, Corr P: **MRI-based texture analysis: a potential technique to assess protectors against induced-liver fibrosis in rats**. *Radiology and Oncology* 2009, **43**:30–40.

158. Chen J, Song SK, Liu W, McLean M, Allen JS, Tan J, Wickline SA, Yu X: **Remodeling of cardiac fiber structure after infarction in rats quantified with diffusion tensor MRI**. *American Journal of Physiology-Heart and Circulatory Physiology* 2003, **285**(3):H946–H954.

159. Ooi GJ, Fox J, Siu K, Lewis R, Bambery KR, McNaughton D, Wood BR: **Fourier transform infrared imaging and small angle x-ray scattering as a combined biomolecular approach to diagnosis of breast cancer**. *Medical physics* 2008, **35**(5):2151–2161.

160. Suhonen H, Fernández M, Serimaa R, Suortti P: **Simulation of small-angle x-ray scattering from collagen fibrils and comparison with experimental patterns**. *Physics in medicine and biology* 2005, **50**(22):5401.

161. Rawlins JM, Lam WL, Karoo RO, Naylor IL, Sharpe DT: **Quantifying collagen type in mature burn scars: a novel approach using histology and digital image analysis**. *Journal of burn care & research* 2006, **27**:60–65.

162. George M, Morgan J, Glock R, Tatum J, Schmidt G, Sofos J, Cowman G, Smith G: **Injection-site lesions: incidence, tissue histology, collagen concentration, and muscle tenderness in beef rounds.** *Journal of animal science* 1995, **73**(12):3510–3518.

163. Han X, Burke RM, Zettel ML, Tang P, Brown EB: **Second harmonic properties of tumor collagen: determining the structural relationship between reactive stroma and healthy stroma**. *Optics express* 2008, **16**(3):1846–1859.

164. Chen X, Huang Z, Xi G, Chen Y, Lin D, Wang J, Li Z, Sun L, Chen J, Chen R: **Quantitative analysis of collagen change between normal and cancerous thyroid tissues based on SHG method**. In *Photonics and Optoelectronics Meetings 2011*, International Society for Optics and Photonics 2012:83290H–83290H.

165. Lin SJ, Hsiao CY, Sun Y, Lo W, Lin WC, Jan GJ, Jee SH, Dong CY: **Monitoring the thermally induced structural transitions of collagen by use of second-harmonic generation microscopy**. *Optics letters* 2005, **30**(6):622–624.

166. Su PJ, Chen WL, Li TH, Chou CK, Chen TH, Ho YY, Huang CH, Chang SJ, Huang YY, Lee HS, et al.: **The discrimination of type I and type II collagen and the label-free imaging of engineered cartilage tissue**. *Biomaterials* 2010, **31**(36):9415–9421.

167. Lu K, Chen J, Zhuo S, Zheng L, Jiang X, Zhu X, Zhao J: **Multiphoton laser scanning microscopy of localized scleroderma**. *Skin Research and Technology* 2009, **15**(4):489–495.

168. Chen WL, Huang CH, Chiou LL, Chen TH, Huang YY, Jiang CC, Lee HS, Dong CY: **Multiphoton imaging and quantitative analysis of collagen production by chondrogenic human mesenchymal stem cells cultured in chitosan scaffold**. *Tissue Engineering Part C: Methods* 2010, **16**(5):913–920.

169. Mega Y, Robitaille M, Zareian R, McLean J, Ruberti J, DiMarzio C: **Quantification of lamellar orientation in corneal collagen using second harmonic generation images**. *Optics letters* 2012, **37**(16):3312–3314.

170. Guilbert T, Odin C, Le Grand Y, Gailhouste L, Turlin B, Ezan F, DÚsille Y, Baffet G, Guyader D: **A robust collagen scoring method for human liver fibrosis by second harmonic microscopy**. *Optics express* 2010, **18**(25):25794–25807.

171. Ambekar R, Lau TY, Walsh M, Bhargava R, Toussaint KC: **Quantifying collagen structure in breast biopsies using second-harmonic generation imaging**. *Biomedical optics express* 2012, **3**(9):2021–2035.

172. Cleutjens J, Verluyten M, Smiths J, Daemen M: **Collagen remodeling after myocardial infarction in the rat heart.** *The American journal of pathology* 1995, **147**(2):325.

173. Wang L, Deng J, Tian W, Xiang B, Yang T, Li G, Wang J, Gruwel M, Kashour T, Rendell J, et al.: **Adipose-derived stem cells are an effective cell candidate for treatment of heart failure: an MR imaging study of rat hearts**. *American Journal of Physiology-Heart and Circulatory Physiology* 2009, **297**(3):H1020–H1031.

174. Wallenburg MA, Wu J, Li RK, Vitkin IA: **Two-photon microscopy of healthy, infarcted and stem-cell treated regenerating heart**. *Journal of biophotonics* 2011, **4**(5):297–304.

175. Bevk M, Kononenko I: **A statistical approach to texture description of medical images: a preliminary study**. In *Computer-Based Medical Systems, 2002.(CBMS 2002). Proceedings of the 15th IEEE Symposium on*, IEEE 2002:239–244.

176. Saeys Y, Inza I, Larrañaga P: **A review of feature selection techniques in bioinformatics**. *bioinformatics* 2007, **23**(19):2507–2517.

177. Greenlee WF, Sun JD, Bus JS: **A proposed mechanism of benzene toxicity: formation of reactive intermediates from polyphenol metabolites**. *Toxicology and applied pharmacology* 1981, **59**(2):187–195.

178. Kielty CM, Sherratt MJ, Shuttleworth CA: **Elastic fibres**. *Journal of Cell Science* 2002, **115**(14):2817–2828.

179. Wagenseil JE, Mecham RP: **Vascular extracellular matrix and arterial mechanics**. *Physiological reviews* 2009, **89**(3):957.

180. Masuda H, Zhuang YJ, Singh TM, Kawamura K, Murakami M, Zarins CK, Glagov S: **Adaptive remodeling of internal elastic lamina and endothelial lining during flow-induced arterial enlargement**. *Arteriosclerosis, thrombosis, and vascular biology* 1999, **19**(10):2298–2307.

181. Brizzolara A, Tomlinson A, Aberdeen J, Gourdie R, Burnstock G: **Sex and age as factors influencing the vascular reactivity in Watanabe heritable hyperlipidaemic (WHHL) rabbits: a pharmacological and morphological study of the hepatic artery**. *Journal of cardiovascular pharmacology* 1992, **19**:86–95.

182. Wong LC, Langille BL: **Developmental remodeling of the internal elastic lamina of rabbit arteries effect of blood flow**. *Circulation research* 1996, **78**(5):799–805.

183. Briones AM, González JM, Somoza B, Giraldo J, Daly CJ, Vila E, Carmen González M, McGrath JC, Arribas SM: **Role of elastin in spontaneously hypertensive rat small mesenteric artery remodelling**. *The Journal of physiology* 2003, **552**:185–195.

184. Haralick RM, Watson LT, Laffey TJ: **The topographic primal sketch**. *The International Journal of Robotics Research* 1983, **2**:50–72.

185. Koller TM, Gerig G, Szekely G, Dettwiler D: **Multiscale detection of curvilinear structures in 2-D and 3-D image data**. In *Computer Vision, 1995. Proceedings., Fifth International Conference on*, IEEE 1995:864–869.

186. Sato Y, Nakajima S, Atsumi H, Koller T, Gerig G, Yoshida S, Kikinis R: **3D multi-scale line filter for segmentation and visualization of curvilinear structures in medical images**. In *CVRMed-MRCAS'97*, Springer 1997:213–222.

187. Boser BE, Guyon IM, Vapnik VN: **A training algorithm for optimal margin classifiers**. In *Proceedings of the fifth annual workshop on Computational learning theory*, ACM 1992:144–152.

# Glossary

**AA**

aorta arch. xi, xiv, xxi, 31, 32, 64, 65, 122–124

**ACC**

American College of Cardiology. 80

**AHA**

American Heart Association. vii, xvii, 7, 80–84

**AR**

aspect ratio. 41

**ASC**

adipose-derived stem cells. xviii, 91–97, 104

**ASM**

angular second moment. xvii, 78, 79

**AbA**

abdominal artery. xi, xiv, xxi, 31, 32, 64, 65, 123, 124

**BF**

bandpass filter. x, 29, 30

**BS**

beam splitter. x, 29

**CARS**

coherent anti-Stokes Raman scattering. i, vii, x–xiii, xv–xvii, xx, 3–5, 7, 8, 15, 23–26, 28–30, 33, 39, 51–54, 57, 67–70, 72–79, 83, 85, 97, 108–113, 115, 130–132

**CCD**

charge-coupled device. 33, 36

**CM**

chirp laser mirrors. x, 29

**DM**

dichroic mirror. x, 29, 30

**ECM**

extracellular matrix. 10, 11, 116

**EEL**

external elastic layer. ix, 10

**EIA**

external iliac artery. xi, xiv, xxi, 31, 32, 64, 65, 123, 124

**F-ISO**

Faraday isolator. x, 29

**FOS**

first order statistics. vii, xviii, xx, 39, 84–87, 89, 93–96, 99, 101–106, 109, 110, 112, 113, 133

**FT**

Fourier transform. 44

**GLCM**

gray level co-occurrence matrix. vii, xvi–xx, 37, 39, 73–76, 78, 84–87, 89, 93–96, 101–106, 110–113, 133

**GLRLM**

gray level run length matrix. 133

**GS**

galvo scanner. x, 29, 30

**GVD**

group velocity dispersion. 29

**ICAM-1**

intercellular adhesion molecule 1. xiv, 14, 35, 63–65, 129

**IDM**

inverse difference moment. xvi–xviii, 73, 76, 78, 79, 94–96, 101, 110

**IEL**

internal elastic layer. ix, 9, 10, 119, 121, 122, 124

**IHC**

immunohistochemistry. xi, 5, 32, 35, 129

**IgG**

immunoglobulin G. 34

**LDL**

low density lipoprotein. xii, 14, 51

**MCP-1**

monocyte chemoattractant protein-1. 14

**MMP-9**

matrix metallopeptidase 9. 14

**MRI**

magnetic resonance imaging. 90

**NADH**

nicotinamide adenine dinucleotide. 14

**NIR**

near infrared. 29

**NIR-F**

near-IR filter. x, 29

**NLO**

nonlinear optical. i, xi–xiii, xv–xvii, 3–7, 15, 27, 28, 30, 33, 34, 36–38, 47, 50–52, 55, 56, 59, 63, 65–68, 70, 72, 73, 75–79, 82, 83, 86, 87, 128–131, 133, 134

**NLOM**

nonlinear optical microscopy. i, 1–7, 15, 26, 65, 90

**OBJ**

objective lens. x, 29, 30

**OIPB**

optical index for plaque burden. i, vii, xi, xiii, xiv, xvii, 4–7, 36, 37, 55, 57–65, 82–87, 129, 130

**PBS**

phosphate buffered saline. 32, 35

**PCF**

photonics crystal fiber. 28, 29

**PMT**

photomultiplier. x, 29, 30, 53

**PSF**

point spread function. 132

**ROC**

receiver operating characteristic. xviii, 95, 96

**ROI**

region of interest. 94

**SHG**

second harmonic generation. i, vii, x–xiii, xv–xix, 2–5, 7, 15, 19, 21, 22, 25, 26, 28–30, 33, 51–54, 57, 67–70, 72–79, 83, 85, 89–95, 97–100, 102, 106, 107, 113, 130, 135

**SMC**

smooth muscle cell. ix, xv, 10, 12, 50, 67, 68, 81

**SVM**

support vector machine. vii, 37, 44–48, 86, 95, 102, 106, 112, 113

**TA**

thoracic artery. xi, xiv, xxi, 31, 32, 64, 65, 123, 124

**THG**

third harmonic generation. 25, 26

**TPEF**

two-photon excited autofluorescence. i, x–xiii, xv–xviii, xx, xxi, 2–5, 7, 8, 15, 17, 18, 22, 26, 28–30, 33, 44, 51–54, 57, 66–68, 70–79, 83, 85, 91, 93, 97, 118–126, 130, 131

**VCAM-1**

vascular cell adhesion protein 1. 14

**WHHLMI**

myocardial infarction prone Watanabe heritable hyperlipidemic. xii–xv, xvii, xix, xx, 6, 14, 31, 50–52, 54, 57, 59, 62, 64, 67, 76, 97–99, 109, 129